SIMULATION BASED EXPERIMENTS OF
TRAVELING-PLANE-WAVE-ACTUATOR MICROPUMPS AND
MICROSWIMMERS

by

AHMET FATİH TABAK

Submitted to the Graduate School of Engineering and Natural Sciences
in partial fulfillment of
the requirements for the degree of
Master of Science

SABANCI UNIVERSITY
Spring 2007

SIMULATION BASED EXPERIMENTS OF
TRAVELING-PLANE-WAVE-ACTUATOR MICROPUMPS AND
MICROSWIMMERS

APPROVED BY:

        Dr. SERHAT YEŞİLYURT   ………………………
        (Thesis Advisor)

        Dr. AYHAN BOZKURT   ………………………

        Dr. GÜLLÜ KIZILTAŞ ŞENDUR ………………………

        Dr. MAHMUT F. AKŞİT   ………………………

        Dr. MELİH PAPİLA   ………………………

DATE OF APPROVAL: 04.06.2007

SIMULATION BASED EXPERIMENTS OF

TRAVELING-PLANE-WAVE-ACTUATOR MICROPUMPS AND

MICROSWIMMERS

Ahmet Fatih Tabak

EECS, MS Thesis, 2007

Thesis Supervisor: Serhat Yeşilyurt

Keywords: Micropump, micropropulsion, microswimmer, traveling-plane-wave, inextensible film, hydraulic power, efficiency

ABSTRACT

A biologically-inspired micropropulsion method is presented by constructing a series of finite element computational fluid dynamics models for time irreversible inextensible wave propagation method in viscous medium. First, micropump models encompassing fully submerged and anchored waving inextensible film mounted inside a microchannel are analyzed to attain flow, hydraulic power consumption and efficiency plots with respect to parameterized design variables via both 2D and 3D models. Each model is governed by incompressible isothermal Stokes and Navier-Stokes equations respectively and conservation of mass, integrated with deforming mesh employing arbitrary Lagrangian Eulerian method.

Next, propulsion velocity, power consumption and efficiency plots of a fully submerged free microswimmer utilizing a wave propagating tail inside a viscous environment is analyzed with respect to parameterized design variables via 3D models governed by incompressible isothermal Navier-Stokes equations and conservation of mass, integrated with deforming mesh employing arbitrary Lagrangian Eulerian Method. All resultant swimmer motions are modeled directly incorporating with stress interactions between surrounding viscous fluid and swimmer surfaces. It is demonstrated that net forward thrust can be harvested from this interaction.

Numerical results are compared with the asymptotical results to analytical studies mainly carried out by Sir Taylor (1951), Katz (1974) and Childress (1981) based on mainly 2D assumptions. It is observed that there exists a strong agreement between earlier results and numerical results besides from wavelength parameter which illustrates slight deviation in power consumption characteristics due to the effects introduced by the existence of third dimension.

YÜRÜYEN-DÜZLEM-DALGA-EYLEYİCİ MİKROPOMPA VE

MİKROYÜZÜCÜLERİN BENZETİM TABANLI DENEYLERİ

Ahmet Fatih Tabak

EECS, Yüksek Lisans Tezi, 2007

Tez Danışmanı: Serhat Yeşilyurt

Anahtar Kelimeler: Mikropompa, mikroitici, mikroyüzücü, yürüyen-düzlem-dalga, uzatılamaz film, hidrolik güç, verim

ÖZET

Doğadan esinlenerek, sonlu eleman hesabına dayalı akışkanlar dinamiği modelleri yardımı ile ağdalı ortamlarda zamanla tersinemez-uzatılamaz dalga yayılımı ile eylenen mikro-itici yöntemi sunulmuştur. Öncelikle, sıvı ile dolu bir mikrokanal içerisinde çapalanmış uzatılamaz ince filmden oluşan iki ve üç boyutlu mikropompa modelleri analiz edilerek parametrik tasarım değişkenlerinin sıvı akışı, hidrolik güç tüketimi ve verim üzerindeki etkisi grafiksel olarak elde edilmiştir. Tüm modeler, sırasıyla sıkıştırılamaz-izotermal Stokes ve sıkıştırılamaz-izotermal Navier Stokes denklemleri, kütlenin korunumu yasası ve biçimi bozulan örgü yöntemi (ALE) kullanılarak çözülmüştür.

Sonraki adımda, tamamen ağdalı akışkan içerisine batırılmış ve yürüyen-düzlem-dalga hareketi ile eylenen kuyruk yardımı ile hareket eden üç boyutlu mikroyüzücü tasarımının parametrik tasarım değişkenlerinin itici hızı, hidrolik güç tüketimi ve yüzücü verimi üzerinki etkisi sıkıştırlamaz-izotermal Navier-Stokes, kütlenin korunumu yasası ve biçimi bozulan örgü yapısı (ALE) yardımı ile grafiksel olarak elde edilmiştir. Mikroyüzücünün hareketleri, etrafını saran ağdalı akışın mikroyüzücü yüzeyine uyguladığı kuvvetlerden yararlanılarak elde edilmiştir. Bu etkileşimden net itme kuvveti elde edilebileceği gözlemlenmiştir.

Sayısal sonuçlar başlıca Taylor (1951), Katz (1974) ve Childress (1981) tarafından iki boyutlu varsayımlar üzerinde yapılmış analitik çalışmaların asemptotic sonuçları ile karşılaştırılmıştır. Üçüncü boyutun varlığının etkisi yüzünden dalga boyu grafiklerinde gözlemlenen sapma dışında, sayısal sonuçlarla asemptotic sonuçlar arasında güçlü bir tutarlılık olduğu görülmüştür.

"May fortune favor the foolish"

- James T. Kirk

ACKNOWLEDGEMENTS

I am greatly indebted to Dr. Serhat Yeşilyurt for his limitless patience, wisdom and assistance during embodiment of this work. His guidance prevented me getting lost throughout my research and his discussions improved my perception of the subject.

My sincere thanks Dr. Güllü Kızıltaş Şendur, Dr. Melih Papila, Dr. Ayhan Bozkurt, Dr. Mahmut Akşit and Dr. Volkan Patoğlu for their help and understanding whenever I needed.

I would like to thank my family; Muharrem, Ergül and Halil Can (Tabak Jr.) for their unconditional support on each step I took.

I thank all my lab mates both in Mechatronics and Material Science programs for being there when I needed; especially Cenk for 'experiment based' laughter from dusk till dawn, Didem for educational discussions on materials, Altuğ for his priceless assistance and Erhan for his valuable advice.

TABLE OF CONTENTS

LIST OF TABLES

LIST OF FIGURES

LIST OF SYMBOLS

Latin

A	Area
B	Amplitude function
C	Proportionality constant
D	Electric displacement
E	Bending rigidity
E	Electric field
F	Force
H	Channel Height
I	Identity matrix
J	Mass moment of inertia
K	Resistive force
L	Channel length
L	Lagrangian Function
M	Mass
M	Moment
P	Momentum
P	Pressure
Q, **Q**	Flow rate
$\Re$	Ramp time function
S	Surface coordinates
T	Torque
U	Generic velocity
U	Fluid velocity vector in stationary reference frame
W	Width
X	Stationary reference frame

X, Y, Z	Stationary reference frame coordinates
a	Major axis
b	Minor axis
c	Wave speed
d	Piezoelectric coupling constant
e	Tensor element
f, f	Driving frequency
g	Gravitational attraction
h	Body (head) property
k	Wave number
ℓ	Generic length
n	Surface normal vector
r	Radius
r	Position vector
s	Compliance matrix element
t	Time
t	Surface tangent vector
u	ALE velocity vector
ϑ	Volume
w	Material velocity vector
u, v, w	velocity vector components
χ	Material frame
x	ALE frame
x, y, z	Coordinates in ALE frame
Greek	
$\wp$	Geometry dependent functions
Θ	Surface angle
Λ	Geometry constant
Π	Power
Σ	Total quantity
ϕ	Mesh node location
Φ	Shear loss function

Ψ	Stream function
Ω	Deforming domain
β	Rubber mesh function
γ	Shear deformation
δ	Dirac delta function
ε	Axial deformation
$\in$	Permittivity constant
ζ	Resistive force coefficient / viscous drag coefficient
η	Efficiency
θ	Rotation angle
λ , λ	Wave length
μ	Viscosity
ρ	Density
σ	Stress element, axial stress
$\boldsymbol{\sigma}$	Stress tensor
τ	Shear stress
φ	Particle motion function
ω	Angular frequency
ϖ	Angular velocity of swimmer

Superscripts

i	Particle number
p	Pump
$P1$, $P2$	Arbitrary locations
$R1$, $R2$	Arbitrary reference frames
s	Swimmer
T	Transpose
z	Zone-limit quantity
2D	Two dimensional
3D	Three dimensional
*	Dimensionless quantity

Subscripts

av	Time averaged quantity
ch	Channel geometry
com	Center of mass
f	Membrane, film, tail
i, j	Orientation element
in, out	Flow direction
m	Mesh parameter
max	Maximum function
min	Minimum function
o	Maximum possible value, flow developing time
p	Propulsion, thrust
Q	Flow rate
r	Relative value
S	Surface
sh	Wave shape constant
top, down	Over / under the membrane & tail
w	Wave related quantity
XX, YY	Direction (fluid)
x, y, z	Coordinates in ALE frame
xx, yy, zz	Direction (piezo)
$\perp$	Normal component
$\parallel$	Tangent component
0	Characteristic scale, reference point
∞	Upstream quantity

Number Groups

Re	Reynolds Number
Sp	Sperm Number

LIST OF ABBREVIATIONS

ALE	Arbitrary Lagrangian Eulerian
ATP	Adenosine Tri-Phosphate
CABG	Coronary Artery Bypass Grafting
EHD	Electrohydrodynamic
FEA	Finite Element Analysis
GRAD	Gradient
GUI	Graphic User Interface
IPMC	Ionic Polymer-Metal Composites
MHD	Magnetohydrodynamic
MEMS	Microelectromechanical Systems
MKL	Math Kernel Library
PARDISO	Parallel Sparse Direct Linear Solver
PZT	Piezoelectric Transducer
SAW	Surface Acoustic Wave
SI	Standard International
UMFPACK	Unsymmetric Multifrontal Sparce LU Factorization Package
2D	Two Dimensional
3D	Three Dimensional

CHAPTER 1

INTRODUCTION

Microelectromechanic systems are widely employed in different areas such as telecommunication, chemical analysis and biomedical applications. Novel micro and nanoscale robotic applications are in development. Autonomous mobile micro devices, namely microrobots are promising gadgets for future uses especially in medical area. One important issue on autonomous microdevices is the ability of self mobility. Physical interactions in microrealm have their own set of interpretations due to the scaling issue. Some forces inherently dominant in macro world can not overcome surface forces in micro world and ruled out by nature herself. Fluid structure interaction is a perfect example of these phenomena. Micropropulsion systems can not operate a kin to their macroscale counterparts so there must be found an original realization to the problem at hand.

Ideally, a microelectromechanical system equipped with necessary gadgets can roam inside the human body and carry out surgical operations without any external interference on the target. The question is that whether it is possible to achieve this journey on feasible routes or not. Maneuverability and controllability of such a system depend on feasible transportation solutions. This problem represents a new research area since generally microsystems are designed to operate while mounted on larger structures. A micropropulsion system must overcome tremendous surface forces dominating against the inertial forces due to the aspect ratio with reasonable thrust effect. The surface force effect can be exemplified by the driver inside a car filled with honey. As driver brakes viscous medium does not let the driver's inertia to carry on the motion, unlike what is experienced in real life. As dimensions gets smaller the relative viscosity of the fluidic medium appears to increase significantly.

The literature which inspired this work is Feynman's (1918-1988) famous talks in the years 1959 and 1983. Therein Feynman suggested a device that can steer in microrealm and elaborated his thoughts on the ideal medical microdevice where Feynman and his friend Albert R. Hibbs discussed which was quoted as "Hibbs's swallowable surgeon" [1], [2]. The studied method on the other hand came from the nature. Nature's solutions to this specific problem and their unique properties have a significant role in embodiment of this work. As will be explained later on, motion in microrealm must satisfy some mandatory conditions and solutions presented by nature seem to obey.

1.1 Conservation of Mass and Momentum

Key elements to fluidic analysis should be introduced before going into details of microfluidic analysis. Landau and Lifshitz (2003) gave a complete definition on conservation laws [3]. Conservation of momentum is an interpretation of "homogeneity of space" by which meant is the invariance of mechanical properties in translational motions and can be expressed in terms of Lagrangian formulation [3]. Momentum equation is defined as:

$$\mathbf{P} = \sum_i \left(M\mathbf{U} \right)_i \tag{1.1}$$

which is a vector quantity, where $\mathbf{U}$ is the particle velocity (will be referred as the fluid velocity vector later on) with respect to XYZ and M denotes the mass of a particle. Lagrange equation has the property of invariance under infinitesimal position changes which is expressed as $\sum_i \partial L/\partial \mathbf{r}^i_{XYZ} = 0$ where $\mathbf{r}$ is the position vector of any arbitrary location in XYZ frame [3]. This relationship leads to the conservation of momentum principle (1.2) since velocity vector $\mathbf{U}$ is the total time derivative of the position vector as:

$$\frac{d}{dt}\frac{\partial L}{\partial \mathbf{U}} = \frac{d}{dt}\mathbf{P} = 0 \tag{1.2}$$

2

Momentum can be expressed in any frame via relative velocity analysis due to the fact that position or velocity vectors in a reference frame can be expressed with a vector originating in another reference frame [4]. This formulation (1.3) will be cherished for moving mesh interpretation throughout following chapters:

$$^{R1}\mathbf{r}^{P2} = {}^{R1}\mathbf{r}^{R2} + {}^{R2}\mathbf{r}^{P2} \tag{1.3}$$

where superscripts $R1$, $R2$ represent two reference frames and $P1$, $P2$ are arbitrary locations on these frames.

Conservation of momentum can be interpreted as a combination of conservation of energy and mass. It can also be derived from equation of motion on a control volume for fluidic applications as an interpretation of Newton's second law of motion [5] and expressed with non-isothermal effects as in:

$$\rho \frac{DU_i}{Dt} = \rho F_i - \frac{\partial P}{\partial X_i} + \frac{\partial}{\partial X_i}\left\{ 2\mu\left(e_{ij} - \frac{1}{3}e_{ii}\delta_{ij} \right) \right\} \tag{1.4}$$

$$\frac{DU_i}{Dt} = \frac{\partial U_i}{\partial t} + \left(\mathbf{U}\cdot\nabla \right)U_i \tag{1.5}$$

$$e_{ij} = \frac{1}{2}\left(\frac{\partial U_i}{\partial X_j} + \frac{\partial U_j}{\partial X_i} \right) \tag{1.6}$$

$$e_{ii} = \nabla\cdot\mathbf{U} \tag{1.7}$$

$$\delta = \begin{bmatrix} 1 & 0 & 0 \\ 0 & 1 & 0 \\ 0 & 0 & 1 \end{bmatrix} \tag{1.8}$$

where D/Dt is called "material derivative" [5], e_{ii} is called "volumetric strain rate" [6], μ is dynamic viscosity, ρ is the density, P is pressure and F is body force. Conservation of mass on the other hand is derived from continuity equation which encompasses the compressibility effects (1.9) as:

$$\frac{\partial \rho}{\partial t} + \nabla\cdot(\rho\mathbf{U}) = 0 \tag{1.9}$$

3

Obviously for incompressible fluids, equation (1.9) will reduce to equation (1.10) which would eliminate the volumetric strain rate expression (1.7) as:

$$\nabla \cdot \mathbf{U} = 0 \tag{1.10}$$

The viscous dissipation inside a compressible fluid is known to be modeled in two dimensions [7] as:

$$\mu\Phi = \mu\left\{\left(\frac{\partial u}{\partial Y} + \frac{\partial v}{\partial X}\right)^2 + 2\left(\left(\frac{\partial u}{\partial X}\right)^2 + \left(\frac{\partial v}{\partial Y}\right)^2\right) - \frac{2}{3}\left(\frac{\partial u}{\partial X} + \frac{\partial v}{\partial Y}\right)^2\right\} \tag{1.11}$$

which is equal to zero for an incompressible and isothermal flow, which is suitable for locally-constant-temperature environments like human body. Thus Navier-Stokes equation reduces to (1.12) in vector form for incompressible-isothermal-Newtonian fluids as:

$$\rho\frac{D\mathbf{U}}{Dt} = -\nabla P + \rho g + \mu\nabla^2\mathbf{U} \tag{1.12}$$

1.2 Non-dimensional Approach and Implications of Reynolds Number

Non-dimensionalization procedure transforms the dimensional Navier-Stokes equations into a non-dimensional equivalent which allows the solution to be purely numeric. This way, physical characteristics of the flow are determined by a series of dimensionless number groups. First step is to select characteristic scales for each physical quantity, i.e. for dimension, ℓ_0, for time, t_0 and for pressure, P_0. These factors are used to obtain the dimensionless form of physical quantities as $X^* = X/\ell_0$, $t^* = t/t_0$ and $P^* = P/P_0$, also resulting in $\mathbf{U}^* = \mathbf{U}t_0/\ell_0$ hence where '*' denotes dimensionless quantities. Substituting these dimensionless quantities in equation (1.12) and rearranging the constants yields equation (1.13) as:

$$\frac{D\mathbf{U}^*}{Dt^*} = -\frac{P_0}{\rho\left(\ell_0/t_0\right)^2}\nabla^* P^* + \frac{\ell_0}{\left(\ell_0/t_0\right)^2}g + \frac{1}{\rho\left(\ell_0/t_0\right)\ell_0}\mu\nabla^{*2}\mathbf{U}^* \qquad (1.13)$$

Equation (1.13) is dimensionless Navier-Stokes where dimensions of each constant group have cancelled out each other. The most important dimensionless group among these is the Reynolds number [5] where $U_0 = \ell_0/t_0$ as in:

$$\mathrm{Re} = \frac{\rho U_0 \ell_0}{\mu} \qquad (1.14)$$

which corresponds to the ratio of inertial forces to the viscous (surface) forces. Re number is the dominant factor in transition between laminar and turbulent flow as well as the transition between laminar flow and creeping flow where inertial forces can be neglected [8]. Navier-Stokes equations reduces into Stokes Equations (1.15) where there must be an acceleration expression only if Re < 1 is considered to be suitable for creeping flow analysis due to the existence of density term [8], which is going to be determined to be the actual situation.

$$\rho\frac{\partial\mathbf{U}}{\partial t} = -\nabla P + \mu\nabla^2\mathbf{U} \qquad (1.15)$$

Equation (1.15) can be transformed into dimensionless form by $\rho = 1$ and $\mu = 1/\mathrm{Re}$ replacement which automatically changes the interpretation of other terms from dimensional to dimensionless form considering that $\rho\left(\ell_0/t_0\right)^2 = P_0$. Re < 1 has an important outcome on physical explanation of fluid flow. Elimination of body forces means pre-acquired velocities are not that effective on general behavior. In real life when a driver brakes, his or her inertia wants to keep moving but in micro realm surface forces do not allow the inertia to be dominant so when a microscale driver brakes, he or she would stop almost instantaneously; furthermore as long as Re number is smaller than 1, dimensions are not important and surface forces will be dominant [9]. Hence the question of artificial mobility in microrealm, in other words propulsion in fluidic media with low Re number, arises.

CHAPTER 2

BACKGROUND

After introducing the basics of fluid analysis, it is necessary to review systems handling fluid volumes by means of various methodologies in microscales; either man made or via natural solutions. Hence, this part of the work is divided into two main sections one of which is dedicated to a brief review of pump mechanism and their working principles by introducing key elements of their conceptual designs without getting into mathematical details. Following section focuses on microswimmers; mainly the overview of the theoretical work done so far to explain how and why microswimmers swim the way they do. Finally a few examples from the literature will be discussed.

2.1 Micropump Systems

Since fluid and structure interaction in micro realm is a much different issue than in macro world as briefly introduced in the previous section, micro pump mechanisms differ from their macro ancestors due to the fact that qualities scale down not only for fluids but other mechanical and electrical systems such that well known behaviors change, some of which will be introduced during this short review of micro pumps. Following, micro pump systems are divided into two subcategories, as mechanically and electrically driven, in an unconventionally way which will be evident through the end. Mechanically driven micropumps are usually of displacement pump fashion as depicted in Figure 2.1.

2.1.1 Mechanically Driven Micropumps

Mechanically driven micropumps are based on fluid structure interactions such that form of a mechanical energy stored is released from the structure, penetrating into the fluid by means of momentum flux as explained in conservation of momentum discussion. Most common mechanical micropump structures can be roughly separated as Piezo-displacement micropumps, thermally driven micropumps, pneumatic micropumps, rotary/centrifugal micropumps, electrostatic micropumps and mechanically induced traveling wave micropumps. There are of course several other distinctive types [10].

2.1.1.1 Piezo-displacement Micropumps

Piezo-displacement micropumps work with the very idea of contracting and expanding the fluid volume inside the pump reservoir [10]. These reservoirs are covered with a thin membrane on top and connected to the outside world by two micro channels. In general, piezo materials can be used both as strain [11] or stress sources, i.e. as a strain source a piezo material is mounted on top of the membrane and essentially responsible for the volume change of the pump reservoir due to its ferroelectric capabilities [12], hence transforming applied electric field into deformations which will be discussed in detail later on. Piezo materials allow high driving frequencies and materials like silicon or glass are commonly used due to their fast response abilities and relatively higher stiffness [10] but they are not capable of large deformations since piezo materials are generally brittle [10], [13]. If reservoirs are to be connected in series, then it is possible to control the flow without any valve structure [10]. Otherwise different check-valve mechanisms may be needed to control the flow inside the pump. Although valve systems are beyond the scope of this work, it is crucial to stress that check valves complicate the micro fabrication process [14], [15].

2.1.1.2 Thermally Actuated Micropumps

Thermally driven micropumps are conventionally considered as a member of micropumps category because strain source is an auxiliary fluid within a second chamber on top of the main reservoir, in which heat interaction takes place resulting in

series of expansion and contractions [10]. Both chambers are separated by a flexible membrane which couples the stroke effects from second chamber to the main reservoir. Although in micro scales heat diffusion takes shorter time, it is not possible to introduce and extract heat rapidly without uninvited losses. Hence thermally driven micropumps can not operate at high frequencies [10], [13]. Such pumps are capable of relatively higher stroke volumes which are apparently restricted with the deflection limits of the separating membrane [16]. In addition to second chamber approach, it is also possible to employ heat flow upon shape memory alloys to create desired periodic volume variations on the reservoir without the need of an auxiliary fluid [17] but driving frequencies are still low for these kind of designs due to same heat flow characteristics. Desired heat for either fluidic expansion or shape memory alloy expansion-contraction can be harvested from Joule heating [18] which will not be discussed here.

2.1.1.3 Pneumatic Micropumps

Pneumatic micropumps are considered as an other member of the displacement pump family and are in need of an external pressure source and extensive valve structures to operate [10], [19] since valve operation frequency is actually the driving frequency of the micropump. Like thermally driven micropumps, pressure is introduced into the secondary chamber leading a deflection on the separator membrane in between the secondary chamber and main reservoir. Separating membrane properties once again limits the maximum possible deflection. Moreover, this design may need two sets of valves, i.e. one pair to control the external pressure source actively and another pair to control the flow inside the main reservoir passively. Due to high surface forces, the cycling effect on active valves may cause increased failures as in MEMS switches used [20] in microwave systems and needs to be extensively designed to achieve longer operation capacity.

2.1.1.4 Rotary/Centrifugal Micropumps

Rotary/Centrifugal micropumps are not necessarily working with the same common principle but they generally include at least one free rotating part to create desired effect on the fluid. Because of this reason they form a completely different category and no matter how differently they are actuated they finally transform

mechanical energy of the rotating part into kinetic energy of the fluid by means of momentum diffusion. They are used mostly for highly viscous fluids [10]. There are several designs such as planetary gear micropump driven by electrostatic comb driver [21], [22], gear micropump driven by small scaled electromagnetic motor in high frequencies [23], eccentric cylinder rotation in micro channels [24] and impeller rotation to create suction effect inside a cylindrical reservoir [25]. These designs are more complicated and expensive due to the fact that rotating parts can be mostly micro fabricated by LIGA technique [13].

2.1.1.5 Electrostatic Micropumps

Electrostatic micropumps belong to the mechanical micropumps category because of their actuation principle. The electrostatic force between two loaded membranes which actually constitute a capacitor is balanced with natural spring force of one of the membranes and under proper conditions this system shows a harmonic oscillatory behavior if constantly fed by a power source [18]. This behavior lets the deflecting charged membrane to act as a reciprocating membrane on top of a reservoir [26] much like as mentioned in piezo or thermally and pneumatic driven micropumps and force the flow by mechanical energy transfer.
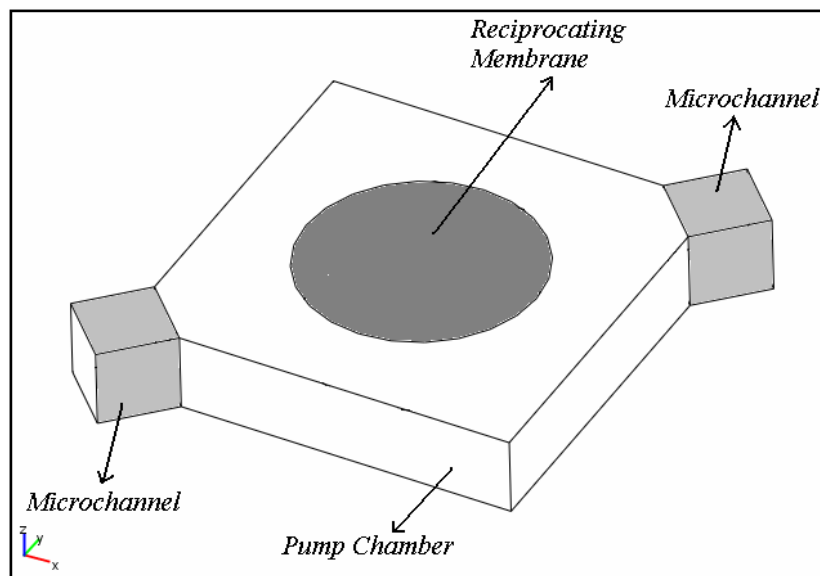
Figure 2.1: Conceptual displacement pump design

2.1.1.6 Mechanically Induced Traveling Wave Micropumps

Mechanically induced traveling wave micropumps are based on an entirely different concept. Mechanical energy is introduced into the fluid by means of periodic sinusoidal deflections of various amplitudes, wavelength and driving frequencies [27]. This creates consequently shifts in pressure and shear zones to force the fluid in the vicinity of the structure to flow. There are two widely known ways to create such an effect. Surface acoustic waves (SAW) can be utilized via inter-digital transducer structures [28] on a thin elastic structure inside a microchannel [29] or out-of-phase ferroelectric materials can handle such deformations under applied electric fields to introduce traveling waves into the fluids [30]. However due to the nature of SAW and especially piezo ceramic materials, these systems should operate with high frequency and small amplitudes.

On the other hand, a very interesting study on traveling wave pumps was carried out by Shapiro *et al.* (1969) which is actually about a mechanically induced traveling wave pump for viscous fluids with an efficiency of almost as much as 70% but unfortunately frequency data here was claimed to be "several waves per minute (Table 2)" rather than a specific value. System was composed of a macro scale rotating wheel and adjustable fingers attached to the sides such that as rotation takes place finger structures would introduce deformations on the flexible channel wrapped around the disk within a constant distance [31]. Although channel was very long, i.e. 30 cm, inside diameter was claimed to be at most 0.5 cm. Indeed, a system with such dimensions can not be considered as a micropump but the actuation principle and regime is quite inspiring due to the fact that Re < 1 condition is satisfied. Extensive results on traveling wave actuation will be discussed in following chapters since the actuation mechanism proposed for the micro propulsion system in this work is the traveling wave method. But to make the proper distinction in advance, it must be pointed out that proposed traveling wave actuation mechanism does not require a reservoir, a valve mechanism or a rotating part but theoretically a sole composite film structure of preferable dimensions and yet is capable of supplying controllable steady flows with relatively high deformations.

2.1.2 Electrically Driven Micropumps

These systems are designed in such a way that they minimize the necessity of secondary mechanical energy conservations before introducing the kinetic energy into the fluid but directly interact with the fluid itself. There may be some other systems to be considered controversial according to this definition, that is to say categorizing as pure electrically driven or mechanically driven may be tough. Hence the preferred choice is to limit this section with pump systems based on forces concerning pure electrohydrodynamic or magnetohydrodynamic interactions. There exist three subtitles in this section, i.e. electrohydrodynamic micropumps, electroosmotic micropumps and magnetohydrodynamic micropumps.

2.1.2.1 Electrohydrodynamic (EHD) Micropumps

These pumps rely on a very complex and extended interpretation of Coulomb force acting on the free ions inside the fluids such that applied electric field on dielectric fluids (with not only mobile ions inside but a more general interaction encompassing the polarization, permittivity and temperature effects) results in a non-uniform volumetric force which compels the flow [10]. There are three distinctive sub categories of EHD micropumps: If electric field is applied on the fluid results in induction inside the fluid that it is called induction EHD pump [32], if applied electric field results in dislocation of ions inside the fluid than this system is referred to as conduction EHD pump [33] and finally if ion exchange occurs between electrode structures and the fluid under high electric fields than this system is referred to as injection EHD pump [34]. In either case viscous interaction between the ions and rest of the fluid causes the net flow [10].

2.1.2.2 Electroosmotic Micropumps

Electroosmotic phenomena takes place in the vicinity of charged surfaces since there exists a charged boundary layer which can be forced to move by external electric fields [10]. This phenomenon is modeled by introducing the electric field into Navier-Stokes equations in which inertia and pressure is neglected due to capillary action [35]. That is to say as in the previous section net flow occurs due to shear interaction between

11

ions inside the so called charged boundary layer and the rest of the fluid causing the electroosmotic pumping effect [36].

2.1.2.3 Magnetohydrodynamic (MHD) Micropumps

Magnetohydrodynamic micropumps are based on the Lorentz force principle [10] which dictates that charged particles moving within an electrical field would feel a certain force acting on them causing a deviation in their path while entering a magnetic field with certain orientation [37]. This interaction finally results in pumping effect if this phenomenon takes place in fluids within a proper geometry [38]. These systems are not suitable for high viscous fluids since efficiency drops due to viscous forces [10].

2.1.3 Areas of Use

This part will briefly present the micropump exploited areas with technical data readily supplied by the designers/producers with some intrinsic inspirations. As one may expect, the most important field of study for micropump technology is medical applications. There are several examples of micropumps used directly for health care. An electrostatic pump design was made by Bourounia *et al.* (1996) for drug delivery applications. Proposed system was 5 mm by 5 mm with a membrane of 2 mm by 2 mm in dimensions. Under 10 V driving potential, it has the capability of operating with driving frequencies more than 1 KHz with certain types of fluids and supply a flow rate in range of 10 to 100 nl/min [26]. Another design was carried out by Cao *et al.* (2000) where the overall system was an implantable apparatus with a micropump consisting of three pump chambers connected in series. Each chamber is 90 μm in depth with 12 mm in diameter. Connecting channels are 2 mm x 10 mm rectangular openings. Each chamber has 80 μm thick membranes connected to PZT materials, which supply 10 μl/min flow rate at 0.5 Hz driving frequency [39]. A more comprehensive study was made by Polla *et al.* (2000) according to which medical micro systems can be categorized into three subcategories which directly utilize micropumps, i.e. surgical microsystems, therapeutic microsystems and diagnostic microsystems. An example to surgical microsystems is the study carried out by Meyns *et al.* (2000) which concentrates on micropump exploitations during beating heart CABG operations [42] as myocardial support systems [43]. On the other hand diagnostics microsystems are

basically "lab on a chip" designs [44] to analyze biochemical materials such as in conducting tests on blood sample in order to search malaria [45].

Other than medical applications there are some interesting areas where micropumps are extensively used or promising for future use. For instance the Ph.D. thesis study made by Tao Zhang (2005) is entirely focused on fuel delivery systems based on piezo driven valve-less displacement micropumps integrated with fuel cells [46]. Another area is microelectronic cooling where high flow rates, i.e. more than 100 ml/min liquid flow, are preferable [47]. Finally, a very interesting and the most relevant area of use is micropropulsion [48] in space where micropumps are expected to work on "ion-based" fluids with a flow rate of 1 ml/min [10] to create the necessary thrust effect for small scale space vehicles.

As a final addition to this list, reader may recall from the movie 'The Hunt for Red October' (1990) that the Russian submarine 'Red October' had a magnetohydrodrive system called "silent drive" which was actually so silent to hear for it had no moving parts to create thrust. The reason why such methods are not preferable as a micro-propulsion system in micro fluids is because of the high shear forces overcoming the electric or magnetic forces [10]. High shear issue will be discussed in detail in following chapters, during numerical results discussions.

2.2 Microswimmers: Biology and Math

Natural swimmers are no doubt wondrous creatures if not perfect due to the fact that they are fond of their harsh environment and limited energy sources. Maybe the only plagiarism to be pardoned is imitating the nature, copying the solution presented by living creatures. Thus this section is dedicated to a rather detailed review, especially for planar wave propagation method occupying swimmers for they are definitely the natural inspiration for this thesis work.

2.2.1 Propulsion Methods of Natural Microswimmers

One of the most comprehensive studies on micro propulsion (or locomotion) was carried out by Brennen and Winet (1977). According to their study, natural swimmers utilize so called "contractile" organelles which can be classified into four main groups, i.e. with the exact words "prokaryotic flagella, cytoplasmic filaments or microtubules,

eukaryotic cilia and flagella, and smooth or striated muscle". In this work for the mean focus is on the distinction between helical rotation drive and planar wave propagation drive, again unconventionally, the classification above will be divided into two main parts, i.e. helical rotation (or in a sense, helical wave propagation) and planar wave propagation. Although there are some single celled organisms utilizing both techniques [50], this context is omitted in this content.

2.2.1.1 Helical Wave Propagation

Although their composition and energy source may differ, helical rotations are carried out by both eukaryotic and prokaryotic flagella structures. Prokaryotic cell [51] flagellums are mounted on the cell walls with "hook-basal body complex" [52]. Bacterial flagellum has four rings in so called hook-basal body complex, two of which are mounted on cytoplasmic membrane under the cell wall and actuation for the rotation of the flagellum takes place in between. The other two rings are mounted in the cell wall responsible for attaching the flagellum to the cell wall [50] which is actually a very interesting organization due to its similarity to the bearing mounting [53] where bearings are used to protect the motor shaft from excessive bending stresses and torsion to keep motor structure intact during operation. Energy source of these rotating rings are not necessarily ATP molecules [54] and they rotate the flagellum as a rigid body, if the fluid forces on the structure is omitted. For instance, *spirochaetes phylum* members exploit this type of propulsion [50], e.g. *Cristispira balbiani* has more than 100 flagella, each approximately 21 μm in length and a body of 80 μm (total 101 μm) [55]. Figure 2.2 is a colored picture of *Treponema pallidum spirochetes*, another prokaryotic single celled organism, with helical tails [56].

On the other hand, helical wave propagating eukaryotic single celled organisms employ ATP molecules as energy source [50]. An example to this type of single celled organisms is *Rhabdomonas spirallis* [57], having helical flagella of 15 μm in length and body of 40 μm (total 55 μm). Hydrodynamics of helical rotations (or helical wave) are beyond the scope of this text but reader can find extensive analysis on the issue in the study carried out by Higdon (1978).
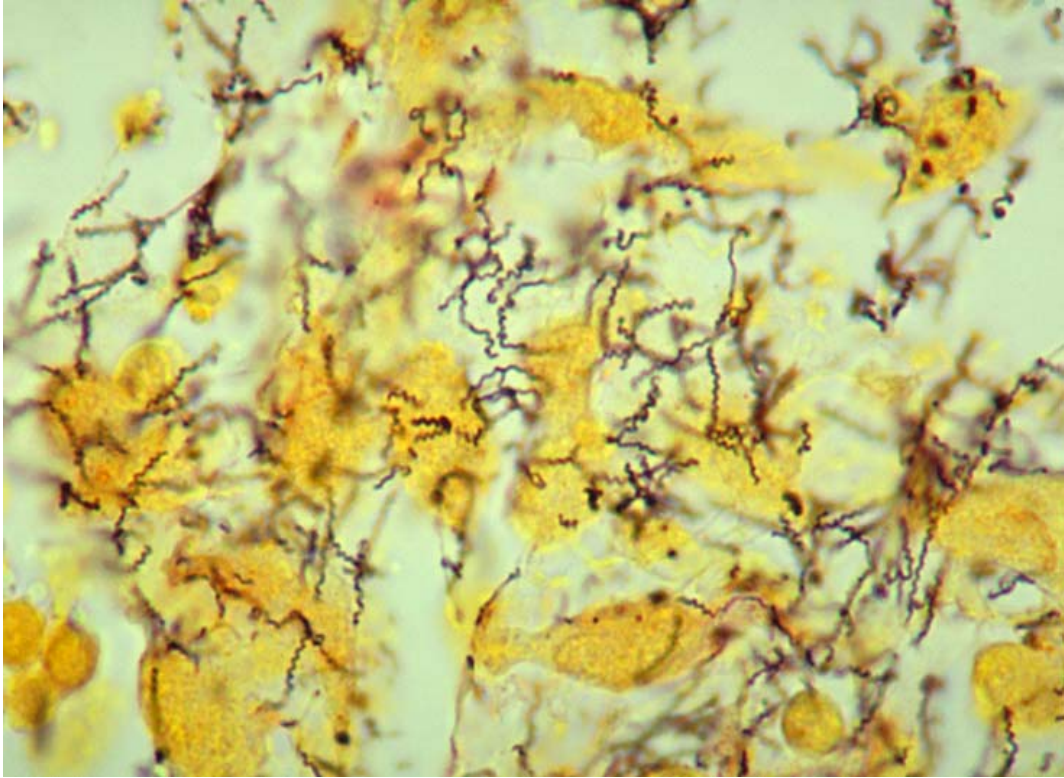
Figure 2.2: *Treponema pallidum spirochetes* [56]

2.2.1.2 Planar Wave Propagation

Planar wave propagation is used mostly by eukaryotic [51] cells and the main energy source is known to be ATP molecules [50]. Planar wave propagation is possible due to the "sliding filaments" inside the eukaryotic flagella or cilia structure via a series of interactions between sub-layers [59]. Wave propagation direction is generally from base to tip [50] but there exist opposite cases [60] where propagation direction is from tip to base. Also, in most of the cases direction of propulsion happens to be in the opposite direction of the wave propagation [50] but propagation and propulsion can also take place in the same direction regarding to the swimmers natural design i.e. in some single celled organism there are row like structures called "mastigoneme" perpendicular to the flagellum which results in forward thrust [61]. Most of the spermatozoa cells employ planar wave propagation, e.g. *Lytechinus* (sea urchin) with a flagellum of 37.5 µm in length and a body of 5.1 µm in length (total 42.6 µm) where ratio of propulsion speed to the wave propagation speed is 0.185 and wave amplitude is 4.6 µm [59]. Another example can be *Colobocentrotus* (sea urchin) with a flagellum of 45 µm in

length and a body of 8.2 μm in length (total 53.2 μm) where ratio of propulsion speed to the wave propagation speed is 0.237 and wave amplitude is 2.8 μm [62].

Having introduced the planar wave propagation concept, it is the next step to get into the planar wave mathematics to understand how it interacts with the surrounding fluid and creates the thrust effect.

2.2.1.3 Mathematical Model for Planar Wave Propagation Based Propulsion

A great body of work has been carried out to explain the basics of planar wave propagation, both from fluid and structure perspectives. Although numerical results presented in this work are entirely concerned the fluidic perspective, it will be evident that it also constitutes the base for future structural analysis.

2.2.1.3.1 Fluidic Perspective

Macro scale fish propel and maneuver themselves with systematic utilization and control of their tail and set of specialized fins which fluid drag depends on [63] but in micro scale a fish like swimming is not possible for scallop theorem states that time reversible motion results in no net propulsion due to high viscous forces against relatively negligible inertial forces [9]. The ratio between shear and inertial forces is quantified by the Re number, equation (1.16), mentioned through the end of the introduction. Although microswimmers are three dimensional creatures despite their size, first mathematical analysis was carried out for two dimensional assumptions for sake of simplicity and the analysis carried out by Sir Taylor (1951) is a symbol of a cornerstone among these.

First of all, the stream function definition must be introduced to be able to continue any further. A stream function is actually the mathematical representation of the time and coordinate dependent trajectory of fluid packets since it is always tangential to the local velocity vector thus velocity components can be found by spatial derivation of it (2.1) [5] and must satisfy (2.2) for irrotational plane flow [6] as:

$$\begin{bmatrix} u \\ v \end{bmatrix} = \begin{bmatrix} \dfrac{\partial \Psi}{\partial Y} \\ -\dfrac{\partial \Psi}{\partial X} \end{bmatrix} \tag{2.1}$$

$$\nabla^2 \Psi = 0 \tag{2.2}$$

Sir Taylor (1951) reminded that any stream function representing a flow field passing over a body in two-dimensional world must also obey (2.3) for inertia neglected viscous flow as in:

$$\nabla^4 \Psi = 0 \tag{2.3}$$

After it is suggested that no-slip boundary conditions must be invoked on the boundary of a waving thin membrane in contact with a viscous fluid only on one side, equation (2.4) is proposed to model the waving phenomena. No-slip condition implies that fluid molecules on the surface will move if and only if the surface moves as shown:

$$\begin{bmatrix} -\dfrac{\partial \Psi}{\partial X} \\ \dfrac{\partial \Psi}{\partial Y} \end{bmatrix} = \begin{bmatrix} -B_o \omega \cos(kX - \omega t) \\ 0 \end{bmatrix} \tag{2.4}$$

where B_o is the maximum possible wave amplitude, k is the wave number ($= 2\pi/\lambda$), ω is the angular frequency ($= 2\pi f$) with f denoting the driving frequency and λ is the wavelength. This surface velocity vector represents a sinusoidal 'waving action', i.e. continuous propagation of a sinusoidal wave on the surface. Another interpretation of equation (2.4) is inextensibility of the sheet which is why the small amplitude assumption (i.e. $B_o k \rightarrow 0$) with $Y \rightarrow 0$ statement was invoked, to obtain the following expression (2.5) for the stream function [64]:

$$\Psi = -\frac{B_o \omega}{k} (1 + kY) e^{-kY} \sin(kX - \omega t) \tag{2.5}$$

Equation (2.5) is important because one can find the pressure expression under the assumption that all inertia dependent variables in the incompressible isothermal Navier-Stokes equations (1.12) are ruled out which results in a new equation, known as the Stokes equations (2.6) [65] stating that fluid is in static equilibrium in stress-wise since explicit time and trajectory dependence is lost as can be observed:

$$\mu\nabla^2\mathbf{U} = \nabla P$$
$$\nabla\cdot\mathbf{U} = 0$$

(2.6)

If equation (2.4) is substituted in equation (2.6) and re-written for only X-direction, then the following expression (2.7) is obtained [66]:

$$\frac{\partial P}{\partial X} = \mu\nabla^2\frac{\partial\Psi}{\partial Y}$$

(2.7)

Integrating both sides with respect to X yields pressure formulation presented by Sir Taylor (1951) as in (2.8):

$$P = 2\omega B_o k\mu e^{-kY}\cos(kX - \omega t)$$

(2.8)

which actually may appear to be a controversial result since (2.7) seems to omit the fact that inertia can be omitted but flow is still unsteady due to the time term 't' inserted in (2.4). Batchelor (1967) pointed out this issue and underlined that when neglecting the inertia, convection term in Navier-Stokes equations drops completely only if flow is steady or $\partial\mathbf{U}/\partial t$ is smaller than the rest (i.e. $\mathbf{U}\cdot\mathbf{grad U}$) [67] which brings the small amplitude assumption of Sir Taylor's (1951) analysis in to the picture one more time. In order to avoid a possible disagreement, an acceleration correction has been made in (2.6) and numerical setup of the problem during Stokes solutions as will be pointed out again.

$$\sigma_{YY} = \left(-2\mu\frac{\partial^2\Psi}{\partial Y\partial X} - P\right)$$

(2.9)

$$\Pi = \frac{1}{A}\int_A \sigma_{YY}\frac{\partial\Psi}{\partial X}dA$$

(2.10)

Exploiting the mentioned pressure expression (2.8) within the principle-Y-stresses component in the full stress tensor (2.9) [68] and substituting the new principle-Y-stress expression into (2.10), Sir Taylor (1951) had found the rate of work for described waving action per unit area to be proportional to $\mu B_o^2 \omega^2 k$ (i.e. $\sim B_o^2 f^2/\lambda$) for small amplitude assumption. Also, ratio between the propagation velocity and resultant upstream flow velocity found to be proportional to $2\pi^2 B_o^2/\lambda^2 - 9.5\pi^4 B_o^4/\lambda^4$ (i.e. $\sim B_o^2/\lambda^2$ without higher order terms) via solution to the series expansion of the stream function to the fourth power of the amplitude for large amplitude case [64] using perturbation method [6]. These results also coincide with the ones represented later on by Gray and Hancock (1955) and Childress (1981).

The work published by Katz (1974) extended the analytical study from inextensible sheet with one surface in contact with fluid assumption to extensible sheet with both surfaces in contact with fluid assumption [70]. Updated version of velocity equations used for no-slip boundary conditions included the propulsion velocity of the sheet but again with small amplitudes invoking "combined biharmonic-lubrication-theory" [8] only to find the ratio between propulsion velocity and propagation velocity to be proportional to $\sim \lambda f B_o^2$, a kin to Taylor's and Childress's results, and energy consumption to be proportional to $\sim \lambda f^2$. The disagreement in the results of Sir Taylor's (1951) and Katz's (1974) on energy consumption, will be clarified with the numerical results to the parametric study of λ throughout following chapters, as well as the consequences of inextensibility approach.

Extending the analytical analysis on resulting propulsion velocity and energy/power need for the desired waving action, has led to the efficiency study for such swimmers. For large scale swimmers such as fish, the efficiency is proposed be to calculate by the expression (2.11) known as the Froude efficiency defined in terms of mean propulsion velocity, mean power requirement and mean forward push, i.e. F_p [63], assuming that net propulsion is in X-direction as in:

$$\eta = \frac{\langle u_p \rangle \langle F_p \rangle}{\langle \Pi \rangle} \qquad (2.11)$$

Propulsion velocity u_p is obviously the velocity of the center of the mass of the swimmer and unfortunately can not be precisely calculated analytically for all cases. But

there exists an important criterion (2.12) imposed by Gray and Hancock (1955) on local propulsion velocity for any arbitrary point to provide instantaneous thrust on the tail as follows [69]:

$$\frac{\partial \Psi}{\partial X} > u_p \frac{\partial}{\partial X}\left(\int \frac{\partial \Psi}{\partial X} dt\right) \qquad (2.12)$$

Sir Lighthill (1975) has suggested a very similar form of efficiency for microswimmers by introducing the concept of tangential and normal forces (i.e. $K_{\parallel}, K_{\perp}$) on the swimmer surface. The significant difference on the proposed formulation was in the interpretation of F_p ; e.g. thrust force and power need was both formulated based on the total motion done by the swimmer hence both tangential normal forces were introduced in all expressions making them rather complicated.

Stone and Samuel (1996) re-interpreted Sir Lighthill's (1975) efficiency definition into a form closer to Sir Taylor's (1951) interpretation and suggested the generalized form of hydraulic power (2.13) consumed by "swimming stroke" as:

$$\Pi = -\int_{S(t)} \mathbf{n} \cdot \boldsymbol{\sigma} \cdot \mathbf{U} dS \qquad (2.13)$$

where S is time dependent surface, $\mathbf{n}$ is the surface normal vector and $\boldsymbol{\sigma}$ is the total stress tensor.

A more stronger distinction has been made by Wiggins and Goldstein (1998) who defined the efficiency as the ratio between power consumption for net propulsion in X-direction (2.14) and power consumption for transverse motions (2.15) for the so called "Elastohydrodynamic Problem II"; e.g. the swimmer with both ends free and waving motion is propagated from head to tail with a dissipative effect. Although the interpretation is exactly same, since the problem definition is unique, efficiency formulation is almost entirely different [73] as shown:

$$\Pi_{\parallel} = u_p \frac{\zeta_{\perp} \omega}{2\pi} \int_0^{2\pi/\omega} \left(\frac{\partial Y(X_f,t)}{\partial X} \frac{\partial}{\partial t}\left(\int_0^{\ell_f} Y(X_f,t) dX \right) \right) dt \qquad (2.14)$$

$$\Pi_\perp = \int_S \left(\zeta_\perp \left(\frac{\partial Y(X_f, t)}{\partial t} \right)^2 \right) dS \tag{2.15}$$

where $Y(X_f, t)$ is the Y-position function of any arbitrary point on the tail, $\zeta_\perp$ is the normal viscous drag coefficient [74], ℓ_f is the length of the tail.

Additionally Sir Lighthill stressed that microswimmers are bounded to have low efficiencies due to their propulsion methods [71]. Purcell (1976) made a similar discussion about how small the efficiency of microswimmers even with optimal conditions is [9]. This last discussion on efficiency actually concludes the basics of planar wave model from a fluidic point of view.

2.2.1.3.2 Structural Perspective

Although structural analysis is not covered in the numerical study, some introductory elements will be revealed for the sake of a more comprehensive background, very briefly. Taylor (1951) suggested it would be possible to determine the moment on a tail like structure by invoking the static beam deflection equations (2.16) from Euler-Bernoulli Beam Theory [75] as:

$$\frac{dF_\perp}{dX} = -P; \quad \frac{d\mathrm{M}}{dX} = F_\perp \tag{2.16}$$

where $F_\perp$ denotes the normal stress and M denotes the moment on the tail. Nevertheless pressure is not the only concern obviously. Childress (1981) gave the two dimensional stress tensor (2.17) for fluid exerted forces [66] as:

$$\boldsymbol{\sigma} = \begin{bmatrix} -P + 2\mu \dfrac{\partial^2 \Psi}{\partial X \partial Y} & \mu \left(\dfrac{\partial^2 \Psi}{\partial Y^2} - \dfrac{\partial^2 \Psi}{\partial X^2} \right) \\[3mm] \mu \left(\dfrac{\partial^2 \Psi}{\partial Y^2} - \dfrac{\partial^2 \Psi}{\partial X^2} \right) & -P - 2\mu \dfrac{\partial^2 \Psi}{\partial X \partial Y} \end{bmatrix} \tag{2.17}$$

Regrettably, the stream function, Ψ, may change in time accordingly with the changing orientation of the swimmer and hence has to be modified with additional effects of a head or asymmetric channel geometry. Although stream functions can be superposed [5], necessity for a more common approach has been raised for analytical purposes. Slender body theory exploits the tangential and normal forces (i.e. $K_{\parallel}, K_{\perp}$) introduced in the previous section [50], [66], [69], [74], [76] as represented in equations (2.18) and (2.19) to calculate the forces acting on an infinitesimal part of the swimmer surface which are proportional to the fluid velocity as depicted:

$$K_{\parallel} = -C_{\parallel} U_{\parallel} dS \tag{2.18}$$

$$K_{\perp} = -C_{\perp} U_{\perp} dS \tag{2.19}$$

In equations (2.18) and (2.19), U is the generic local velocity of any infinitesimal part of the swimmer body (i.e. tail or head) or can be interpreted as the velocity of the upstream without any explicit orientation. $C_{\perp}$ and $C_{\parallel}$ are the resistive force coefficients [50] of the swimmer but are also known as the drag coefficient [74] as introduced in the previous section (i.e. $\zeta_{\perp} = C_{\perp}, \zeta_{\parallel} = C_{\parallel}$). These coefficients are usually in the following form, i.e. (2.19) and (2.20):

$$\zeta_{\perp} = \frac{4\pi\mu}{\ln(2a/b) + \wp_1} [\wp_2] \tag{2.20}$$

$$\zeta_{\parallel} = \frac{2\pi\mu}{\ln(2a/b) - \wp_1} [\wp_2] \tag{2.21}$$

where $\wp_1$ and $\wp_2$ are the geometry dependent higher order variables, a is major axis and b is the minor axis of the swimmer geometry [50]. In addition to the previous expressions for power and force calculations, normal viscous coefficient appears in two important formulations where surrounding fluid is correlated with structural behavior:

(i) In the hyperdiffusion constant inside the equation of elastohydrodynamics (2.22) [73] derived to explain the behavior of elastic tails in low Reynolds number medium as follows:

$$\frac{\partial}{\partial t}Y(X,t) = \frac{E}{\zeta_\perp}\frac{\partial^4}{\partial X^4}Y(X,t) \tag{2.22}$$

where E is the bending rigidity of the structure, i.e. $E/\zeta_\perp$ constitutes the hyperdiffusion constant.

(ii) Sperm Number (2.23), a quantity which defines the ratio between viscous forces exerted by the surrounding fluid and bending forces inside the tail structure [77] as:

$$\mathrm{Sp} = \left(\frac{\ell_f^4 \omega \zeta_\perp}{E}\right)^{1/4} \tag{2.23}$$

Sp number has three known outcomes [77]. As Sp → 0, u_p and η goes to zero, $u_{p\text{-max}}$ and η_{max} occurs where Sp ~4 and finally at very high Sp numbers, propulsion and efficiency becomes independent of Sp [77].

2.2.1.3.3 Examples from Literature

Microswimmer experiments or simulations are relatively immature comparing with all the analytical work done so far. However, there are few interesting examples on the experimental or simulation studies carried out recently.

Experimental data published by Dreyfus *et al.* (2005) embodies the most interesting study so far for the swimmer structure with the actuation mechanism choice of bounded living cell with an artificial organelle. The proposed swimmer structure is composed of a red blood cell and a magnetic tail composed of "streptavidin magnetic particles" and "dibiotin ds-DNA (315 bp)". This artificial tail is driven by external magnetic fields such that changing orientation of applied magnetic field results in beating motion, i.e. planar wave propagation, on the artificial tail structure. A parametric study was carried out to explain the relationship between magnetic field strength, velocity field and Sp number. Reported results show that maximum propulsion is achieved with Sp ~3 and dimensionless magnetic field of Mn = 4.5 with a driving frequency around 10 Hz and $\zeta_\perp = 4\pi\mu$ [78].

Another microscale experimental setup was used by Wiggins *et al.* to check the reliability of the analytical solution to the "elastohydrodynamic problem II". Here an "F-actin" connected to a spherical body. This structure is placed between two slides with only 20 μm apart. Structure is observed with a laser beam directed via a microscope objective. Experimental results for different driving frequencies and filament lengths were presented [74]. A very similar study has been carried out by Lagomarsino *et al.* (2003) including effect of Sp number and wave amplitude on propulsion velocity and effect of Sp number on swimmer efficiency, e.g. maximum efficiency was found to be almost 0.095 for Sp = 3 [77].

A different experimental design was carried out by Behkam and Sitti (2006) using macroscale helical tail. Although experimental setup was not small, silicone oil made it possible to work with small Re numbers i.e. Re < 1. Helical tail was actuated by a motor and three different designs with two different containers in size were used in to find out the effects on propulsion velocity and efficiency under parameterized design variables, i.e. diameter of the head piece, amplitude of helical waves and diameter of tail structure [79].

Conceptual design for a micro robot design was suggested by Edd *et al.* (2003) to be used for surgical applications. The propulsion mechanism was the rotary motion of a micro disc with several tail-like structures attached to one surface to simultaneously propagate helical waves due to the rotary action of the base. Normalized efficiency was found to be at most 0.025 under varying number of tail structures (i.e. 0-100), rotation angle (i.e. 0-90), driving frequency (i.e. 10 Hz – 100 kHz) and amplitude (i.e. 0-15 μm) [80].

CHAPTER 3

NUMERIC PROCEDURE

This chapter is dedicated to the numerical setup of the micropump and microswimmer models in detail as a foundation before the results of the parametric studies are presented. There will be a discussion on the most celebrated moving frame interpretation and its utilization. Preparing the groundwork for moving boundaries, first the necessary equations are derived for moving boundaries of 2D and 3D micro pump designs, thereafter equations corresponding to boundaries of the 3D swimmer model are derived. Finally the scheme to the boundaries of numerical scenarios will be clarified for all various cases.

3.1 Moving Boundaries: Mathematical Interpretation

Simulating the boundaries in motion is an important part of numerical study. The medium occupied by fluid is basically meshed by computer, with or without human interference, in order to solve the set of equations corresponding for every designated mesh nodes within finite element solution. When a physical problem, namely physical scenario, is given it is not feasible to solve the problem for every physical point on the system for it will surely occupy a great deal of time, effort and storage means. In order to solve a physical problem, the continuous medium is transferred into a simplified model composed of discrete points where the calculations would take place [81]. Numerical methods are widely used for solving differential equations which can form a system of linear equations that expressed in matrix form to be solved via certain procedures. Roots of system of differential equations for a physical model are simply the Eigenvalues to the matrix form of the same model [82]. Each mesh node is associated with a set of equation and each equation enters into the matrix to be solved. Each

unknown inside the matrix is called 'degrees of freedom'. Obviously, to be able to solve such a system, boundary conditions must be introduced to the mathematical model. Finite element models created in computer environment gives the user the freedom to define proper boundary conditions to designated boundaries of the simulated physical system.

Boundaries where fluid-structure interaction is taking place are hard to interpret for mutual force couples would result in stress and strain effect in the structural side as well as pressure and velocity fields in the fluid side of the model. When a boundary moves, mesh nodes on that boundary also move. When structural analysis is considered strain on a boundary is directly transferred to other boundaries under proper mathematical procedures unless a joint exists, as in Figure 3.1. On the other hand, when a fluidic analysis is carried out, motion of a boundary is not necessarily resulting in deformation of other boundaries hence stretching effect deforms the mesh elements on the corresponding medium as in Figure 3.2.
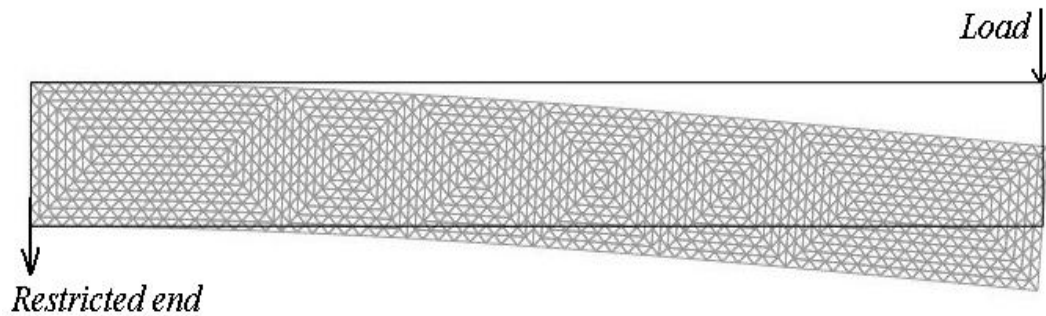
Figure 3.1: Cantilever beam, deformed geometry results in translated mesh nodes.
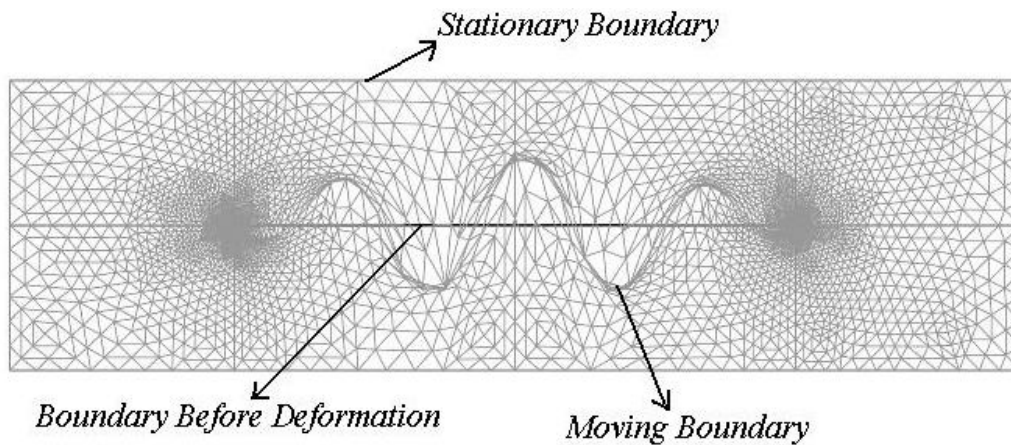
Figure 3.2: Moving boundary with compression and expansion effect on triangular mesh elements.

As it is demonstrated in Figure 3.2 deformed boundary may result in following mesh elements to deform. There are three numerical methods to model and interpret the mesh structure, i.e. to follow the medium. They are known as Eulerian, Lagrangian and arbitrary Lagrangian Eulerian method. Eulerian method [83] suggests rather fixed geometry size and shape while Lagrangian method [84] forces the whole mesh to move with the medium. Arbitrary Lagrangian Eulerian method makes it possible to force mesh follow the medium only near moving boundaries [85]. Since moving and non moving mesh coexists in the same medium at the same time, there must be a distinction between stationary frame and moving frame, also known as ALE frame. The motion in ALE frame is projected to the stationary frame thus into Navier-Stokes Equations (1.12). Due to the fact that the motion in material frame and motion in mesh frame are independent of each other there is a third common stationary fame of reference to be considered to be able to write the equation of motion properly [86]. Therefore, there are three velocity definitions to consider. One is the mesh velocity with respect to the stationary reference frame (3.1), second is the particle velocity with respect to the material reference frame (3.2) and the last one is the material velocity vector with respect to the reference frame (3.3). Together they form a transformation equation (3.4) which results in terms of the particle velocity with respect to the mesh velocity (3.5) as follows [87]:

$$\mathbf{u}_{\mathrm{m}}\left(\mathbf{X},t\right)=\left(\frac{\partial \mathbf{x}}{\partial t}\right)_{\mathbf{X}} \tag{3.1}$$

$$\mathbf{U}\left(\boldsymbol{\chi},t\right)=\left(\frac{\partial \mathbf{x}}{\partial t}\right)_{\mathbf{x}} \tag{3.2}$$

$$\mathbf{w}=\left(\frac{\partial \mathbf{X}}{\partial t}\right)_{\boldsymbol{\chi}} \tag{3.3}$$

$$\frac{\partial \varphi}{\partial\left(\boldsymbol{\chi},t\right)}\left(\boldsymbol{\chi},t\right)=\begin{pmatrix} \dfrac{\partial \mathbf{x}}{\partial \boldsymbol{\chi}} & \mathbf{U} \\ \mathbf{0}^{\mathrm{T}} & 1 \end{pmatrix}\begin{pmatrix} \dfrac{\partial \mathbf{x}}{\partial \mathbf{X}} & \mathbf{u}_{\mathrm{m}} \\ \mathbf{0}^{\mathrm{T}} & 1 \end{pmatrix}\begin{pmatrix} \dfrac{\partial \mathbf{X}}{\partial \boldsymbol{\chi}} & \mathbf{w} \\ \mathbf{0}^{\mathrm{T}} & 1 \end{pmatrix} \tag{3.4}$$

$$\mathbf{u}_{\mathrm{r}}=\mathbf{U}-\mathbf{u}_{\mathrm{m}}=\frac{\partial \mathbf{x}}{\partial \mathbf{X}}\cdot \mathbf{w} \tag{3.5}$$

where φ is the so called "particle motion function" [87] which is used to compute the mesh velocity, $\mathbf{X}$ denotes the reference frame, $\boldsymbol{\chi}$ denotes the material frame and $\mathbf{x}$

denotes the ALE frame and $\mathbf{u}_m$ is the mesh velocity vector. Finally the resulting relative velocity just computed can be used in Navier-Stokes equations and Stokes Equations such that moving mesh and unsteady moving boundaries are taken into account [87], [88], [89] as can be seen in equations (3.6), (3.7) and (3.8) respectively. These equations are solved with Winslow smoothing method [85], [90], [91] later on, i.e. another mathematical algorithm employed in mesh calculations (3.9); in order to satisfy (3.8) [85]. The reason how and why relative velocity enters the momentum equation was explained in the introductory section 1.4:

$$\rho\left(\frac{\partial \mathbf{U}}{\partial t}+\mathbf{u}_r\cdot\nabla\mathbf{U}\right)=-\nabla P+\mu\nabla^2\mathbf{U} \tag{3.6}$$

$$\rho\left(\frac{\partial \mathbf{U}}{\partial t}-\mathbf{u}_m\cdot\nabla\mathbf{U}\right)=-\nabla P+\mu\nabla^2\mathbf{U} \tag{3.7}$$

$$\nabla^2\mathbf{u}_m=0 \tag{3.8}$$

$$\frac{\partial^2}{\partial x^2}\mathbf{X}+\frac{\partial^2}{\partial y^2}\mathbf{X}=0 \tag{3.9}$$

3.2 Moving Boundaries in Pump Simulations

After clearing up the issue on moving mesh interpretation, moving boundaries of the pump system can be designated. Moving boundaries are actually the boundaries where dynamic structure and fluid interaction takes place. Since it is assumed that desired motion is prearranged, this section will cover the mathematical expressions for moving boundary conditions; Navier-Stokes / Stokes and ALE frame settings with 2D and 3D models which are solved via a commercial standalone finite element solver packet COMSOL® [92]. MATLAB®, another commercial package for simulations [93], is used to communicate with COMSOL®, i.e. without graphic user interface. Details on solution method will be given in successive sections.

3.2.1 2D Geometry

2D geometry (hence planar kinematics) has only 3 degrees of freedom for any point particle on the plane, i.e. translation on X and Y-axes and rotation around Z-axis.

Hence, pump design consists of a stationary waving membrane has only one motion design to consider for ALE and one motion design to consider for Stokes equations (3.7) which is the choice of governing differential equation for 2D pump simulations. In previous chapter waving function has been determined from the stream function Sir Taylor (1951) suggested [64]. From Stokes point of view, surface velocity of the waving membrane, mesh deformation speed, is also the no-slip boundary conditions for the fluid which states that fluid molecules are strictly following the boundary. On the other hand, time integration of the same equation gives the *Y*-translation of the mesh nodes on waving boundaries. Since both ends of the waving membrane are considered to be fixed, there is a parabolic envelope function (3.10) to determine the maximum amplitude with respect to time with an extra ramp function (3.10) to ensure that system starts from initial rest position. Hence modified Stokes and ALE boundary condition equations (3.12) – (3.16) [89], [94], [95] are given as:

$$B\left(X_f,t\right)=4B_{\mathrm{o}}\left(1-X_f/\ell_f\right)\left(X_f/\ell_f\right)\Re \tag{3.10}$$

$$\Re = \min\left(t,1/f\right) \tag{3.11}$$

$$y_f^{2D-p}\left(X_f,t\right)=B\left(X_f,t\right)\sin\left(\omega t-kX_f\right) \tag{3.12}$$

$$u_f^{2D-p}\left(x_f,y_f,t\right)=0 \tag{3.13}$$

$$v_f^{2D-p}\left(X_f,Y_f,t\right)=\frac{\partial Y_f}{\partial t}$$
$$=\left(\frac{\partial B\left(X_f,t\right)}{\partial t}\right)\sin\left(\omega t-kX_f\right)+\omega B\left(X_f,t\right)\cos\left(\omega t-kX_f\right) \tag{3.14}$$

$$u_{\mathrm{m}}^{2D-p}\left(X_f,Y_f,t\right)=0 \tag{3.15}$$

$$v_{\mathrm{m}}^{2D-p}\left(X_f,Y_f,t\right)=\frac{\partial Y_f}{\partial t}$$
$$=\left(\frac{\partial B\left(X_f,t\right)}{\partial t}\right)\sin\left(\omega t-kX_f\right)+\omega B\left(X_f,t\right)\cos\left(\omega t-kX_f\right) \tag{3.16}$$

where X_f and Y_f represent the time-dependent position of the thin-film with respect to the reference frame, ℓ_f is the waving film length and B_{o} stands for the maximum

possible amplitude value. Note that, although partial derivatives of Y_f and B with respect to X_f are non-zero, since X_f does not change with time, vertical component of the film velocity can be calculated from (3.14).

3.2.2 3D Geometry

Pump design in 3D geometry is not any different from 2D geometry except this time parabolic shape function is replaced with a hyperbolic shape function to ensure that one end is free and third axis comes into picture without any contribution to the motion [27] in equations (3.17) – (3.24) as:

$$B\left(X_f,t\right)= B_\mathrm{o} \tanh\left(X_f\right)\Re \tag{3.17}$$

$$y_f^{3D-p}\left(X_f,t\right)= B\left(X_f,t\right)\sin\left(\omega t - kX_f\right) \tag{3.18}$$

$$u_f^{3D-p}\left(X_f,Y_f,t\right)=0 \tag{3.19}$$

$$v_f^{3D-p}\left(X_f,Y_f,t\right)=\frac{\partial Y_f}{\partial t}$$
$$=\left(\frac{\partial B\left(X_f,t\right)}{\partial t}\right)\sin\left(\omega t - kX_f\right)+\omega B\left(X_f,t\right)\cos\left(\omega t - kX_f\right) \tag{3.20}$$

$$w_f^{3D-p}\left(X_f,Y_f,t\right)=0 \tag{3.21}$$

$$u_\mathrm{m}^{3D-p}\left(X_f,Y_f,t\right)=0 \tag{3.22}$$

$$v_\mathrm{m}^{3D-p}\left(X_f,Y_f,t\right)=4\left[\frac{1}{4}-\left(\frac{Y}{H}\right)^2\right]v_\mathrm{m}^{3D-p}\left(X_f,Y_f,t\right)=4\left[\frac{1}{4}-\left(\frac{Y}{H}\right)^2\right]\frac{\partial Y_f}{\partial t} \tag{3.23}$$

$$w_\mathrm{m}^{3D-p}\left(X_f,Y_f,t\right)=0 \tag{3.24}$$

It is noted that v_m^{3D-p} has an extra Y-component in it. This feature will prove useful within the section where boundary conditions are described with mesh deformation limit. One can notice that same ramp function was used to guarantee that system starts from stationary initial conditions. Mesh deformation data can be introduced to the model in two possible ways; one is providing the mesh deformation velocity on the boundary,

the other is providing the mesh deformation in the domain; although second choice was used for 3D pump model, it must be pointed out that either approach must satisfy (3.22), (3.23) and (3.24). All boundary conditions and initial condition data for both moving and nonmoving boundaries are provided in following sections.

3.3 Moving Boundaries in 3D Swimmer Simulations

Moving boundaries for swimmer constitute a more complicated problem to handle with respect to pump analysis since swimmer geometry is no more fixed and is taking full advantage of translation on *X* and *Y*-axes and rotation around *Z*-axis. Since swimmer is supposed to move free by means of force interactions with surrounding fluid, especially comparing with the pump simulations where structure is kept stationary with a presumed anchoring force, boundary condition equations are expected to be more complicated as will be observed in the following sections.

3.3.1 ALE Boundary Conditions for Moving Boundaries

Resultant motions of waving action on a tail can be simplified to 2D due to the fact that flow in the vicinity is symmetric with respect to *XY* plane so rotations in *X* and *Y*-axes are ruled out. Hence there are four distinctive motions to solve for and these can be expressed in two general equations, (3.25) and (3.26) which are combination of series of sub-expressions to mesh deformation [96] as follows:

$$dx_S = dx_\| + dx_\theta \tag{3.25}$$

$$dy_S = dy_w + dy_\perp + dy_\theta \tag{3.26}$$

where *X*-translation is denoted by $dx_\|$, *Y*-translation is denoted by $dy_\perp$, rotation components are denoted by dx_θ, dy_θ and finally waving motion is denoted by dy_w. These equations are known as the prescribed mesh deformation functions, i.e. motion of each mesh node is pre defined by user and as a result need for computational power is reduced. Also this method reduces the possibility of "inverted mesh" error which occurs if a mesh element gets twisted during deformation procedure [85].

3.3.1.1 Translations

Translation is the net pure displacement of the center of the mass to the swimmer in both X and Y-axes governed by the following equations. Unfortunately the below predefined mesh equations must satisfy that outer boundaries remain strictly stationary and a motion exists depending on swimmer dynamics [96] as:

$$dx_\| = x_\mathrm{m}\beta_x \tag{3.27}$$

$$x_\mathrm{m} = \iint F_X \, dt dt \,/\, M \tag{3.28}$$

$$F_X = \int_{S(t)} \Sigma_X dS \tag{3.29}$$

$$\Sigma_X = \begin{bmatrix} \left(2\mu\dfrac{\partial u}{\partial X} - P\right) \\ \mu\left(\dfrac{\partial u}{\partial Y} + \dfrac{\partial v}{\partial X}\right) \\ \mu\left(\dfrac{\partial u}{\partial Z} + \dfrac{\partial w}{\partial X}\right) \end{bmatrix} \cdot \mathbf{n} \tag{3.30}$$

$$\beta_x = X\,/\,X_0^z\left(X < X_0^z\right) + \left(X \geq X_0^z\right)\left(X \leq X_1^z\right) + \left(X > X_1^z\right)\left(X_2^z - X\right)/\left(X_2^z - X_1^z\right) \tag{3.31}$$

$$dy_\perp = y_\mathrm{m}\beta_y \tag{3.32}$$

$$y_\mathrm{m} = \iint F_Y \, dt dt \,/\, M \tag{3.33}$$

$$F_Y = \int_{S(t)} \Sigma_Y dS \tag{3.34}$$

$$\Sigma_Y = \begin{bmatrix} \mu\left(\dfrac{\partial u}{\partial Y} + \dfrac{\partial v}{\partial X}\right) \\ \left(2\mu\dfrac{\partial v}{\partial Y} - P\right) \\ \mu\left(\dfrac{\partial v}{\partial Z} + \dfrac{\partial w}{\partial Y}\right) \end{bmatrix} \cdot \mathbf{n} \tag{3.35}$$

$$\beta_y = Y\,/\,Y_0^z\left(Y < Y_0^z\right) + \left(Y \geq Y_0^z\right)\left(Y \leq Y_1^z\right) + \left(Y > Y_1^z\right)\left(H - Y\right)/\left(H_2^z - Y_1^z\right) \tag{3.36}$$

$$M = \rho\vartheta \tag{3.37}$$

Equations (3.27) – (3.37) are mathematical representations of the translational deformations of the mesh around the unconstrained swimmer. If swimmer is assumed to

be neutrally buoyant than mass, M, can be found by (3.37) [5], where ϑ denotes the total volume of the swimmer, i.e. volume of the head plus volume of tail. After determining the mass, it is possible to find the acceleration and displacement data of the swimmer, on X and Y-axes from equations (3.28) – (3.30) and (3.33) – (3.35), i.e. X and Y-forces are calculated from the total stress tensor [68], where $\mathbf{n}$ is the surface normal vector. H is the height of the domain in which the swimmer is placed. $X_0^z, X_1^z, X_2^z, Y_0^z, Y_1^z$ are deformation limit coordinates employed in order to specify where to start and where to stop the deformation in mesh function β. 'β' functions are generally responsible from determination of expanding and compressing portions of the mesh domain, namely rubber mesh behavior.

3.3.1.2 Rotation

Rotation can be described as the rigid body rotation of the swimmer with respect to its own center of mass. The rotational components of the motion of swimmer are found in a similar manner (3.38) – (3.45) as:

$$dx_\theta = \theta_x \beta_x \tag{3.38}$$

$$\theta_x = (X - X_{com})\cos(\theta) - (Y - Y_{com})\sin(\theta) + X_{com} - X \tag{3.39}$$

$$dy_\theta = \theta_y \beta_y \tag{3.40}$$

$$\theta_y = (X - X_{com})\sin(\theta) - (Y - Y_{com})\cos(\theta) + Y_{com} - Y \tag{3.41}$$

$$\theta = \iint T dt dt / J \tag{3.42}$$

$$T = \int\limits_{S(t)} \left(\Sigma_X \phi_x + \Sigma_Y \phi_y\right) dS \tag{3.43}$$

$$\phi_x = \left(Y_{com}^2 + X_{com}^2\right)^{0.5} \cos\left(\arctan\left((Y - Y_{com})/(X - X_{com})\right) + \theta_{t-dt}\right) \tag{3.44}$$

$$\phi_y = \left(Y_{com}^2 + X_{com}^2\right)^{0.5} \sin\left(\arctan\left((Y - Y_{com})/(X - X_{com})\right) + \theta_{t-dt}\right) \tag{3.45}$$

Rotation of the swimmer body with respect to its center of mass is denoted by θ and coordinates of center of the mass is given by $\left(X_{com}, Y_{com}\right)$ where the subscript '*com*' stands for the center of mass to the swimmer which is assumed to be where tail

33

and head piece is connected to each other. θ is updated via, T and J which is the mass moment of inertia of the swimmer. Torque is calculated on the swimmer surface (3.43), i.e. integration of torque values of each single point over total swimmer surface, $S(t)$, employing the current θ data, i.e. θ_{t-dt}, before the new time step is being commenced. Equations (3.28), (3.33) and (3.43) are solved with the help of numerical ordinary differential equation solver embedded in COMSOL® [85].

3.3.1.3 Waving Action

Final motion to model is the wave propagation on tail. Waving action is similar to the 3D pump model with minor changes, e.g. most importantly shape function is replaced with an exponential expression similar to hyperbolic tangent. Hence one end is still free and the other end is fixed at the head piece of the swimmer and a limiting term has been added to the equation. Equations for the waving tail portion to the swimmer are given as:

$$dy_w = Y_w \beta_w \tag{3.46}$$

$$Y_w = B(X_f, t)\sin(\omega t - kX_f)(X_f - X_{com}/\ell_f \geq 0)(X_f - X_{com}/\ell_f \leq 1) \tag{3.47}$$

$$B(X_f, t) = B_0 \left(1 - e^{-C_{sh}(X_f - X_{com})}\right)\Re \tag{3.48}$$

$$\beta_w = \begin{pmatrix} (Y - Y_0^z)/(Y_{com} - Y_0^z)(Y < Y_{com})(Y \geq Y_0^z) + \\ (Y_1^z - Y)/(Y_1^z - Y_{com})(Y \geq Y_{com})(Y \leq Y_1^z) \end{pmatrix}$$
$$\begin{pmatrix} (X \geq X_{com})(X \leq X_{com} + \ell_f) + \\ (X_1^z - X)/(X_1^z - X_{com} - \ell_f)(X > X_{com} + \ell_f)(X \leq X_1^z) \end{pmatrix} \tag{3.49}$$
$$(Z < Z_0^z)$$

where C_{sh} is the shape function constant and the last term, i.e. $(Z < Z_0^z)$, guarantees that waving deformation dissipates before it can reach lateral boundary of the channel shaped control volume occupied by fluid, i.e. $\Omega(t)$. Note that waving action is limited

with the tail length on *X*-axis and amplitude diminishes long before it reaches to the outer surfaces.

3.3.2 Navier-Stokes Boundary Conditions on Moving Boundaries

Designating the Navier-Stokes boundary conditions is easy once ALE expressions are cleared for velocities are basically total time derivatives of the given expressions (3.25) and (3.26) which is feasible because spatial limitations are clearly defined for each component of *X* and *Y*-deformations and each deformation has been formulated in terms of reference frame coordinates hence for instance there won't be a waving action on the headpiece. Thus, velocities on swimmer surfaces are defined by the following equation (3.50) based on (3.25) and (3.26) as:

$$
\begin{bmatrix} u^{3D-s} \\ v^{3D-s} \\ w^{3D-s} \end{bmatrix} = \begin{bmatrix} \dfrac{d}{dt} dx_S \Big|_{S(t)} \\ \dfrac{d}{dt} dy_S \Big|_{S(t)} \\ 0 \end{bmatrix} \tag{3.50}
$$

3.4 Setting up the Numerical Scenario

Following the moving boundary interpretation discussion, in this section the overall numerical setup is explained. Again, there is pump – swimmer and 2D – 3D partition within the context. Boundary conditions and initial conditions for all designs will be explained in detail in the light of previous sections. The scenarios explained here were given to the software environment by a graphical user interface (GUI) of COMSOL®[85].

3.4.1 Pump Simulations

In this section, initial and boundary conditions for 2D and 3D pump models are discussed in detail with diagrams. Instead of long versions of the expressions derived so far, their representative symbols are used where they fit. On the other hand, the last part

of this section contains extra derivations to be used during analysis of the numerical results. Additionally, towards the end of each section, mesh details will be given for specific designs.

3.4.1.1 2D Pump Model

This section is devoted to articulate the numerical model for 2D pump design. Figure 3.3 illustrates the proposed pump design with a waving membrane placed concentrically within a channel formed by two plates. Position of an arbitrary location on the membrane surface is expressed by reference coordinates. Shape function boundary is also shown in the Figure 3.3. Interpretation of 2D models is such that the image shown below can be extruded for any preferred distance in Z-direction; each and every slice will be identical which is why plates and membrane is considered to be infinite in Z-axis.
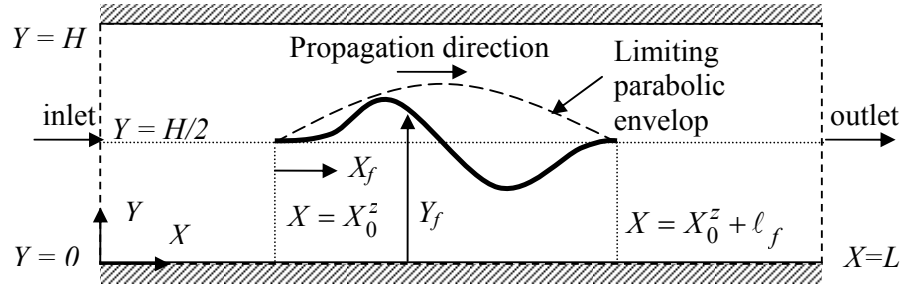
Figure 3.3: 2D pump scheme: Wave propagation on an elastic thin film placed in a microchannel filled with an incompressible fluid.

3.4.1.1.1 Spatial and Temporal Boundary Conditions

Figure 3.3 represents the 2D pump mechanism which consists of two stationary infinite plates and an inextensible membrane in-between where H is channel height and L is the channel length. The domain $\Omega(t)$ is defined with fixed boundaries, which correspond to the channel's walls, inlet and outlet, and moving boundaries that coincides with the film's surface. Boundary conditions for the Stokes equation are no-slip conditions on the plate walls as:

36

$$\begin{bmatrix} u(X,0,t) \\ v(X,0,t) \end{bmatrix} = \begin{bmatrix} u(X,H,t) \\ v(X,H,t) \end{bmatrix} = \begin{bmatrix} 0 \\ 0 \end{bmatrix} \tag{3.51}$$

Velocity on moving boundaries of the actuator film is zero in the *X*-direction since both ends are fixed. Velocity condition for moving boundary, i.e. waving infinite film can be expressed as:

$$\begin{bmatrix} u(X_f, Y_f, t) \\ v(X_f, Y_f, t) \end{bmatrix} = \begin{bmatrix} u_f^{2D-p} \\ v_f^{2D-p} \end{bmatrix} \tag{3.52}$$

At the channel inlet and outlet, unless efficiency study is carried out, the neutral flow boundary condition is used, which corresponds to vanishing total forces acting on the surface as expressed in (3.53) as:

$$\left[-P\mathbf{I} + \boldsymbol{\sigma} \right] \cdot \mathbf{n} \big|_{X=\{0,L\},Y,t} = \mathbf{0} \tag{3.53}$$

where $\mathbf{n}$ is the outward normal of the surface, and $\boldsymbol{\sigma}$ is the total stress tensor as described in previous sections. For efficiency study there need to be a pressure difference between channel inlet and outlet, i.e. pressure head. Hence (3.53) is replaced with (3.54) for those particular cases as:

$$\left[-P\mathbf{I} \right] \cdot \mathbf{n} \big|_{X=0,Y,t} = 0; \quad \left[-P\mathbf{I} \right] \cdot \mathbf{n} \big|_{X=L,Y,t} = \Delta P \equiv \left(P_{out} - P_{in} \right) \tag{3.54}$$

Note that it is possible to specify the total pressure force on inlet and outlet boundaries alternatively for all cases; however, solution may not always converge as the pressure constraint becomes too stringent on the flow for all wavelengths, amplitudes, and frequencies. Therefore, that condition is relaxed in general parametric study, with neutral boundary conditions that the flow is not restricted at the inlet and the outlet of the micropump [89], [94], [95] in terms of normal forces (3.54). Initial condition for the fluidic domain $\Omega(t)$ is the flow at rest, i.e. the velocity components and the pressure are all equal to zero at $t = 0$ as demonstrated:

$$u(X,Y,0)=v(X,Y,0)=P(X,Y,0)=0 \tag{3.55}$$

$$u_{\mathrm{m}}(X,Y,0)=v_{\mathrm{m}}(X,Y,0)=0 \tag{3.56}$$

Apparent velocity of the mesh, $\mathbf{u}_{\mathrm{m}}$ in Stokes equations, needs to be calculated due to the propagation of the motion of the boundary into the fluid domain $\Omega(t)$ as explained. The arbitrary Lagrangian Eulerian (ALE) method that incorporates Winslow smoothing is used with the following boundary conditions.

$$\begin{bmatrix} u_{\mathrm{m}}\left(X_f,Y_f,t\right) \\ v_{\mathrm{m}}\left(X_f,Y_f,t\right) \end{bmatrix}=\begin{bmatrix} u_{\mathrm{m}}^{2D-p} \\ v_{\mathrm{m}}^{2D-p} \end{bmatrix} \tag{3.57}$$

$$\begin{bmatrix} u_{\mathrm{m}}(0,Y,t) \\ v_{\mathrm{m}}(0,Y,t) \end{bmatrix}=\begin{bmatrix} u_{\mathrm{m}}(L,Y,t) \\ v_{\mathrm{m}}(L,Y,t) \end{bmatrix}=\begin{bmatrix} u_{\mathrm{m}}(X,0,t) \\ v_{\mathrm{m}}(X,0,t) \end{bmatrix}=\begin{bmatrix} u_{\mathrm{m}}(X,H,t) \\ v_{\mathrm{m}}(X,H,t) \end{bmatrix}=\begin{bmatrix} 0 \\ 0 \end{bmatrix} \tag{3.58}$$

Meshing the waving action is an important concept since sufficient data can be obtained if there are at least 5 mesh nodes per half a wave on the waving boundary. This model was meshed via triangular elements such that there are total of 2144 mesh nodes resulting in 37596 degrees of freedom, i.e. equations to solve at each time step with 10^{-8} absolute tolerance under COMSOL® with Stokes Flow and Moving Mesh modules coupled together [85]. Simulations employed UMFPACK [97] solver method. A typical simulation takes about 6 hours on a single processor of a dual 2.4 GHz 32-bit Xenon workstation with 1GB of RAM running on SUSE Linux 10.0 operating system.

3.4.1.1.2 Post-Processing for 2D Pump Simulations

Since numerical study for the proposed 2D pump design was carried out under non-dimensional quantities, i.e. $\mu = 1/Re$ and $\rho = 1$ as discussed in the introduction, hence some ground rules, namely dimensionalization tables must be provided before any attempts are placed explain the results. Table 3.1 and Table 3.2 represents these rules for this particular parametric simulation family where '*' denotes dimensionless quantities and subscript '0' stands for characteristic scale [89].

Table 3.1: Characteristic scales and their base values used in simulations and comparison of results for 2D pump analysis

Characteristic scales	Representative values
Length, ℓ_0	2.5×10^{-4} [m]
Velocity, U_0	5×10^{-4} [m/s]
Time, t_0	0.5 [s]
Pressure and shear, P_0	ρU_0^2, 2.5×10^{-4} [Pa] for water
Power, Π_0	$\rho \ell_0^2 U_0^3$, 7.81×10^{-15} [W] for water

Table 3.2: Default values for geometric variables used in simulations for 2D pump analysis, unless otherwise noted.

Geometric variables (dimensionless)	Value
Channel height, H^*	2.5
Channel length, L^*	9.0
Film's length, ℓ_f^*	5.0
Maximum amplitude of the deformation for general case, B_o^*	0.0581
Wavelength, λ^*	5.0
Frequency, f^*	1.0
Wave speed, $u^* = c^*$	5.0

The instantaneous flow rate per unit depth delivered by the pump for a given set of inputs, i.e. the set of parameterized constants $\{B_o, f, \lambda, H\}$, is computed by the integration of the X-component of the velocity over the inlet or outlet of the channel as given by (3.59):

$$Q(t) = Q_{\{in,out\}}(t) = \int_{Y=-H}^{H} \mathbf{U}(t) \cdot \left(\mp \mathbf{n}_{\{in,out\}} \right) dY \tag{3.59}$$

where $\mathbf{n}_{in}$ and $\mathbf{n}_{out}$ correspond to inlet and outlet surface normals, pointing outward direction, due to which the '+' sign applies for the outlet flow, and '−' for the inlet flow. In practice, we also check the conservation of mass by comparing inlet and outlet flow rates, the relative difference of which always remains well below the tolerance of the numerical procedure, i.e. $2|Q_{in} - Q_{out}|/|Q_{in} + Q_{out}| \approx 10^{-8} < 10^{-3}$.

The time-averaged flow rate is computed from the integral of instantaneous flow rate given by (3.59) over at least 3 full periods of plane-wave deformations after a steady-periodic state is observed as expressed in (3.60):

$$\bar{Q}_{\{in,out\}} = Q_{av} = \frac{1}{3/f} \int_{t_0}^{t=3/f+t_0} Q_{\{in,out\}}(t)\,dt \tag{3.60}$$

Due to relatively short length of the channel and the dominance of viscous effects the flow becomes steady-periodic within the first period following the initial ramp of plane-wave deformations.

The rate of work done on the fluid by the deforming motion of the film is calculated by the area integral of the product of the film's y-velocity and the y-component of the total stress tensor on the film as shown in (3.61):

$$\Pi(t) = \int_{S(t)} \Sigma_Y\left(X_f, Y_f, t\right) v\left(X_f, Y_f, t\right) dS \tag{3.61}$$

where Π is the rate of work (power) done on the fluid, also called "shaft power" in classical texts such as in Munson *et al.* (2006), Σ_Y is the Y-component of the stress tensor in 2D [67], [68], which is exerted by the structure on the fluid, and v is the Y-velocity of the film surface as in:

$$\Sigma_Y\left(X_f, Y_f, t\right) = \left(2\mu \frac{\partial v}{\partial Y} - P\right) n_Y + \mu\left(\frac{\partial u}{\partial Y} + \frac{\partial v}{\partial X}\right) n_X \tag{3.62}$$

where, μ is the viscosity of the fluid, n_X and n_Y are X and Y-components of the surface normal vector **n**. The time-averaged power is calculated the same way as the time-averaged flow rate, which is calculated by (3.60).

Hydraulic efficiency of the pump, η (3.63), based on the imposed pressure load at the exit, ΔP, time-averaged flow rate given by (3.60), and time-averaged power based on (3.61) are defined as proposed in [5]:

$$\eta = 100 \frac{\Delta P \, Q_{av}}{\Pi_{av}} \tag{3.63}$$

The hydraulic efficiency given by (3.63), in effect, is the net portion of the rate of mechanical work done on the fluid and converted to flow against the pressure load imposed at the exit and zero inlet pressure.

3.4.1.2 3D Pump Model

3D pump design is very similar to the 2D design, but it can not be sliced into identical pieces since width of the waving membrane is not equal to the width of the channel which introduces an extra design parameter, i.e. the ratio between film width and channel width, W_f/W_{ch}, instead of channel height, H, and wavelength, λ. Figure 3.4 illustrates the top view of the channel structure where in fact the pump is divided into two parts along its lateral axis in order to reduce computational power during simulations since the flow inside the channel is known to be symmetric [95]. Figure 3.5 is the three dimensional view of the 'half channel'.
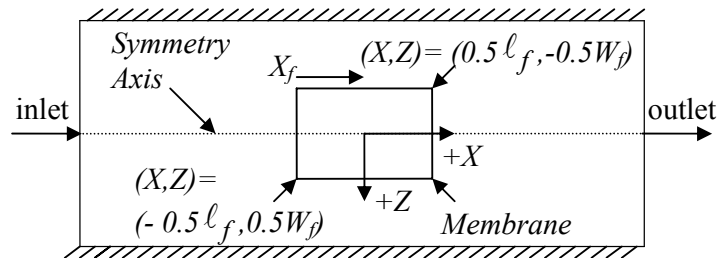

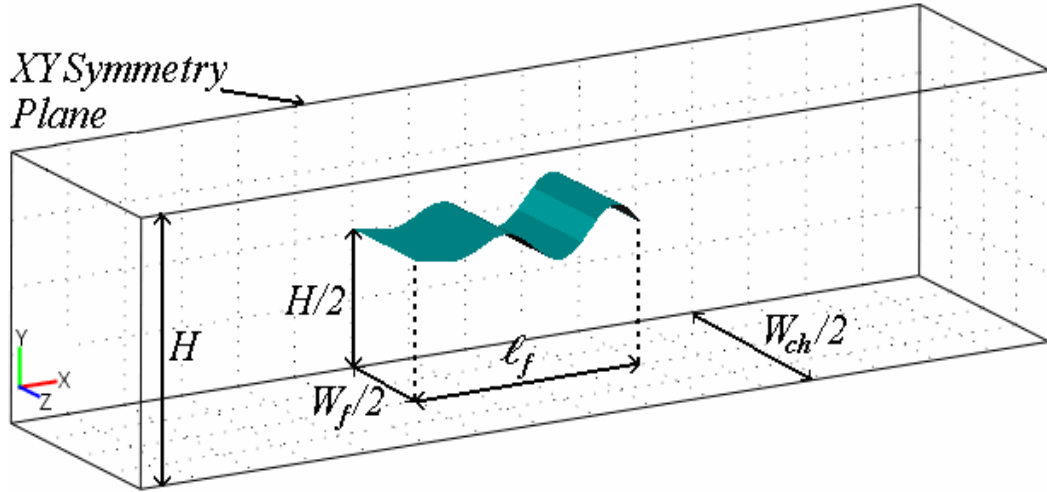Figure 3.4: 3D Pump top-view in the *Y*-direction on the *XZ* plane

Figure 3.5: 3D Pump, plane-wave deformations traveling in the Z-direction on the thin membrane placed in a channel.

3.4.1.2.1 Spatial and Temporal Boundary Conditions

Time dependent deforming domain, $\Omega(t)$, is designated as the volume occupied by the fluid inside the channel and $\mathbf{u}_m$ is the mesh deformation velocity of the domain $\Omega(t)$ [88], which is induced due to moving boundaries of the membrane. Channel walls are subjected to no-slip boundary conditions, i.e. fluid molecules on the wall surfaces do not move with the flow inside as:

$$\begin{bmatrix} u(X,0,Z,t) \\ v(X,0,Z,t) \\ w(X,0,Z,t) \end{bmatrix} = \begin{bmatrix} u(X,H,Z,t) \\ v(X,H,Z,t) \\ w(X,H,Z,t) \end{bmatrix} = \begin{bmatrix} u(X,Y,0,t) \\ v(X,Y,0,t) \\ w(X,Y,0,t) \end{bmatrix} = \begin{bmatrix} u(X,Y,W_{ch},t) \\ v(X,Y,W_{ch},t) \\ w(X,Y,W_{ch},t) \end{bmatrix} = \begin{bmatrix} 0 \\ 0 \\ 0 \end{bmatrix} \quad (3.64)$$

where H is the channel height and W_{ch} is the channel width. Similarly to the 2D pump model, thin-membrane moves in the Y-direction only leading to zero tangential components of the velocity on the membrane, both reference frame and ALE frame wise. Boundary conditions for outer extremities are also designated such that deformations do not occur but only on XY-symmetry plane where waving action takes place.

$$
\begin{bmatrix} u_m(X,0,Z,t) \\ v_m(X,0,Z,t) \\ w_m(X,0,Z,t) \end{bmatrix} = \begin{bmatrix} u_m(X,H,Z,t) \\ v_m(X,H,Z,t) \\ w_m(X,H,Z,t) \end{bmatrix} = \begin{bmatrix} 0 \\ 0 \\ 0 \end{bmatrix}
$$

$$
\begin{bmatrix} u_m(X,Y,0,t) \\ v_m(X,Y,0,t) \\ w_m(X,Y,0,t) \end{bmatrix} = \begin{bmatrix} u_m(X,Y,W_{ch},t) \\ v_m(X,Y,W_{ch},t) \\ w_m(X,Y,W_{ch},t) \end{bmatrix} = \begin{bmatrix} 0 \\ 0 \\ 0 \end{bmatrix} \tag{3.65}
$$

$$
\begin{bmatrix} u_m(X,0,Z,t) \\ v_m(X,0,Z,t) \\ w_m(X,0,Z,t) \end{bmatrix} = \begin{bmatrix} u_m(X,L,Z,t) \\ v_m(X,L,Z,t) \\ w_m(X,L,Z,t) \end{bmatrix} = \begin{bmatrix} 0 \\ 0 \\ 0 \end{bmatrix}
$$

Boundary conditions on the membrane are given by the velocity equations derived in section 3.2.2 in accordance with the no-slip boundary condition as:

$$
\begin{bmatrix} u(X_f,Y_f,t) \\ v(X_f,Y_f,t) \\ w(X_f,Y_f,t) \end{bmatrix} = \begin{bmatrix} u^{3D-p} \\ v^{3D-p} \\ w^{3D-p} \end{bmatrix} \tag{3.66}
$$

$$
\begin{bmatrix} u_m(X_f,Y_f,t) \\ v_m(X_f,Y_f,t) \\ w_m(X_f,Y_f,t) \end{bmatrix} = prescribed \tag{3.67}
$$

Mesh velocity vector, u_m, is not explicitly given as boundary condition because it is a prescribed condition [85], i.e. deformation in $\Omega(t)$ domain is modeled and expression is introduced as mesh deformation x_m (3.68) and guarantees that mesh deformation is limited within an artificial domain and diminishes before reaching channel surfaces as:

$$
\mathbf{x}_m = \begin{bmatrix} 0 \\ \begin{cases} 0, & X > \left| 0.5\ell_f \right| \\ 4Y_f\left(\dfrac{1}{4} - \left(\dfrac{Y}{H} \right)^2 \right), & \text{otherwise} \end{cases} \\ 0 \end{bmatrix} \tag{3.68}
$$

43

Inlet and outlet pressures are specified as zero in all simulations (3.69) and (3.70) but for the ones used to obtain the flow rate as a function of the pressure head for a typical pump as:

$$\left[-P\mathbf{I}\right]\cdot\mathbf{n}\big|_{X=0,Y,Z,t} = P_{in} = 0 \tag{3.69}$$

$$\left[-P\mathbf{I}\right]\cdot\mathbf{n}\big|_{X=L,Y,Z,t} = P_{out} = 0 \tag{3.70}$$

$$\left[-P\mathbf{I}\right]\cdot\mathbf{n}\big|_{X=0,Y,Z,t} = 0; \quad \left[-P\mathbf{I}\right]\cdot\mathbf{n}\big|_{X=L,Y,Z,t} = \Delta P \equiv \left(P_{out} - P_{in}\right) \tag{3.71}$$

For the flow at rest, all velocity components for material flow and mesh velocity with mesh deformation are specified as initially zero as:

$$u(X,Y,Z,0) = v(X,Y,Z,0) = w(X,Y,Z,0) = 0 \tag{3.72}$$

$$u_{\mathrm{m}}(X,Y,Z,0) = v_{\mathrm{m}}(X,Y,Z,0) = w_{\mathrm{m}}(X,Y,Z,0) = 0 \tag{3.73}$$

$$x(X,Y,Z,0) = y(X,Y,Z,0) = z(X,Y,Z,0) = 0 \tag{3.74}$$

Finally, the boundary condition for symmetry plane is set as slip/symmetry [85], i.e. normal velocity component (3.75) and tangential stress (3.76) component becomes zero as:

$$\mathbf{n}\cdot\mathbf{U} = 0 \tag{3.75}$$

$$\left[-P\mathbf{I} + \boldsymbol{\sigma}\right]\cdot\mathbf{t}\big|_{X,Y,Z=0.5W_{ch},t} = \mathbf{0} \tag{3.76}$$

where **t** is the surface tangent vector designated for *XY* symmetry plane. Similarly, mesh is created such that at least 5 mesh nodes exist per half a wave on the waving boundary. 3D pump model was meshed by triangular elements such that there are 4980 mesh nodes resulting in 222249 degrees of freedom, i.e. equations to solve at each time step, with 10^{-5} absolute tolerance under COMSOL® with Incompressible Navier-Stokes and Moving Mesh modules coupled together [85]. PARDISO solver [98] was used as numerical solution method and simulations were carried out on a double 2.73 GHz 64-Bit Xenon workstation with 16 Giga-bytes of RAM operating on Suse Linux 10.0

incorporating with Intel® Math Kernel Library, namely MKL Blas [99], and each simulation took about 1 day to complete.

3.4.1.2.2 Post-Processing for 3D Pump Simulations

Similar to the 2D case, numerical studies for 3D pump design are carried out employing non-dimensional quantities, i.e. $\mu = 1/\text{Re}$ and $\rho = 1$ as discussed in introduction. Therefore dimensionalization tables must be provided to be able to transform numerical data in to meaningful results. Table 3.3 and Table 3.4 represent the transformation for this particular parametric simulation family where subscript '0' stands for characteristic scale [95].

Table 3.3: Standard parameters and their units for 3D pump simulations.

Name, symbol	Values/dimensions
W_{ch}	$W_f + 10^{-4}$ [m]
Channel Height, H	10^{-4} [m]
Channel Length, L	4×10^{-4} [m]
Membrane Length, ℓ_f	10^{-4} [m]
Wavelength, λ	$0.5\,\ell_f$ [m]
Dynamic Viscosity of water, μ	1.12×10^{-3} [Pa.s]
Density of water, ρ	999 [kg/m³]

Table 3.4: Characteristic scales and their values for 3D pump simulations.

Characteristic scales	Representative values/dimensions
Length, ℓ_0	10^{-4} [m]
Time, t_0	$1/f$ [s]
Velocity, U_0	ℓ_0/t_0 [m/s]
Pressure and shear, P_0	ρU_0^2 [Pa]
Power, Π_0	$P_0 \ell_0^2 U_0$ [W]

The instantaneous flow rate is computed for a given set of inputs, i.e. the set of parameterized constants $\{B_0, f, W_f / W_{ch}\}$ for this simulation study, by integrating the *X*-velocity over the inlet, or outlet of the channel as:

$$Q(t) = \int_{Z=0}^{W_{ch}} \int_{Y=0}^{H} u(0, Y, Z, t) \mathbf{n}_{\{in, out\}} dY dZ \qquad (3.77)$$

where $\mathbf{n}_{in}$ and $\mathbf{n}_{out}$ correspond to inlet and outlet surface normal vectors, respectively. Time-averaged flow rate is computed from the integration of the instantaneous flow rate over at least two full cycles after the flow reaches the steady-periodic state as:

$$Q_{av} = \frac{f}{2} \int_{t_0}^{t_0 + 2/f} Q(t) dt \qquad (3.78)$$

The *Y*-component of the stress exerted on the fluid due to the membrane's motion on its surface is determined from the full stress tensor [68] as:

$$\Sigma_Y \left(X_f, Y_f, Z_f, t \right) = \begin{bmatrix} \mu \left(\dfrac{\partial u}{\partial Y} + \dfrac{\partial v}{\partial X} \right) \\[2mm] \left(2\mu \dfrac{\partial v}{\partial Y} - P \right) \\[2mm] \mu \left(\dfrac{\partial v}{\partial Z} + \dfrac{\partial w}{\partial Y} \right) \end{bmatrix} \cdot \mathbf{n} \qquad (3.79)$$

where $\mathbf{n}$ is the outward normal of the membrane's surface. Instantaneous rate of work done on the fluid by the deforming membrane is the surface area integration of the product of the total *Y*-stress and the *Y*-velocity on the membrane as:

$$\Pi(t) = \int_{S(t)} \Sigma_Y v_f dS \qquad (3.80)$$

Time-averaged rate of work done by the membrane is calculated from:

$$\Pi_{av} = \frac{f}{2} \int_{t_o}^{t_o+2/f} \Pi(t)\,dt \qquad\qquad (3.81)$$

where t_o stands for the time for ramp function to take the system from initial conditions to normal operating parameters. Hydraulic efficiency, η, of a typical micropump that consists of a thin-membrane, which deforms according to traveling-plane waves is calculated from the ratio of the fluid power, which is given by the product of the total pressure head and the flow rate, and the rate of work done by the membrane as follows [5]:

$$\eta = 100 \frac{\Delta P Q_{av}}{\Pi_{av}} \qquad\qquad (3.82)$$

3.4.2 3D Swimmer Simulations

Swimmer model is similar to the 3D pump design except swimmer surface is not just deforming with time, i.e. $S=S(t)$, it is also in motion with respect to the stationary common reference frame, i.e. $S=S(X,Y,Z,t)$. Figures 3.6 and 3.7 illustrate the swimmer inside a channel, from XY and ZX planes. Figure 3.8 shows a 3D picture of swimmer and the channel it is placed in, sliced in half with respect to XY symmetry plane. Notice that tail is a whip like structure when compared with channel and head piece of the swimmer is bullet shaped, i.e. combination of a cylinder and half a sphere on top.
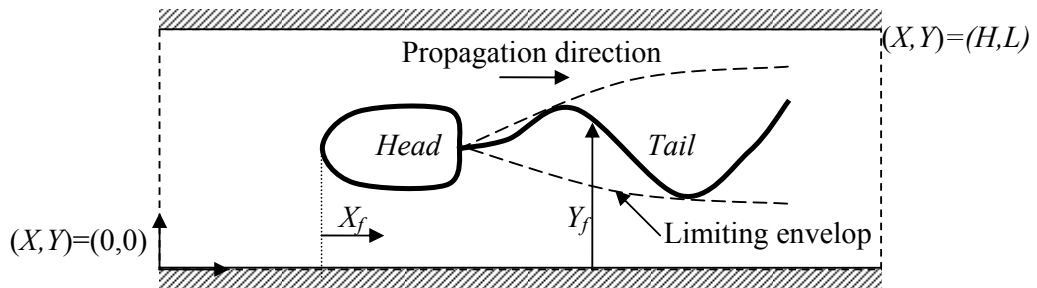

Figure 3.6: Swimmer and channel, conceptual design, snapshot from XY symmetry plane.
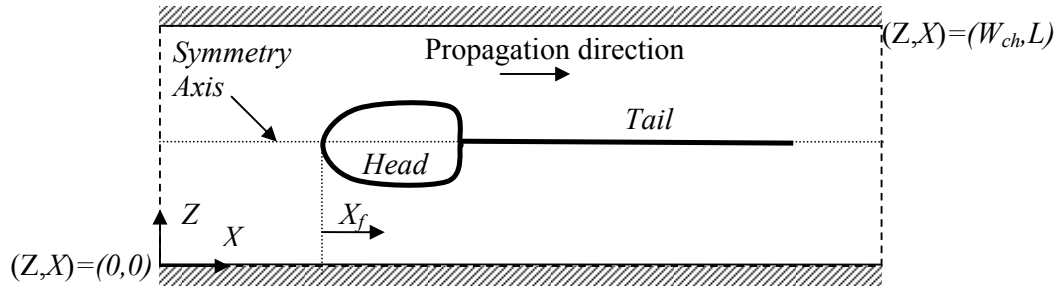
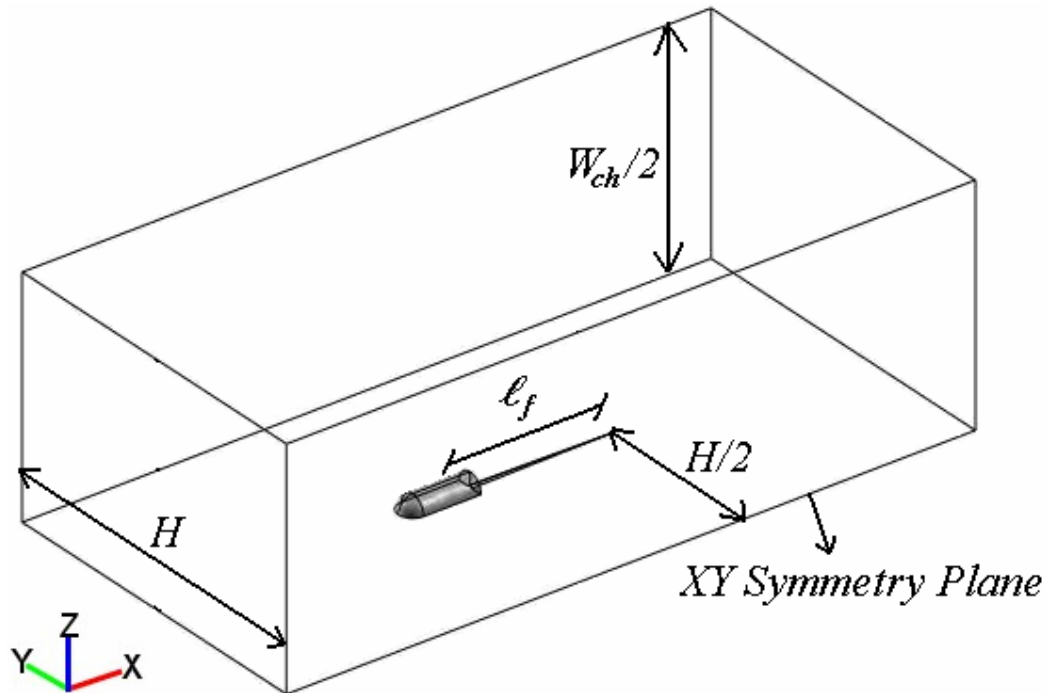Figure 3.7: Swimmer and channel, conceptual design, top view (*ZX* plane).

Figure 3.8: Swimmer and channel; split in to two symmetric parts with respect to *XY* symmetry plane.

3.4.2.1 3D Spatial and Temporal Boundary Conditions

Once more, time dependent deforming domain, $\Omega(t)$, is refers to the volume occupied by the fluid inside the channel and $\mathbf{u}_m$ is the mesh deformation velocity of the domain $\Omega(t)$ [88], which is induced due to moving boundaries of the swimmer. Channel walls are subjected to no-slip boundary conditions, i.e. fluid molecules on the wall surfaces do not move with the flow inside (3.83). Also swimmer surface is designated as

no-slip (3.84) that is to say the fluid molecules on swimmer surface are moving with the swimmer as in:

$$\begin{bmatrix} u(X,0,Z,t) \\ v(X,0,Z,t) \\ w(X,0,Z,t) \end{bmatrix} = \begin{bmatrix} u(X,H,Z,t) \\ v(X,H,Z,t) \\ w(X,H,Z,t) \end{bmatrix} = \begin{bmatrix} u(X,Y,0,t) \\ v(X,Y,0,t) \\ w(X,Y,0,t) \end{bmatrix} = \begin{bmatrix} u(X,Y,W_{ch},t) \\ v(X,Y,W_{ch},t) \\ w(X,Y,W_{ch},t) \end{bmatrix} = \begin{bmatrix} 0 \\ 0 \\ 0 \end{bmatrix} \tag{3.83}$$

$$\begin{bmatrix} u\left(X_f,Y_f,Z_f,t\right) \\ v\left(X_f,Y_f,Z_f,t\right) \\ w\left(X_f,Y_f,Z_f,t\right) \end{bmatrix} = \begin{bmatrix} u^{3D-s} \\ v^{3D-s} \\ w^{3D-s} \end{bmatrix} \tag{3.84}$$

Neutral flow boundary conditions have been assigned to channel inlet and outlets as:

$$\left[-P\mathbf{I}+\boldsymbol{\sigma}\right]\cdot\mathbf{n}\big|_{X=\{0,L\},Y,t} = \mathbf{0} \tag{3.85}$$

and initial *XY* symmetry plane boundary condition is designated as slip/symmetry to ensure the flow symmetry on *Z*-axis:

$$\mathbf{n}\cdot\mathbf{U} = 0 \tag{3.86}$$

$$\left[-P\mathbf{I}+\boldsymbol{\sigma}\right]\cdot\mathbf{t}\big|_{X,Y,Z=0.5W_{ch},t} = \mathbf{0} \tag{3.87}$$

Mesh deformation, i.e. $\mathbf{x}_m$, in domain $\Omega(t)$ is set as prescribed deformation which is expressed through (3.25) - (3.49). Deformation vector is given as:

$$\mathbf{x}_m = \begin{bmatrix} dx_S \\ dy_S \\ 0 \end{bmatrix} \tag{3.88}$$

where deformations are numerically computed and updated by solving ordinary differential equations (3.28), (3.33) and (3.42) for each time step based on dynamic

forces on swimmer body during simulation. Initial conditions for flow inside the channel, swimmer velocity and mesh deformation are set to zero as expected as:

$$u(X,Y,Z,0) = v(X,Y,Z,0) = w(X,Y,Z,0) = 0 \tag{3.89}$$

$$u\left(X_f, Y_f, Z_f, 0\right) = v\left(X_f, Y_f, Z_f, 0\right) = w(X_f, Y_f, Z_f, 0) = 0 \tag{3.90}$$

$$u_{\mathrm{m}}(X,Y,Z,0) = v_{\mathrm{m}}(X,Y,Z,0) = w_{\mathrm{m}}(X,Y,Z,0) = 0 \tag{3.91}$$

$$x(X,Y,Z,0) = y(X,Y,Z,0) = z(X,Y,Z,0) = 0 \tag{3.92}$$

Similarly, mesh is carried out in the same way to get at least 5 mesh nodes per half a wave on the waving boundary. 3D swimmer design was meshed by triangular elements with a total of 1530 mesh nodes resulting in 33495 degrees of freedom, i.e. equations to solve at each time step with 10^{-4} absolute tolerance under COMSOL® with Incompressible Navier-Stokes and Moving Mesh modules coupled together [85]. These simulations were carried out on double 2.73 GHz 64-Bit Xenon workstation with 16 Giga-bytes of RAM operating on openSuse Linux 10.2 incorporating with Intel® Math Kernel Library, i.e. namely MKL Blas [99], and each simulation took about 2 to 3 hours to complete.

3.4.2.2 Post-Processing for 3D Swimmer Simulations

The most important difference between the swimmer and pump simulations is that they are carried out in dimensional form, i.e. the numerical outputs are obtained in SI units. Table 3.5 contains all data on simulation constants including geometry and material properties.

Table 3.5: Simulation constants for 3D swimmer study

Name, symbol	Values/dimensions
W_{ch}	4×10^{-3} [m]
Channel Height, H	3×10^{-3} [m]
Channel Length, L	6×10^{-3} [m]
Tail Length, ℓ_f	1.25×10^{-3} [m]
Head Length, L_h	6.25×10^{-4} [m]
Head Radius, r_h	1.25×10^{-4} [m]
Tail (membrane) width, W_f	2×10^{-5} [m]
Swimmer Mass Moment of Inertia, J	7.073456×10^{-12} [kg.m^2]
Mass of the Swimmer, M	1.713071×10^{-8} [kg]
Dynamic Viscosity of water, μ	1.12×10^{-3} [Pa.s]
Density of water, ρ	999 [kg/m^3]

In the simulations, flow velocity inside the channel was not of concern whereas average swimmer velocity components were of interest. Hence velocity vector for the swimmer is obtained from equations (3.27), (3.32) and (3.42) derived in previous sections by integrating and averaging the numerical values over two periods as:

$$u_{av} = \frac{f}{2} \int_{t_0}^{t_0 + 2/f} u^{3D-s} dt \qquad (3.93)$$

$$v_{av} = \frac{f}{2} \int_{t_0}^{t_0 + 2/f} v^{3D-s} dt \qquad (3.94)$$

$$\varpi_{av} = \frac{f}{2} \int_{t_0}^{t_0 + 2/f} \frac{d\theta}{dt} dt \qquad (3.95)$$

where ϖ is the angular velocity of the swimmer with respect to its center of mass. The Y-component of the stress exerted on the fluid due to the waving motion on tail surface is determined from the Y-component of the full stress tensor [68] as:

$$\Sigma_Y\left(X_f, Y_f, Z_f, t\right) = \begin{bmatrix} \mu\left(\dfrac{\partial u}{\partial Y} + \dfrac{\partial v}{\partial X}\right) \\ \left(2\mu\dfrac{\partial v}{\partial Y} - P\right) \\ \mu\left(\dfrac{\partial v}{\partial Z} + \dfrac{\partial w}{\partial Y}\right) \end{bmatrix} \cdot \mathbf{n} \tag{3.96}$$

where $\mathbf{n}$ is the outward normal of the tail's surface. Instantaneous rate of work done on the fluid by the deforming tail is the surface area integration of the product of the total Y-stress and the Y-velocity on the tail. Notice that tail velocity is zero if the corresponding surface coordinates are not on the tail (3.49).

$$\Pi_w(t) = \int\limits_{S(X_f, Y_f, Z_f, t)} \Sigma_Y \left.\frac{dY_w}{dt}\right|_{S(X_f, Y_f, Z_f, t)} dS \tag{3.97}$$

Time-averaged rate of work done by the tail is calculated from integration of (3.97) over two complete periods as:

$$\left\langle \Pi_w \right\rangle = \Pi_{w-av} = \frac{f}{2} \int\limits_{t_0}^{t_0 + 2/f} \Pi_w(t)\, dt \tag{3.98}$$

where t_0 stands for the time for ramp function to take the system from initial conditions to normal operating parameters. The X-component of the stress exerted on the swimmer due to the net propulsion is determined from the X-component of the full stress tensor [68] as:

$$\Sigma_X\left(X_f, Y_f, Z_f, t\right) = \begin{bmatrix} \left(2\mu\dfrac{\partial u}{\partial X} - P\right) \\ \mu\left(\dfrac{\partial u}{\partial Y} + \dfrac{\partial v}{\partial X}\right) \\ \mu\left(\dfrac{\partial u}{\partial Z} + \dfrac{\partial w}{\partial X}\right) \end{bmatrix} \cdot \mathbf{n} \tag{3.99}$$

where **n** is the outward normal of the membrane's surface. The instantaneous power to overcome the *X*-component of the total force exerted on swimmer surface is the surface integral of the propulsion velocity (3.93) and *X*-stress (3.99) product as:

$$\Pi_X(t) = \int\limits_{S(X,Y,Z,t)} \Sigma_X u_{av}^{3D-s} dS \tag{3.100}$$

which is used to calculate the time averaged power consumption in *X*-direction.

$$\left\langle \Pi_X \right\rangle = \Pi_{X-av} = \frac{f}{2} \int\limits_{t_0}^{t_0+2/f} \Pi_X(t) dt \tag{3.101}$$

Swimmer efficiency as depicted by Sfakiotakis *et al.* (1999) known as Froude efficiency and is given by (3.102) as:

$$\eta = \frac{\left\langle \Pi_X \right\rangle}{\left\langle \Pi_w \right\rangle} \tag{3.102}$$

These final remarks on swimmer efficiency conclude most of the theoretical and numerical background on this subject from the fluidic perspective, introducing the groundwork of the theoretical and numerical studies. Some additional comments will be added into this text in the following chapter as are seem to fit.

CHAPTER 4

RESULTS

In this section, numerical results to the simulations carried out for both pump and swimmer studies are presented extensively. The most intensive study is done for 2D pump model. This model is the key element to understand how fluid in the vicinity of a waving membrane behaves and what is to expect as well as to compare and check the numerical results with the asymptotical results found by Sir Taylor (1951) and Katz (1974), later on Childress (1981). 3D pump simulations were mostly the basis to explore the 3D behavior of the flow and understand the basic capabilities about the FEA tool; what is possible and what is not. 3D swimmer simulations are carried out lastly since they demand the most insight and experience about the behavior of flow as well as the capabilities of the mesh deformation module used throughout this study. The following results represented here are either published in different papers or about to be published in time [27], [89], [94], [95], [96]. Keep in mind that each data point in the plots correspond to an individual simulation.

4.1 Pump Results

Pump simulations have been carried out for various sets of parameters. 2D pump behavior is studied for wavelength, λ, wave amplitude, B_o, channel height, H and driving frequency, f. Summing up all the mathematical background for this simulation batch, the main partial differential equation to be solved is the dimensionless incompressible isothermal Stokes with moving mesh and unsteady flow (4.1) with conservation of mass (4.2) incorporating Winslow smoothing method (4.3) as:

$$\left(\frac{\partial \mathbf{U}}{\partial t} - \mathbf{u}_\mathrm{m} \cdot \nabla \mathbf{U}\right) = -\nabla P + \frac{1}{\mathrm{Re}}\nabla^2 \mathbf{U} \tag{4.1}$$

$$\nabla \cdot \mathbf{U} = 0 \tag{4.2}$$

$$\frac{\partial^2}{\partial x^2}\mathbf{X} + \frac{\partial^2}{\partial y^2}\mathbf{X} = 0 \tag{4.3}$$

3D pump behavior is studied for wave amplitude, B_o, membrane width to channel width ratio, W_f/W_{ch} and driving frequency, f. The main partial differential equation to be solved is the dimensionless incompressible isothermal Navier-Stokes with moving mesh and unsteady flow (4.4) with conservation of mass (4.5) incorporating Winslow smoothing (4.6). The important difference in between is that the mesh deformation is a predefined quantity instead of a boundary condition.

$$\left(\frac{\partial \mathbf{U}}{\partial t} + \mathbf{u}_\mathrm{r} \cdot \nabla \mathbf{U}\right) = -\nabla P + \frac{1}{\mathrm{Re}}\nabla^2 \mathbf{U} \tag{4.4}$$

$$\nabla \cdot \mathbf{U} = 0 \tag{4.5}$$

$$\frac{\partial^2}{\partial x^2}\mathbf{X} + \frac{\partial^2}{\partial y^2}\mathbf{X} = 0 \tag{4.6}$$

4.1.1 2D Pump Results

This section has six sub-components: First of all the dimensionalization procedure is overviewed then working principles of the proposed pump system is discussed, then the effect of design parameters are studied in a dimensionless manner. After the characteristic pump curve is investigated in the fourth part, in the fifth part the parametric study is revisited for maximum dimensional quantities. Finally combined effects of the design variables for power consumption and flow rate are studied in the sixth part.

4.1.1.1 Dimensionalization Process

Dimensionalization procedure is an important element to understand the pump behavior for a specific set of design parameters since nondimensional results are the

generalized behavior of the proposed pump design in any dimensions as long as the Re criteria, i.e. Re < 1, discussed in the introduction is satisfied. Table 3.1 contains the characteristic scales for length, ℓ_0, velocity, U_0, time, t_0, pressure and shear, P_0, and power, Π_0. Basically dimensionalization procedure is relying on the product of nondimensional results with characteristic scales satisfying the Re criteria, i.e. $\ell_{\text{dim}} = \ell^* \ell_0$, $U_{\text{dim}} = u^* U_0$, $t_{\text{dim}} = t_0 / f^*$, $P_{\text{dim}} = P^* P_0$ and $\Pi_{\text{dim}} = \Pi^* \Pi_0$ where subscript 'dim' stands for dimensional quantity.

4.1.1.2 Analysis of Operating Principles

In Figure 4.1, a series of snapshots of the pressure and velocity distribution in the channel is shown for $f^* = 1.0$, $\lambda^* = \ell_f^* = 5$ and $B_o^* = 0.365$. First half of the full period between $t^* = 3.9$ and $t^* = 4.9$ is covered in the snapshots. The other half of the period is mirror-symmetric with respect to the channel centerline. At a given instant, such as any snapshot shown in Figure 4.1-(a) –(e) , higher pressure takes place on the side of the film that pushes the fluid than the side which pulls the fluid.

In other words, a particular point on the film is exposed to a higher pressure above the film than below when the slope of the film at that point is negative and lower pressure than the one below when the slope is positive as the waves travel in the X-direction. These high and low pressure couples move downstream at the same velocity as the speed of wave propagation. Once the high (low) pressure point on the film passes the midpoint, it starts decreasing its intensity; and reaches to its lowest when the film takes the shape of a 'Mexican hat' as depicted in Figure 4.1-(c) corresponds to the largest deformation of the midpoint. As the wave travels further downstream and the slope of the film changes, high and low pressure regions switch sides; high pressure takes place under the film and low pressure above the film. It is noted that Figure 4.1-(d) ($t^* = 4.3$) is the mirror image of Figures 4.1-b ($t^* = 4.0$) and 4.1-e ($t^* = 4.4$) of 4.1-a ($t^* = 3.9$).
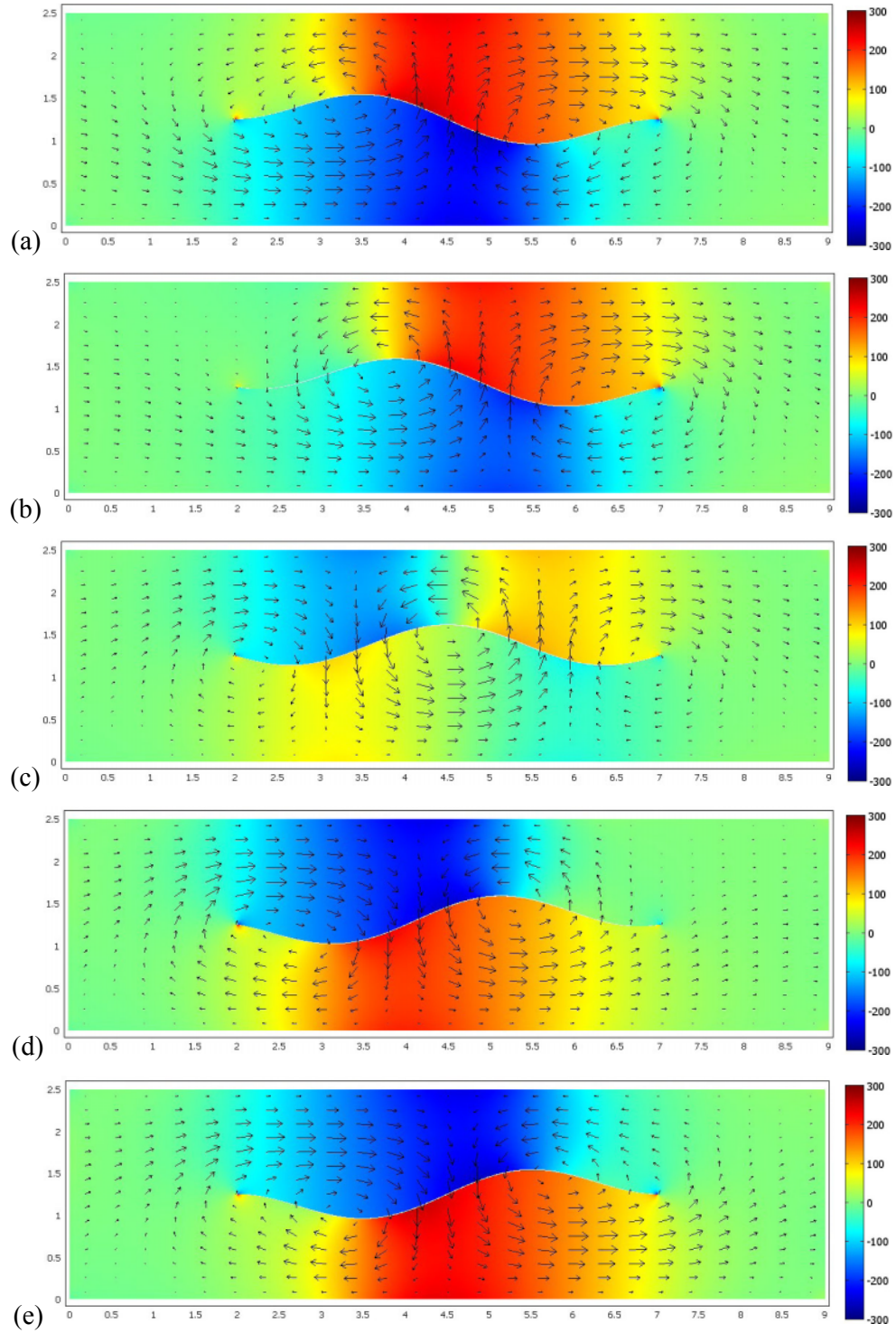
Figure 4.1: 2D Pump; H^*=2.5, $B^* = 0.365$, $\lambda^* = \ell_f^* = 5, f^* = 1$; snapshots of the pressure distribution (color shading), and flow velocity (arrows) for $t^* = 3.9, 4.0, 4.15, 4.3,$ and 4.4 respectively from (a) to (e). The length of the arrows is proportional to local magnitude of the velocity.

Furthermore, in combination with the local vertical motion of the film, net pressure difference across the film introduces a moment and is accompanied by recirculation in the fluid. As the recirculation moves downstream it results in a net flow rate in the channel albeit smaller than the local flow rate taking place above or below the film. The relative size of the velocity arrows indicate the local speed in Figures 4.1-(a) – (e). At any given instant and X-position on the film, X_f, the sum of the two flows on both sides of the film must be equal to the total flow rate:

$$Q(t) = Q_{top}\left(X_f, t\right) + Q_{down}\left(X_f, t\right) \tag{4.7}$$

$$Q_{top}\left(X_f, t\right) = \int_{Y_f}^{H} u\left(X_f, t\right) dY \tag{4.8}$$

$$Q_{down}\left(X_f, t\right) = \int_{0}^{Y_f} u\left(X_f, t\right) dY \tag{4.9}$$

Hence, for the flow rate to be positive at all times, either both Q_{up} and Q_{down} must be positive at any position on the film, or when one is negative the other must be positive and have a larger magnitude.

In Figure 4.2, total flow rate and relative variations of Q^*_{top} and Q^*_{down} for $X_f = \ell_f / 2$ are shown with respect to time. The net flow rate, $Q^*(t)$, remains always positive, but oscillates between its minimum, 0.77, and maximum values, 0.99. The partial flow rate above and below the film, is also steady-periodic but oscillates between −1.25 and 2.02 for the case shown in Figure 4.2. When the flow rate above the film reaches its maximum, the flow rate below the film becomes the minimum and vice versa.
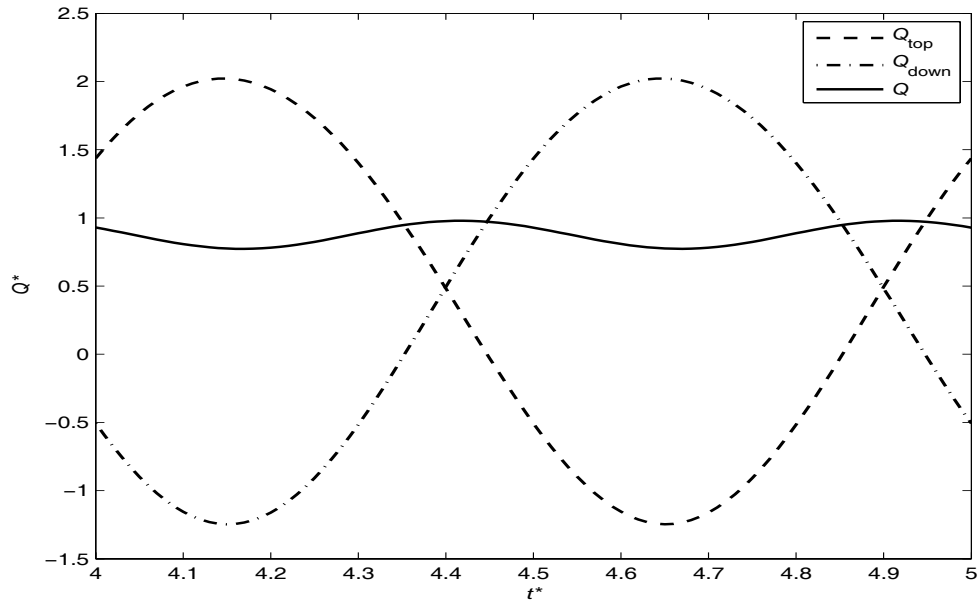
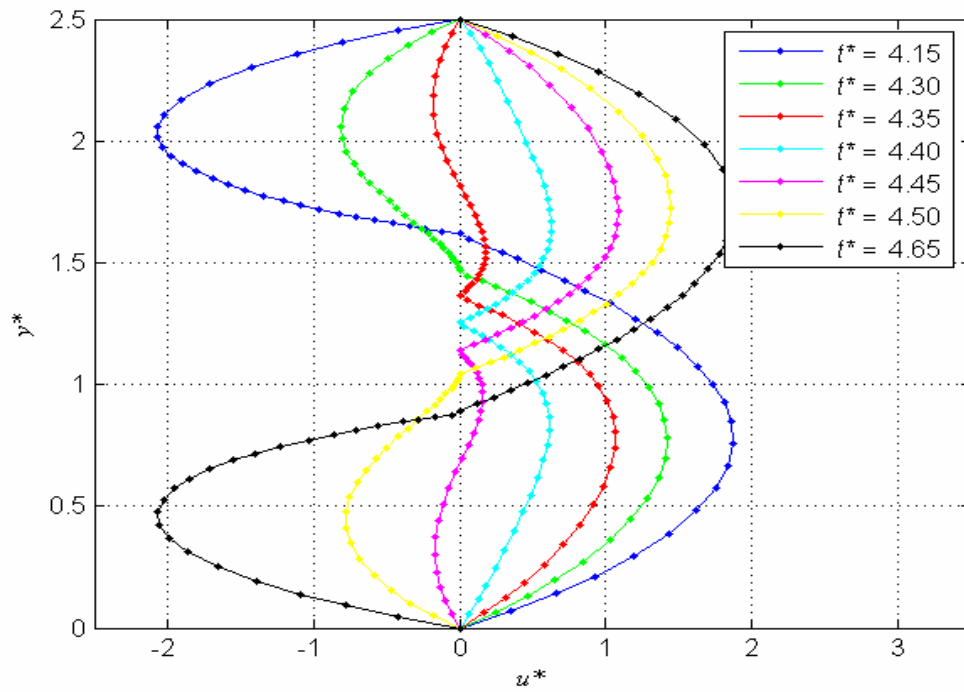Figure 4.2: 2D Pump; flow rates through top and down side of the elastic film and the net flow.

Figure 4.3: 2D Pump; flow rates through top and down side of the elastic film and the net flow.

The *Y*-profile of the *X*-component of the fluid velocity at the midpoint of the channel is shown for $t^* =$ 4.15, 4.3, 4.35, 4.4, 4.45, 4.5, and 4.65 in Figure 4.3. The *Y*-position of the film at the midpoint, $Y_f\left(\ell_f/2,t\right)$ is maximum when $t^* =$ 4.15 and minimum when $t^* =$ 4.65. At $t^* =$ 4.15, the *X*-component of the velocity is in the negative direction above the film, and in the positive direction below confirming observations in Figure. 4.2. At $t^* =$ 4.3, the flow passing the midpoint slows down in magnitude both above and below the film; this corresponds to diminishing intensity of the high and low pressures. At $t^* =$ 4.35, flow above the film changes its direction near the film; net flow rate above the film at that time is about zero as shown in Figure 4.2. At $t^* =$ 4.40, deformation of the film at the midpoint is zero and the *X*-velocity profiles above and below the film are almost identical and positive corresponding to $Q^*_{top} = Q^*_{down} = 0.494$ as in Figure 4.2. At $t^* =$ 4.45, velocity profile above (below) the film is similar to the velocity profile below (above) the film at $t^* =$ 4.35. This is also valid for $t^* =$ 4.50 and 4.30, and $t^* =$ 4.65 and 4.15. From that time onward, the evolution of the velocity profile is reversed until $t^* =$ 5.15, when the cycle is completed.

Figures 4.4-(a) and 4.4-(b) depict the pressure distribution and Figure 4.4-(c) shows the *u*–velocity and streamlines in the channel for the case which corresponds to small wavelengths compared to the length of the film. Namely, we have $\lambda^*/\ell^*_f = 1/11$, f^* = 1, and $B^*_0 = 0.058$. In this simulation, the length scale is kept the same as in Table 1, and the time scale is, $t_0 = 5.5$ s. According to Figure 4.4-(a), high and low pressure regions are distributed in the close vicinity of the film on both sides. Similar to the response shown in Figures 4.4-(a) – (e), pressure is higher when the slope of the surface is positive and lower when negative above the film. However, there are multiple pairs of high and low pressure regions on both sides of the film corresponding to a multitude of waves on the film as shown in Figure 4.4-(a). Maximum and minimum pressures are closer to deformation peaks. Multiple snapshots are omitted, as the pressure changes locally near the film only. In fact, in Figure 4.4-(b), the pressure distribution along the channel is shown at $Y^* =$ 2.0 and $t^* =$ 4.0 (see section A-A in Figure 4.4-(a)) – it is noted that, this profile remains almost steady and does not change significantly in time.
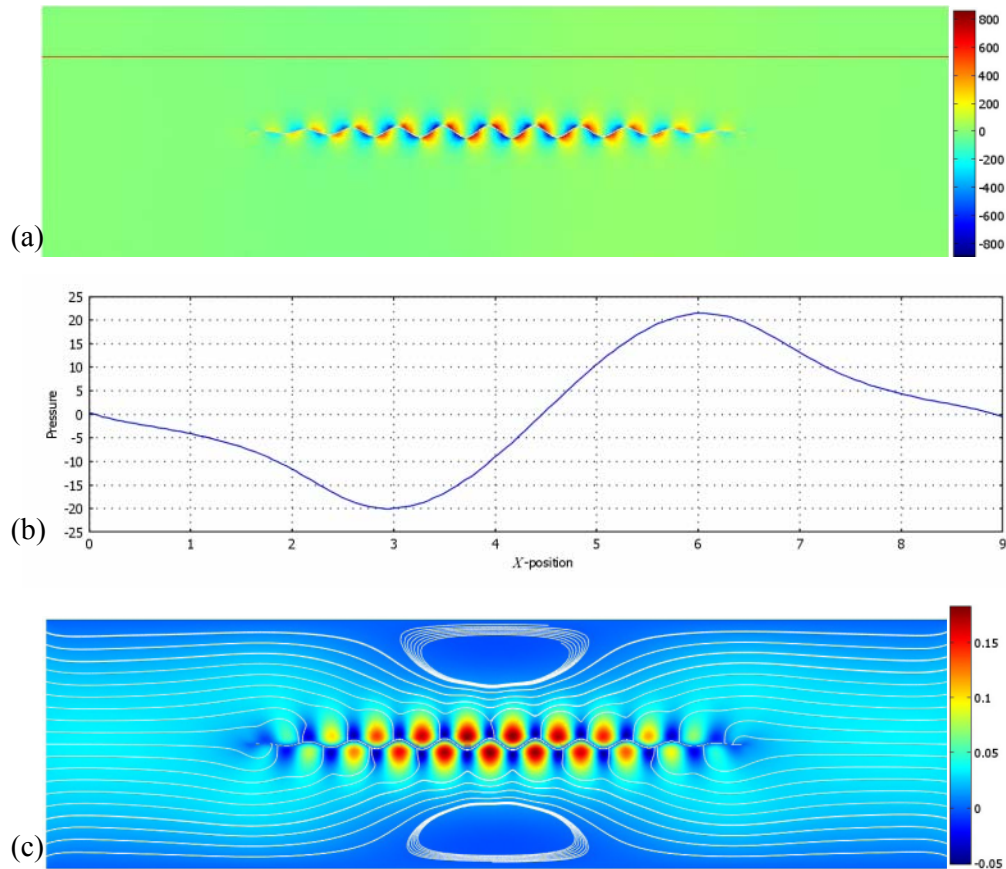
Figure 4.4: 2D Pump; for $\lambda / \ell_f = 11, f^* = 1, B_o^* = 0.058$ at $t^* = 4.0$: (a) color shaded pressure distribution; (b) pressure plot at section A-A (a); (c) color shaded X-velocity distribution and streamlines.

The pressure profile in Figure 4.4-(b) is typical for a dynamic pump placed in a channel, where the pressure first drops due to friction in the channel prior to the position where pumping takes place, increases due to pumping action, and, finally, decreases again due to friction in the exit portion. Corresponding X-velocity distribution and streamlines are shown in Figure 4.4-(c), which does not vary significantly in time near the walls confirming a steady flow in that region but varies with respect to traveling waves near the film. Inlet and exit portions of the channel correspond to almost steady-laminar parabolic profiles as indicated by color shading of the X-velocity. Moreover, there is a steady vortex pair in the middle of the channel on both sides of the film near the walls indicating that average X-velocity must be higher near the film. In essence, streamlines indicate that the time-averaged velocity distribution is similar to that of converging-diverging nozzles.

A special case of the flow regime takes place when the amplitude of the waves is comparable to the height of the channel. In the limit, when $B_o = H/2$ the pump in fact works as a displacement pump, where the deformation waves on the film carries the fluid steadily.

Another flow regime occurrence is an expected case when the wavelength is much larger than the length of the film. In this case, the net flow rate goes to zero and the effectiveness of the pump diminishes. The film simply deforms according to $\mathbf{u}_m$ with a parabolic deformation profile not yielding a significant net flow.

4.1.1.3 Parametric Study-1: Parametric Analysis of Time-Averaged Results

Figure 4.5-(a) depicts the relationship between the channel-height-to-amplitude ratio, H/B_o, and the time and area-averaged velocity, $u_{av}^* = \langle U^* \rangle = \bar{U}^* = \bar{Q}^*/H^*$, which decreases with the square of the H/B_o ratio. Katz (1974) observed that velocity normalized with the speed of wave propagation is proportional to the square of B_o/H ratio when $H/\lambda \sim O(1)$ according to:

$$\frac{\bar{U}_\infty}{c} = \frac{\Lambda_1}{\left(H/B_o\right)^2 + \Lambda_2} \tag{4.10}$$

where '∞' denotes the upstream velocity property, '$\bar{\ }$' stands for time averaged quantity as subscript 'av' or '$\langle\ \rangle$' used interchangeably so far throughout this text, c is the wave propagation speed (= λf), Λ_1 and Λ_2 are positive constants and U is the generic velocity expression which corresponds to upstream velocity without orientation. This behavior is consistent with what is reported by Katz (1974) in the analysis of the propulsion of an infinitely extending sheet placed between parallel plates and subject to traveling deformation-waves. This relationship is predominant regardless whether the amplitude or the channel height is varied in simulations. Moreover, in Figure 4.5-(a), it is shown that the average velocity converges to the displacement-pump limit, which is characterized by the amplitude of the waves being equal to the half of the channel's height. In that case, essentially, the average velocity of the flow is the same as the propagation speed of the waves.
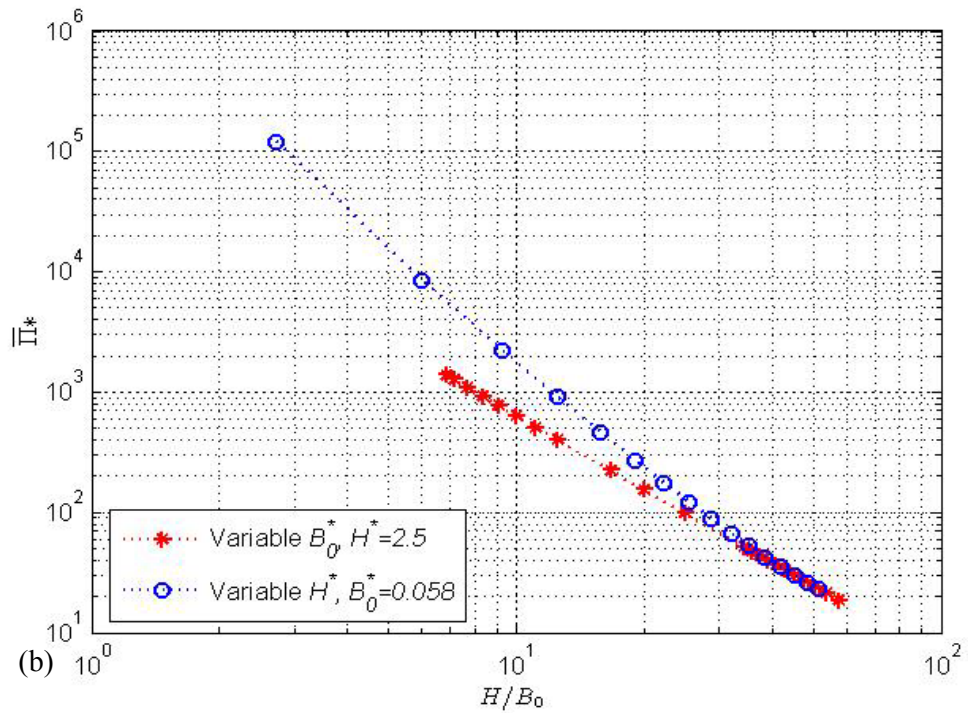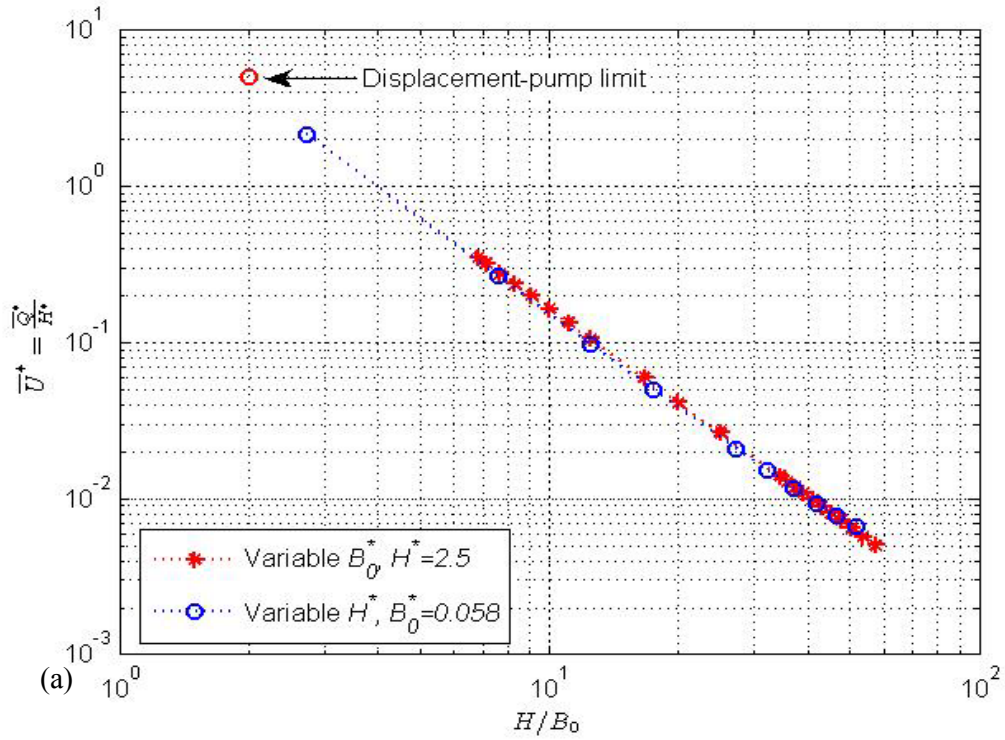
Figure 4.5: 2D Pump; (a) parametric dependence of the time and area averaged velocity with respect to channel-height to wave amplitude ratio, H/B_o (b) parametric dependence of the time-averaged power exerted on the fluid by the film with respect to H/B_o for varying H and B_o.

In Figure 4.5-(b), time-averaged nondimensional rate-of-work done on the fluid by the elastic film is plotted against the H/B_o ratio. Rate of work decreases proportional to the square of H/B_o ratio. This behavior is observed in the case for variable amplitude simulations.

In effect, this result agrees qualitatively well with the asymptotic analysis presented by Childress (1981) for the time-averaged work per unit horizontal area per time for the infinite sheet, which results in quadratic dependence of power on the amplitude as:

$$\bar{\Pi}_\infty = C 2\mu \frac{\omega^2 B_o^2}{\lambda} \tag{4.11}$$

where the proportionality constant, C is equal to one for the infinite sheet. Furthermore variable height runs deviate from the square dependence due to the relative change in other variables such as λ, which has a profound effect on the flow regime as discussed earlier and shown in Figures 4.1-(a) – (e) and Figures 4.4-(a) – (c).

In Figure 4.6-(a), the relationship between the time-averaged flow rate and the frequency of the deformation waves is shown. It is clear that the average flow rate tends to increase linearly with the frequency. This is also observed by Sir Taylor (1951) in the analysis of swimming microorganisms, which is modeled via a sheet of infinite extension that propagates deformation waves in the opposite direction to the swimming direction in an infinite medium without walls. In Taylor's (1951) analysis the average velocity of the microswimmer has a leading term proportional to the frequency of the deformations on the film as:

$$\overline{U_\infty} \approx k^2 B_o^2 c \sim \frac{B_o^2 \omega}{\lambda} \tag{4.12}$$

Based on (4.10) and (4.12) it is plausible to expect the average velocity, hence the flow rate for constant channel height, constant amplitude and constant wavelength to have a linear dependence on the frequency.
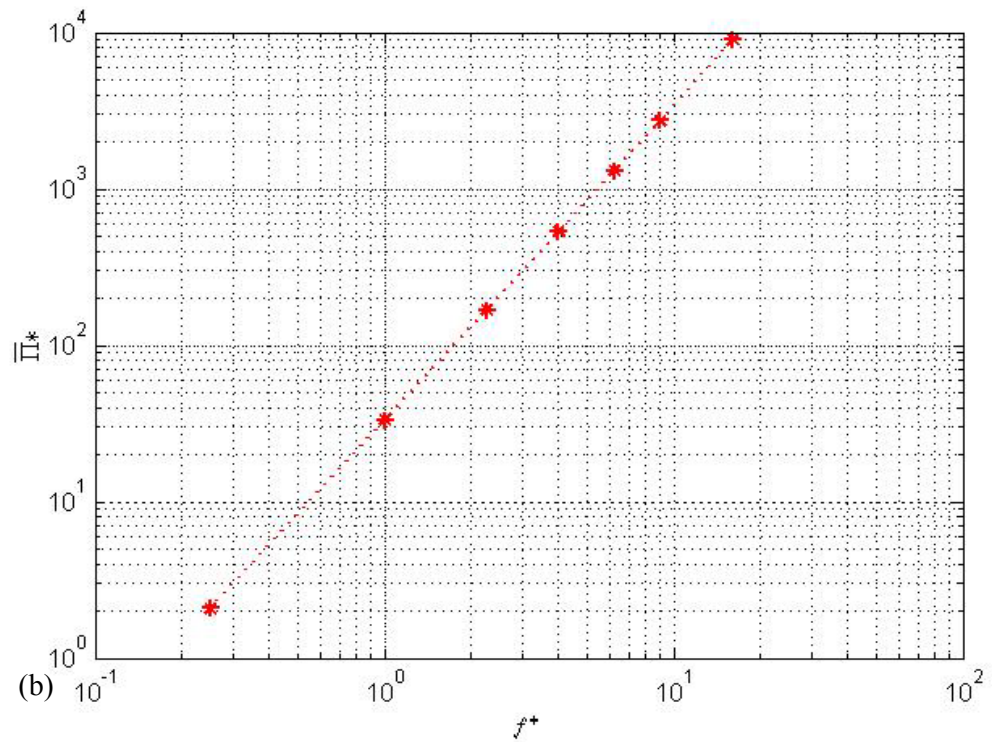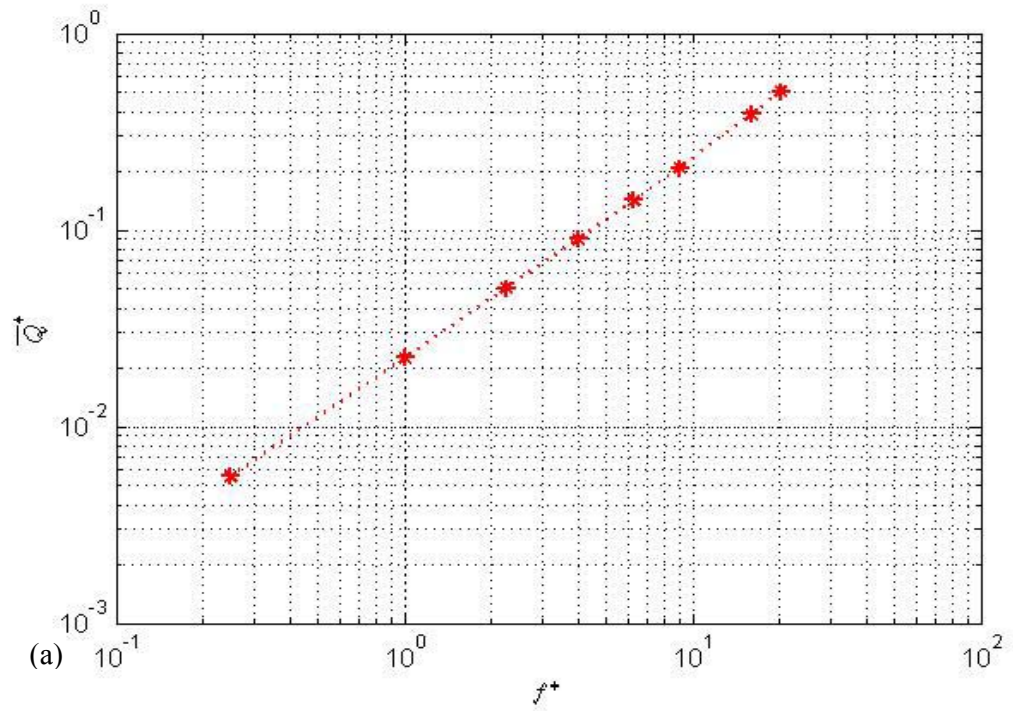
Figure 4.6: 2D Pump; (a) time-averaged flow rate as a function of the frequency of the sinusoidal deformations on the film; (b) time-averaged dimensionless power exerted on the fluid as a function of the frequency.

Figure 4.6-(b) demonstrates the behavior of time-averaged nondimensional power exerted on the fluid, which is calculated from (4.12), with respect to driving frequency. Power exerted by elastic thin film tends to increase with the square of frequency, which qualitatively agrees well with the result of the analysis presented in Childress (1981) and given by (4.11).

In Figure 4.7-(a), average flow rate is plotted against the wavelength. As reported in Figures 2 and 3, the wavelength, in fact, determines the flow regime that takes place in the channel. For small wavelengths, almost-steady flow rate in the channel decreases slowly with the wavelength agreeing well with the result given by (4.12).

As the wavelength becomes comparable with the separation of channels, which is half of the length of the film, steady-periodic flow rate increases proportional to the square root of the wavelength rather than the linear dependence suggested by (4.10).

Note that the analysis, which is the basis of the result presented in (4.10), is for an infinitely long sheet unlike the finite film considered here and for which $\lambda / H \approx O(1)$. It is presumable to suggest that the deviation is due to film's finite-length, and further studies are necessary to elucidate this behavior. Moreover, due to the finite length of the film further increase of the wavelength is expected to reduce the flow rate as the limiting envelope around the waving action reduces the effectiveness of the wave propagation.

In Figure 4.7-(b), time-averaged power is plotted as a function of the wavelength, λ. For small wavelengths, $\lambda \leq \ell_f / 2$, nondimensional power exerted on fluid by the film decreases linearly with respect to the wavelength according to (4.12). But for $\lambda \geq \ell_f / 2 = H$, a different pattern emerges and the power linearly increases with the wavelength. According to the analysis carried out by Katz (1974), when the wavelength is comparable to the separation between the channel walls, leading order of the average rate of work is given by:

$$\overline{\Pi}_{\infty,\lambda \sim H} \sim \mu c^2 k B_0^2 = \mu \omega^2 B_0^2 \lambda \tag{4.13}$$
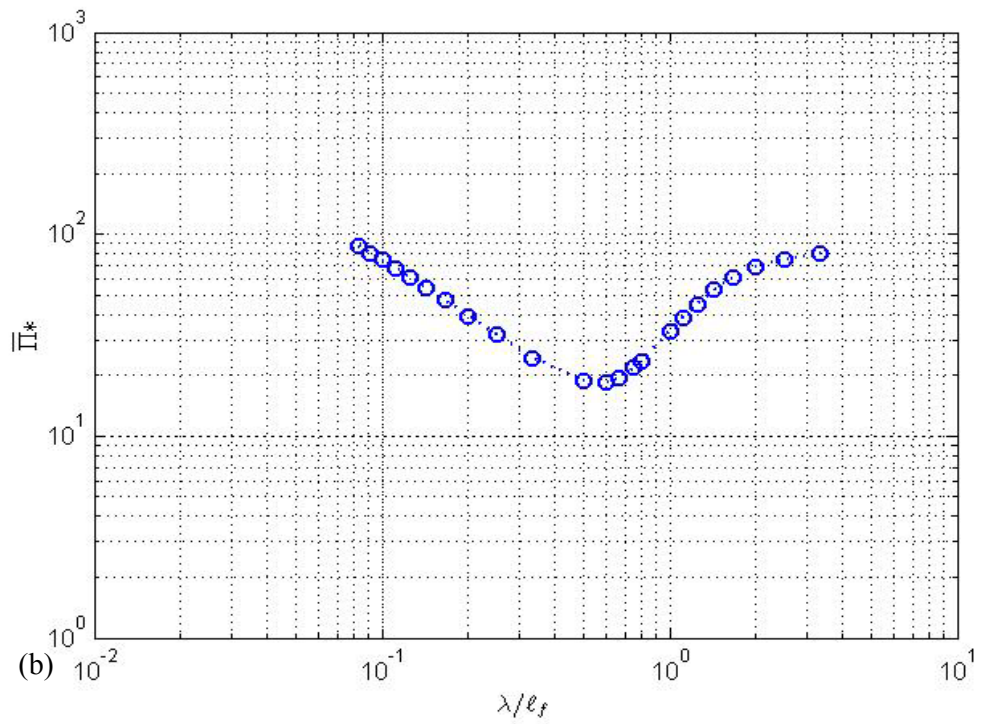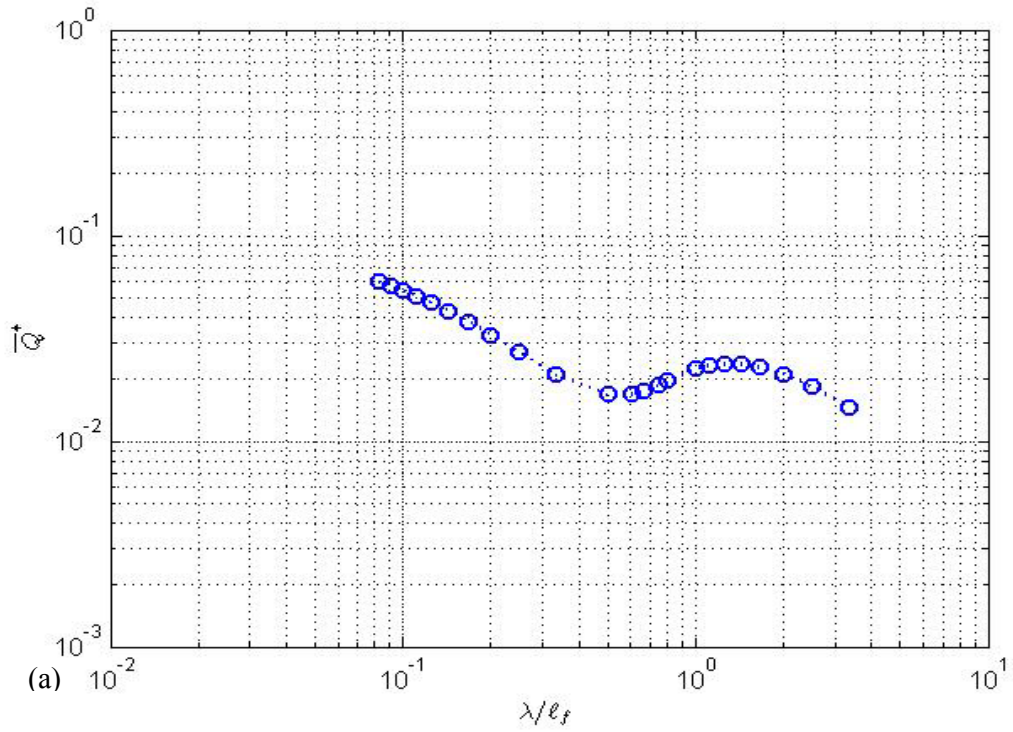
Figure 4.7: 2D Pump; (a) the time-averaged flow rate as a function of wavelength to film's length ratio; (b) time-averaged power exerted on fluid by the film as a function of wavelength to film's length ratio.

67

For that regime, the pressure itself varies proportional to the wavelength. For very large wavelengths compared to the film's length, uniform steady flow can not be maintained since the motion of the finite film turns into a simple uniform vertical motion of a parabolic curve and the propagation of waves diminishes. This behavior manifests itself as leveling off of the curve for large wavelengths in Figure 4.7-(b).

4.1.1.4 Characteristic Pump Curve

In Figure 4.8, the pressure load and the efficiency are plotted against the time-averaged flow rate for the base case, for which $\lambda = \ell_f = 1.25$ mm, $B_o = 14.5$ μm and $f = 2$ Hz. The performance is that of a typical dynamic pump without inertial effects as the pressure difference due to higher exit pressure varies linearly with the flow rate, and, hence, the efficiency of the pump is given by a perfect parabola. The maximum time-averaged flow rate is obtained for zero pressure load at $Q_{max} = 0.42$ μl/min, and the maximum pressure load for the zero time-averaged flow rate is 0.99 mPa. The pump operates at constant fluid power (rate of work done on the fluid by the film) of 2.60 pW with small variations ($<10^{-2}$ pW) as the pressure load changes. The energy of the flow is distributed between the kinetic energy of the flow and the pressure according to the pressure load as expected. The maximum efficiency is obtained at the average flow rate that equals the half of the Q_{max} as 0.067 %; based on the linearity between the pressure load and the average flow rate. To calculate the efficiency, we also have:

$$\eta_{max} = 100 \frac{\Delta P_{max} Q_{max}}{4\Pi_{max}} \tag{4.14}$$

where Π_{max} is the time-averaged maximum power exerted on fluid in $\Omega(t)$ for specified wavelength, λ, frequency, f, and amplitude, B_o. The power, Π_{max}, remains nearly constant as the flow rate or the applied pressure varies. Note that, under varying power conditions with the flow rate and the pressure load for a fixed operating condition, linear dependence between the pressure and the average flow rate observed in Figure 4.8 would no longer be valid.
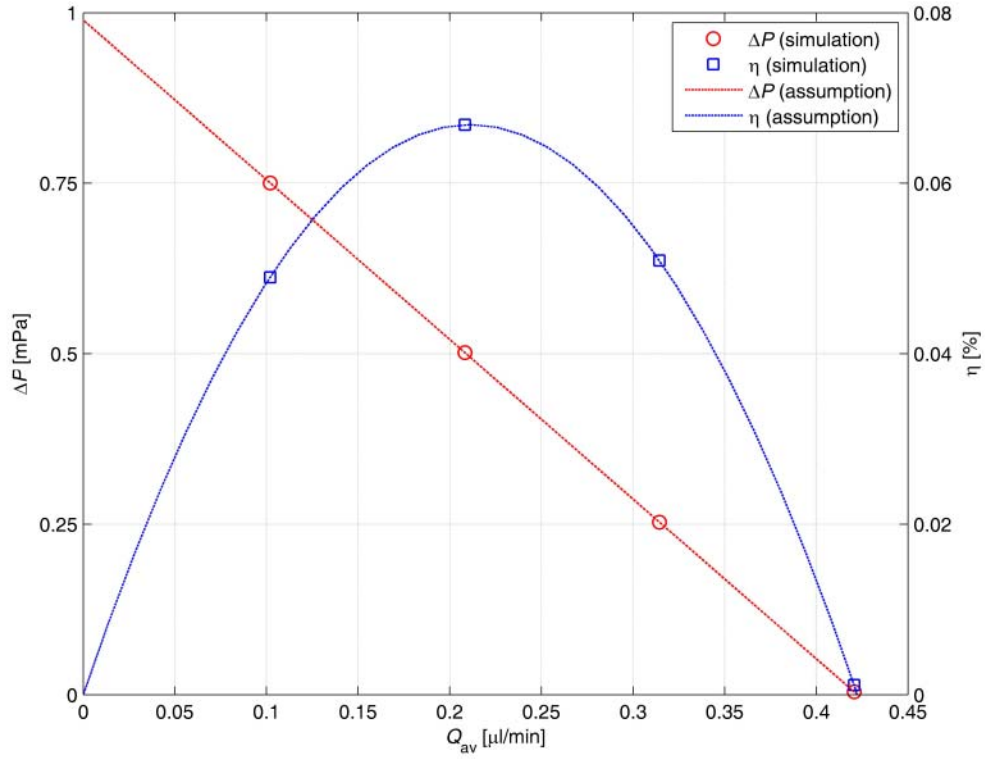
Figure 4.8: 2D Pump; inlet-to-outlet pressure increase, ΔP, and efficiency, η, vs. time-averaged flow rate, Q_{av}, for the base case, $\lambda = 125$ μm, $B_o = 14.5$ μm, and $f = 2$Hz; results indicated with symbols are from numerical simulations, and dashed lines indicate the linearity of ΔP with Q_{av}.

4.1.1.5 Parametric Study-2: Maximum Values

All results discussed under the following section correspond to the maximum values represented in characteristic pump curve plot (Figure 4.8) and they are all in dimensional form. In Figures 4.9, 4.10 and 4.11, variations of the maximum values of time-averaged flow rate for zero ΔP in the channel (in Figures 4.9-(a), 4.10-(a) and 4.11-(a)), the maximum pressure difference for zero time-averaged flow rate (in Figures 4.9-(b), 4.10-(b) and 4.11-(b)), the rate-of-work done on the fluid (in Figures 4.9-(c), 4.10-(c) and 4.11-(c)), and maximum pump efficiency (Figures 4.9-(d), 4.10-(d) and 4.11-(d)), an extra quantity, are plotted against the wavelength in Figure 4.9, frequency in Figure 4.10 and the amplitude in Figure 4.11 respectively. In Figures 4.9, 4.10 and 4.11, the base case conditions are set to $\lambda = 1.25$ mm, $B_o = 14.5$ μm and $f = 2$Hz.

69

For shorter wavelengths than half of the film's length, the maximum flow rate and maximum pressure load decrease with increasing wavelength as depicted in Figures 4.9-(a) and 4.10-(b). For the same range of wavelengths, the power exerted on the fluid tends to decrease with a faster rate than the one for Q_{max} and ΔP_{max} as in Figure 4.9-(c). Hence the efficiency tends to decrease with a rate similar to that of Q_{max} and ΔP_{max}. Unfortunately, it is harder to quantify the rates especially for Q_{max} and ΔP_{max}, as there are not enough data points especially for short wavelengths due to numerical instability of the solutions as the resolution of each wave requires increasing number of mesh nodes on the film, which, in turn, poses a difficulty in deforming mesh calculations. However for the power, one can argue that Π_{max} is proportional to $1/\lambda$.

For larger wavelengths than about the half of the film's length, in a relatively small intermediate regime Q_{max} and ΔP_{max} increase with the wavelength for up to about twice the length of the film as can be observed in Figures 4.9-(a) and 4.9-(b). Further increase in the wavelength do not yield larger flow rates or pressure increase in the channel due to the shape function which results in a simple vertical motion of the film without an effective wave propagation and, hence, pumping.

In that window, power exerted on the fluid observed in Figure 4.9-(c) increases with the wavelength with a faster rate than that of Q_{max} and ΔP_{max}. In combination of responses of the flow rate, pressure and the power, the efficiency of the pump drops with the increasing wavelength as in Figure 4.9-(d).

In Figure 4.10, the frequency is varied while the wavelength and the amplitude are kept at their reference values. Hence, the flow regime corresponds to the case for large wavelengths. Increasing the frequency results in increased flow rate, pressure and the power, but efficiency remains unaffected from the frequency variations. From Figures 4.10-(a) and 4.10-(b), one can easily inspect that the Q_{max} and ΔP_{max} vary linearly with the frequency, i.e. $Q_{max} \sim f$, and $\Delta P_{max} \sim f$. From Figure 4.10-(c), it is observed that the power exerted on the fluid varies with the square of the frequency, i.e. $\Pi_{max} \sim f^2$. Therefore the efficiency remains constant at its reference value (.067 %).

Lastly, it is observe that the flow rate in Figure 4.11-(a), pressure in Figure 4.11-(b), power 4.11-(c), and, hence, the efficiency in Figure 4.11-(d) increase with the square of the amplitude, i.e. $Q_{max} \sim B_0^2$, $\Delta P_{max} \sim B_0^2$, $\Pi_{max} \sim B_0^2$, and $\eta \sim B_0^2$. These results are all in agreement with the results discussed so far, i.e. the asymptotic results for upstream velocity and power consumption are totally match with the

numerical results. Moreover, offered results exhibit an inverse relationship between the power and the wavelength capturing the asymptotic result reported by Childress (1981) for infinite-sheet in infinite-medium in full for small wavelengths compared to the film's length and the channel height as in Figure 4.9-(c). Hence the disagreement between small and large wavelengths stated in previous sections is resolved by numeric investigation for infinite waving sheet (membrane).
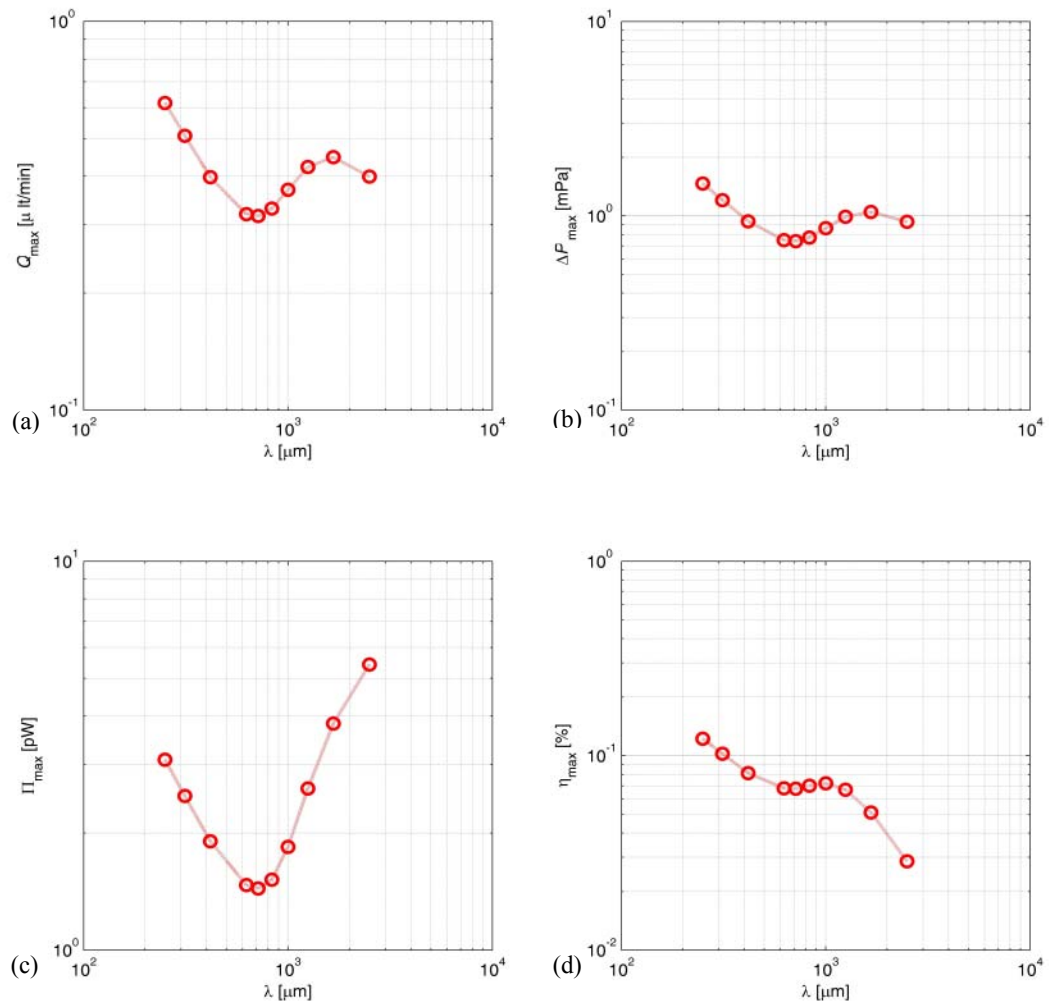

Figure 4.9: 2D Pump; flow rate for zero pressure load (a), pressure rise for zero flow rate (b), pressure (c) and efficiency (d) vs. the wavelength.
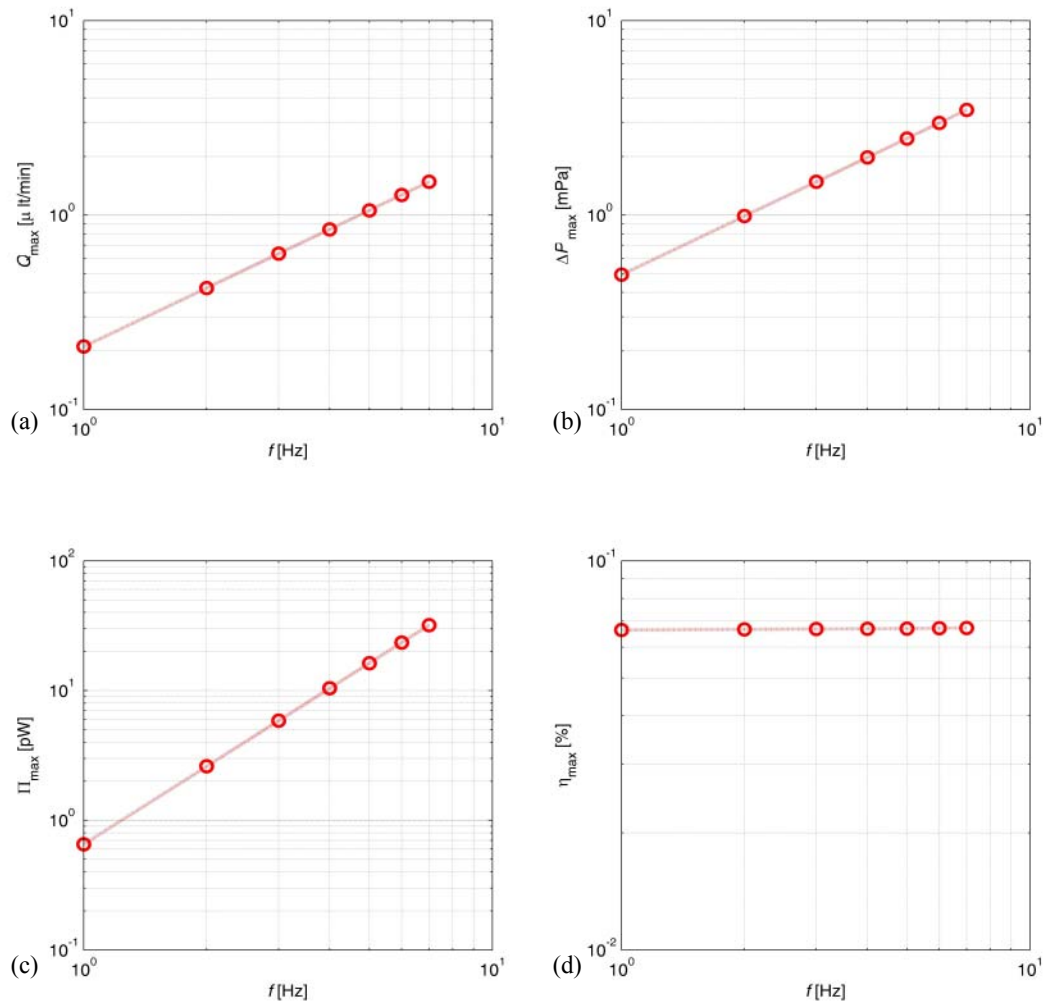
Figure 4.10: 2D Pump; flow rate for zero pressure load (a), pressure rise for zero flow rate (b), pressure (c) and efficiency (d) vs. the frequency.
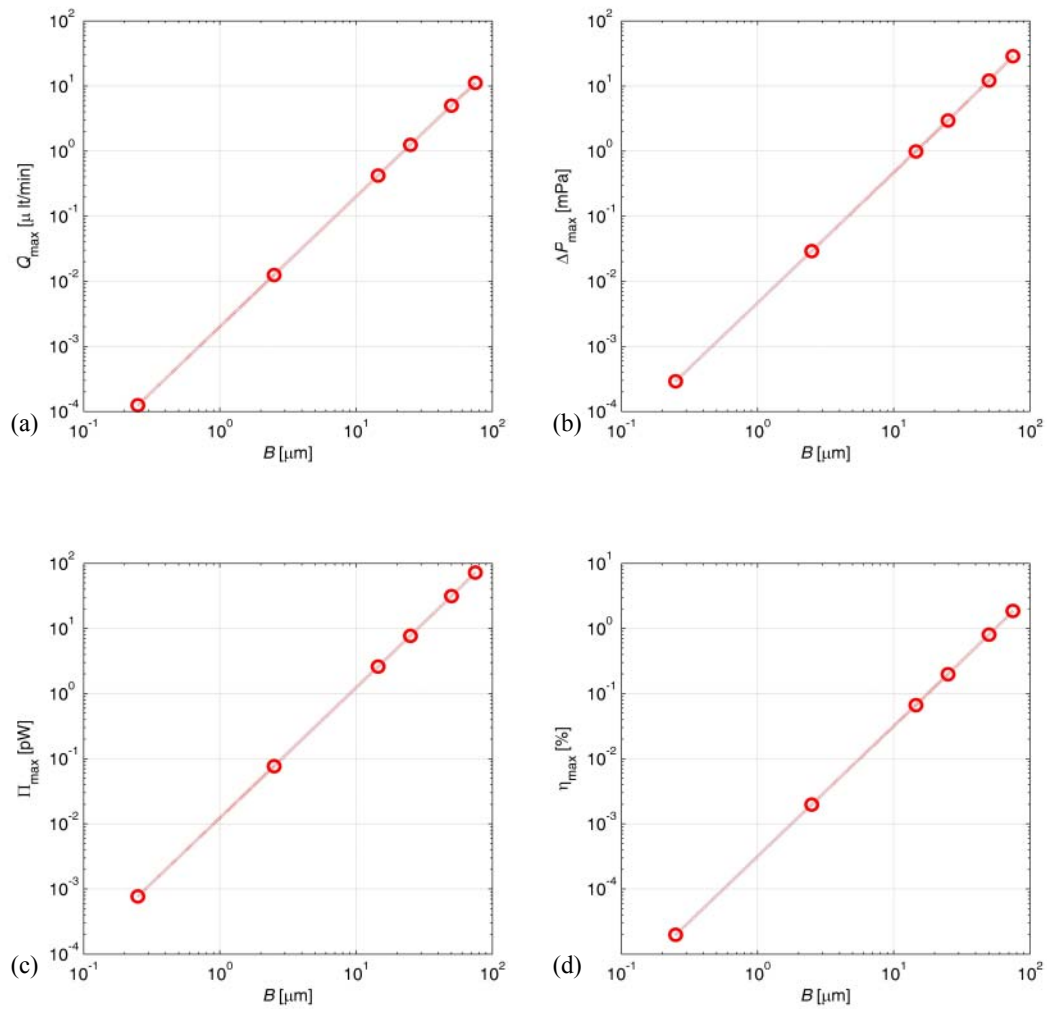
Figure 4.11: 2D Pump; flow rate for zero pressure load (a), pressure rise for zero flow rate (b), pressure (c) and efficiency (d) vs. the amplitude.

4.1.1.6 Parametric Study-3: Combined Effects of the Design Parameters

Final comments on parametric 2D pump results will be on 'combined effect constants', quantities generated to explain the pump behavior in a combination of all design parameters discussed so far. In Figure 4.12-(a), combined effects of the amplitude and the frequency for constant wavelength and channel height is put together to characterize the flow rate. From what are depicted in Figures 4.5-(a), 4.6-(a) and 4.7-(a), a flow rate parameter is defined as follows:

$$C_Q = \left(\frac{B_0}{H}\right)\left(B_0^*\omega^*\right)\sqrt{\lambda^*} \qquad (4.15)$$

Dimensionless average flow rate which is based on the scales provided in Tables 3.1 and 3.2 scales with the flow rate parameter, C_Q, given in equation (4.15). As the wavelength dictates the flow regime of the finite-length film, only a portion of the wavelength simulations match to this general behavior for wavelengths comparable to the base case, which is used in other simulations for amplitude, frequency and the channel height.

In Figure 4.12-(b), time-averaged power exerted on the fluid is plotted against a power parameter that puts together the parametric behavior of nondimensional power, which is shown in Figures 4.5-(b), 4.6-(b) and 4.7-(b), as given by:

$$C_\Pi = \left(\frac{B_0}{H}\right)^2\left(\frac{\lambda}{H}\right)\omega^{*2} \qquad (4.16)$$

All four curves coincide except for the parametric wavelength curve, which matches to others only partially, as also observed in Figure 4.12-(b) and discussed above. The power coefficient given by (4.16), in effect, is derived for constant viscosity. It is clear that the power exerted on the fluid must scale with the viscosity of the fluid linearly. In fact, an alternate and common nondimensionalization of the pressure and shear stress is based on the scale, $\mu U_0/\ell_0$. If the viscosity were used in nondimensionalization of stress variables and the power, then, without loss of generality (4.16) would have been used directly without including the effect of viscosity additionally in practical calculations.
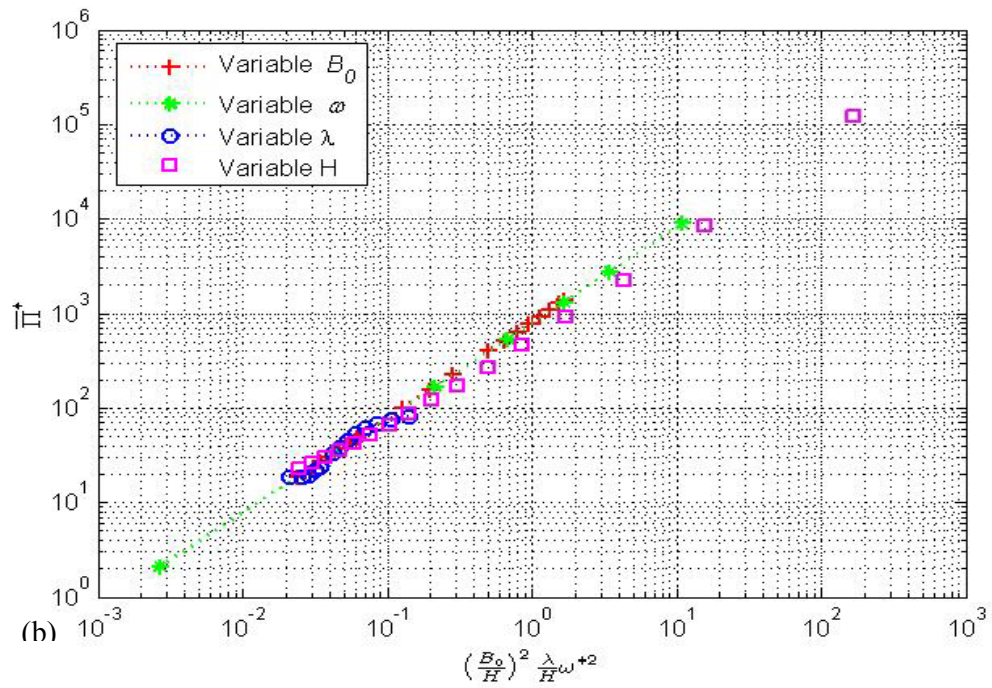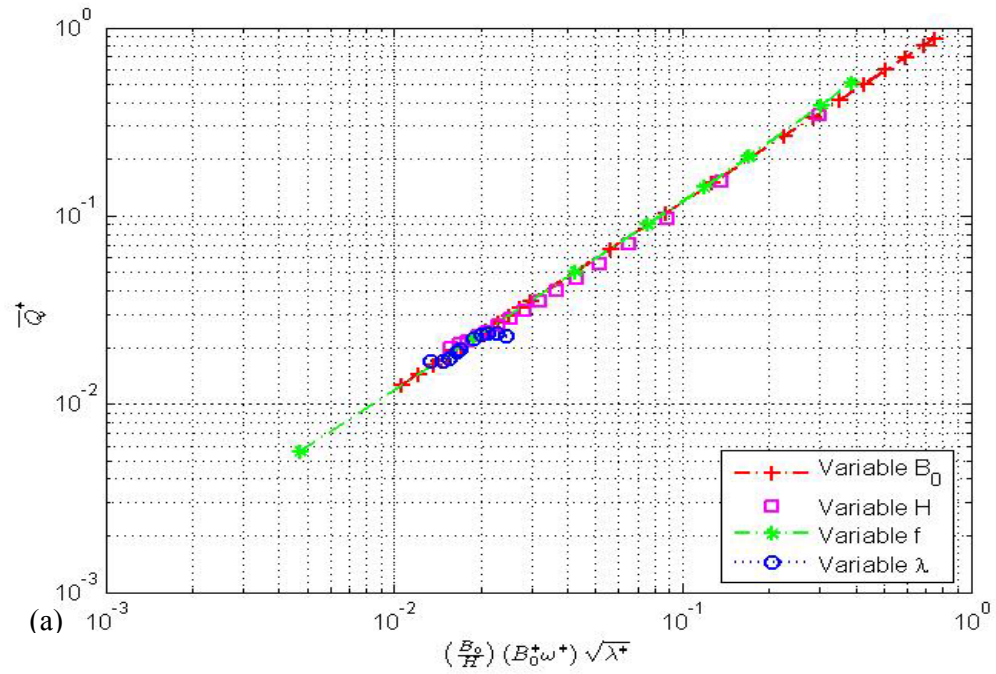
Figure 4.12: 2D Pump; (a) combined effects of the amplitude and the frequency for constant wavelength and channel height on time averaged flow rate vs. the flow rate parameter; (b) combined effects of the amplitude and the frequency for constant wavelength and channel height on time averaged power exerted on fluid vs. the power parameter.

4.1.2 3D Pump Results

The general idea presenting 2D pump results in previous section was to show that it is possible to push the fluid in the vicinity of a waving boundary. This section is dedicated to elaborate the flow and pump characteristics when both channel and waving membrane is finite. Simulations carried out with dimensionless parameters and results transformed into dimensional form later on with a similar procedure described in the previous section.

4.1.2.1 Dimensionalization Process

Dimensionalization procedure for 3D pump design is carried out for the constants that are given in Table 3.4. To summarize once more, to get the dimensional quantities out of dimensionless simulation outputs, it is essential to invoke scaling factors satisfying the Re < 1 condition. Hence dimensional results can be obtained by

$$\ell_{\text{dim}} = \ell^* \ell_0, \quad \mathbf{U}_{\text{dim}} = u^* U_0, \quad t_{\text{dim}} = t_0 / f^*, P_{\text{dim}} = P^* P_0 \text{ and } \quad \Pi_{\text{dim}} = \Pi^* \Pi_0 \quad \text{where}$$

subscript 'dim' stands for dimensional quantity.

4.1.2.2 Analysis of Operating Principles

Vertical motion of the fully submerged elastic membrane causes dynamic high and low pressure regions resulting in a flow between them. As the deformation shifts position accordingly with the propagation of traveling waves, high and low pressure regions in the vicinity of the membrane demonstrate consequential shifts which result in a net flow in propagation direction. This relation between pressure and deformation was deduced by means of work exerted on the fluid by the deforming membrane.

Numerical results that are presented here are obtained for water flow in a pump whose dimensions are listed in Table 3.3. Nondimensional equations are used in the simulations. Results presented here depend on parameterized flow conditions namely the wave-amplitude, B_o, excitation frequency, f, and the ratio of the widths of the membrane and the channel, W_f / W_{ch}. Time-averaged quantities are obtained from integration over the last two cycles. Unless otherwise noted the base case used in the simulations corresponds to $\lambda = 50$ μm, $B_o = 5$ μm, $f = 112$ Hz, and $W_f / W_{ch} = 0.5$.

In Figures 4.13 and 4.14 pressure distribution on the center symmetry plane with deformed membrane structure and instantaneous streamlines are shown for the base case at $t = 6$. Pressure variations take place in the vicinity of the membrane away from the top and bottom walls of the channel parallel to the flow direction and away from the channel entrance and exit. Therefore it is reasonable to claim that there is a uniform flow at the channel entrance and exit owing to this localization of the pressure variations in the membrane's vicinity. Instantaneous streamlines are uniform near the inlet, exit and away from the membrane. Furthermore, having sides of the membrane exposed to the flow results in downstream vortex formations around and behind the membrane. As membrane width gets comparable with the channel width, lateral wall shear effects cause a sharper velocity gradient in Z-direction due to the no-slip boundary conditions invoked on both membrane and wall surfaces. This effect would trigger an enlarged high-velocity-zone display on exit velocity profile.

Figures 4.15, 4.16 and 4.17 demonstrate the velocity profiles on different sections of the half-channel via arrow plots for $\lambda = 50$ μm, $B_o = 5$ μm, $f = 112$ Hz, and $W_f/W_{ch} = 0.5$ with $W_{ch} = 200$ μm at simulation time $t = 6$. Velocity field is steady in both inlet and outlet of the channel despite the large vortices formed by the free end of the membrane.
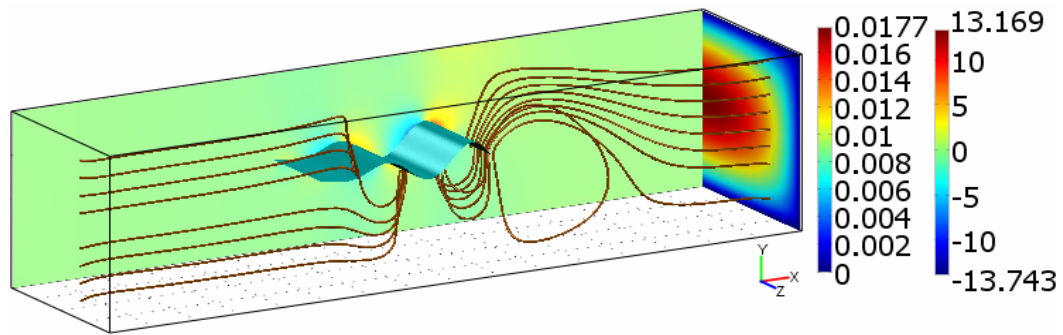

Figure 4.13: 3D Pump; snapshot of the streamlines from inlet and outlet of the channel both ending on bottom surface of the membrane, pressure distribution on the symmetry plane, and the exit velocity distribution at $t = 6$. First color bar stands for the nondimensional velocity profile on outlet half plane; second color bar stands for nondimensional pressure profile on the symmetry plane.
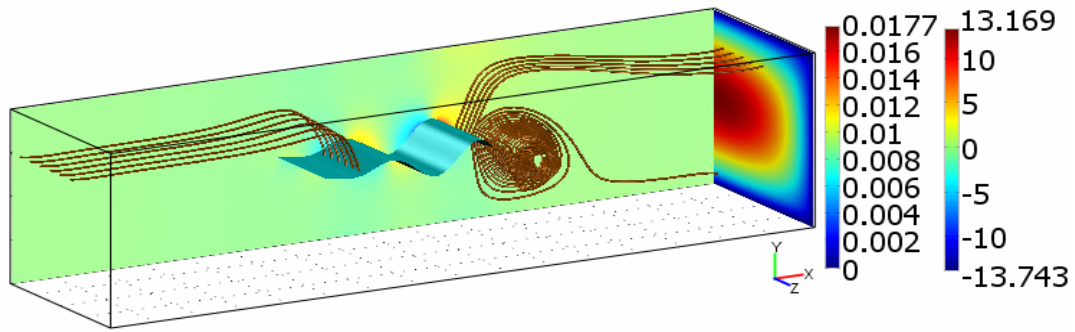
Figure 4.14: 3D Pump; snapshot of the streamlines from inlet and outlet of the channel both ending on top surface of the membrane with the circulation formed behind the membrane ending on outlet, pressure distribution on the symmetry plane, and the velocity distribution at the exit. First color bar stands for nondimensional velocity profile on outlet half plane; second color bar stands for nondimensional pressure profile on the symmetry plane.
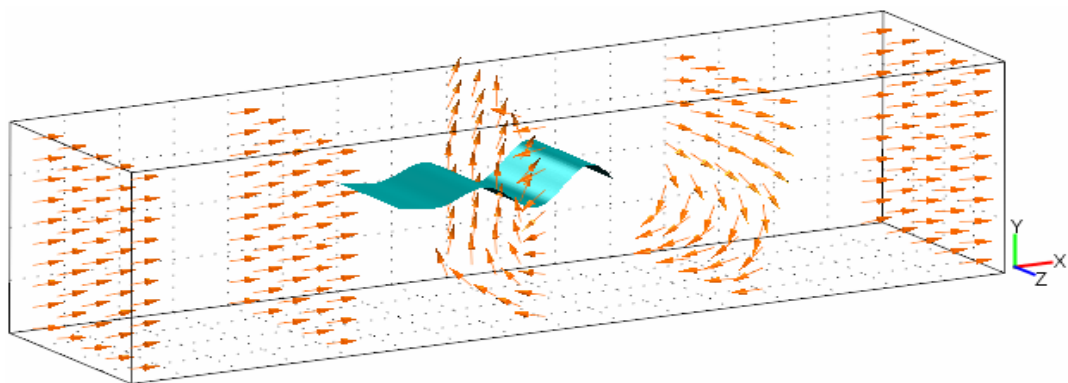
Figure 4.15: 3D Pump; normalized velocity vectors on YZ planes at $X = $ -2, -1, 0, 1, 2.
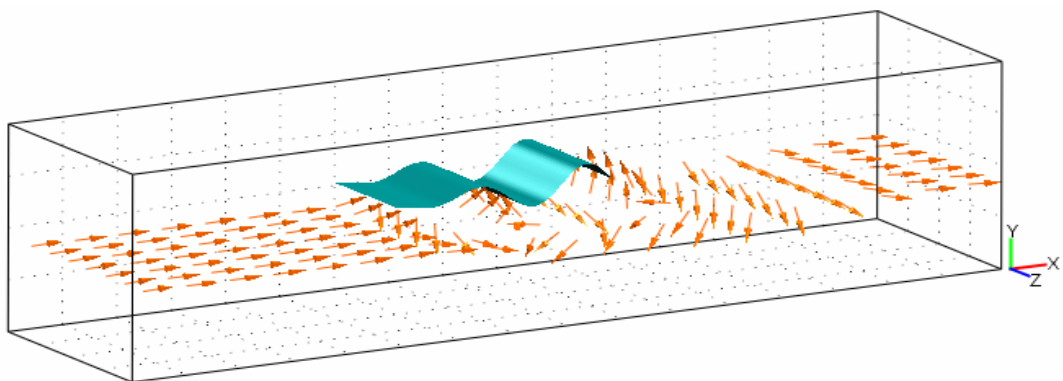
Figure 4.16: 3D Pump; normalized velocity vectors on XZ plane at $Y = $ -0.1.
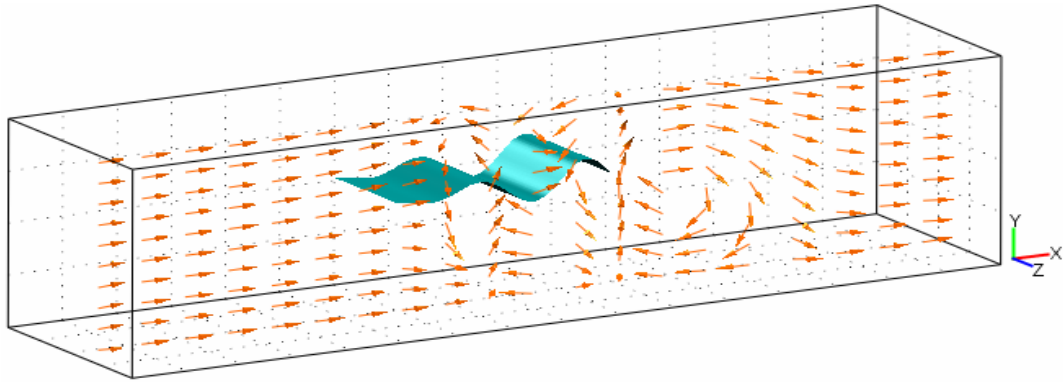
Figure 4.17: 3D Pump; normalized velocity vectors on *XY* plane at *Z* = 0.6.

4.1.2.3 Parametric Study: Parametric Analysis of Time-Averaged Results

Figure 4.18, demonstrates the relationship between the amplitude and the average flow rate for all the variables fixed at the base case except the amplitude. As amplitude increases the average flow rate increases quadratically with the amplitude which is in agreement with the asymptotical predictions [64], [70] and earlier published 2D numerical results [95]. Slight deviation from quadratic relationship at large amplitudes is due to increased interaction of the three-dimensional flow with the channel walls. Further simulations are necessary to elucidate this slight leveling behavior.
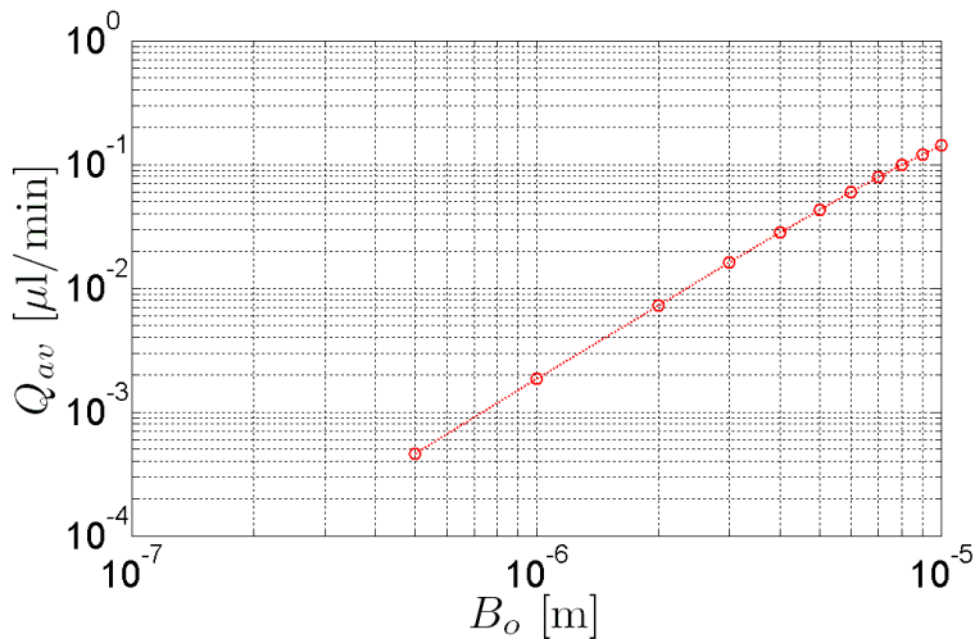
Figure 4.18: 3D Pump; amplitude vs. average flow rate for W_f/W_{ch} =0.5 and f = 112 Hz.

Figure 4.19 demonstrates the relationship between the wave-amplitude, B_o and the time-averaged power consumption, Π_{av}, which is also quadratic with the amplitude, and in agreement with the asymptotic solutions given by Childress (1981) and two-dimensional simulation results [95].
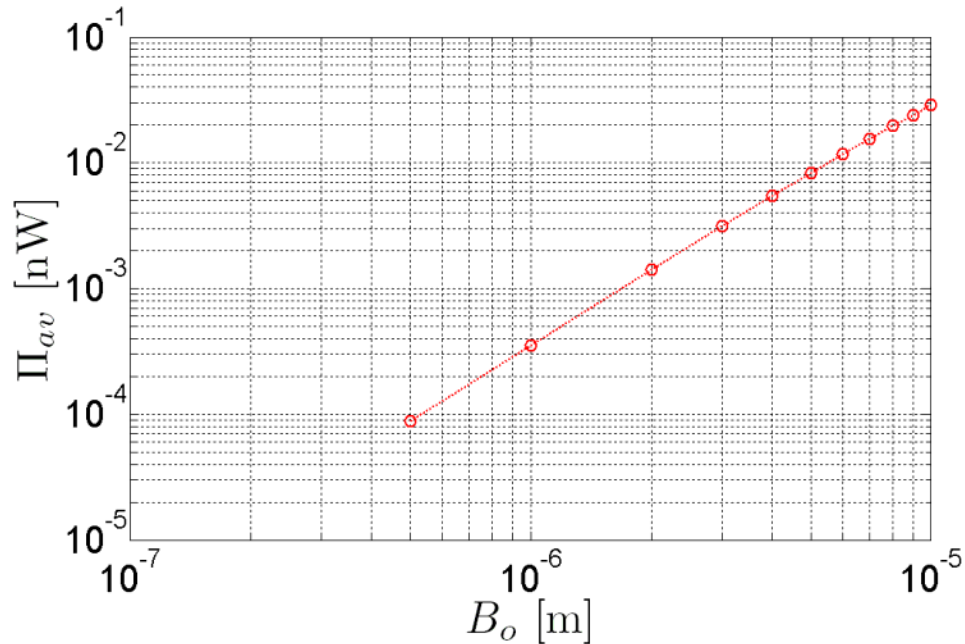

Figure 4.19: 3D Pump; amplitude vs. average power consumption for W_f/W_{ch} =0.5 and f = 112 Hz.

Figure 4.20 demonstrates the relationship between the average flow rate and the frequency for all the variables fixed at the base case except the frequency. The average rate of work done on the fluid Π_{av} varies quadratically with the frequency as depicted in Figure 4.21. The effect of the frequency, also, agrees well with the asymptotic results [64], [70] and previous numeric results, where small amplitude choice was mathematically justified and numerical results obtained by the previous 2D simulations [95].
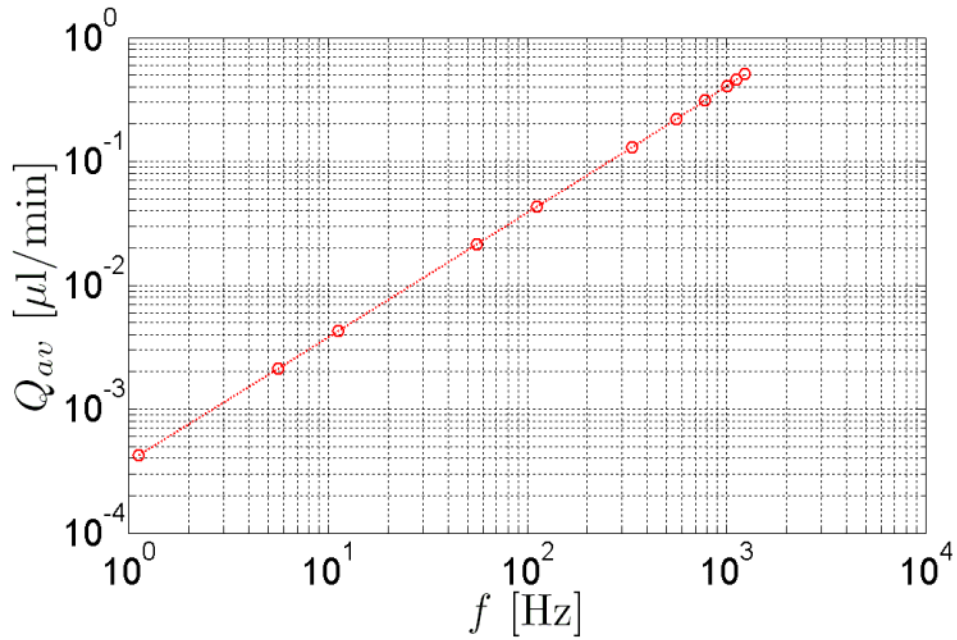
Figure 4.20: 3D Pump; frequency vs. average flow rate for $\lambda = 0.5\ell_f = 0.5H = 0.5W_f = 50$ μm, $W_f/W_{ch} = 0.5$ and $B_o = H/20 = 5$ μm.

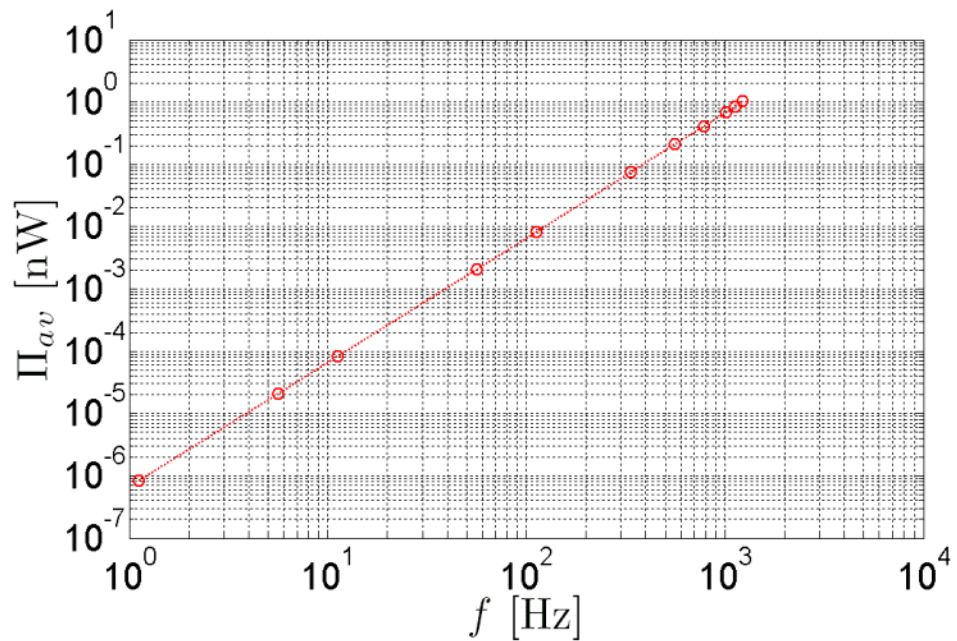Figure 4.21: 3D Pump; frequency vs. average power consumption for $W_f/W_{ch} = 0.5$ and $B_o = 5$ μm.

Figures 4.22 and 4.23, display the effect of the ratio of the membrane's width to the channel width on the average flow rate and the rate of work done on the fluid. In simulations that correspond to data points on the graph, width ratio is adjusted by means of adjusting the membrane's width and fixing the other variables at the base case. As the

81

width of the channel approaches to the width of the membrane, i.e. $W_f/W_{ch} \to 1$, not only the flow rate (Figure 4.22) but also the average power increases rapidly, hinting that the gap between the membrane and the channel's side walls play a very important role in addition to increasing membrane area. In fact, when the ratio goes to zero, i.e. $W_f/W_{ch} \to 0$, both the power and the flow rate increases almost linearly.

The average flow velocity, which is given by Q_{av}/A_{ch}, is plotted against the width ratio in Figure 4.24. Clearly, as the ratio increases, i.e. the membrane width increases, the membrane becomes more effective in propulsion. For large width ratios, $W_f/W_{ch} > 0.5$, as the width ratio decreases, momentum flux into the Z-direction drains the available mechanical energy and reduces the net propulsion. On the other hand, for small width ratios, the average velocity tends to approach a limit, which, presumably, corresponds to the average velocity of the swimmer in an infinite medium.

Area averaged power consumption, which is computed by Π_{av}/A_f, is plotted against the width ratio in Figure 4.25. Even though total power consumption increases, power consumption per unit area drops almost linearly for small width ratios, which may be due to decreasing flow in the Z-direction. For large width ratios, area-averaged rate-of-work done on the fluid does not vary significantly.

As membrane width becomes comparable with channel width, flow rate and total power consumption approaches to a limit value as can be observed in Figures 4.22 and 4.23. Elimination of parasitic effects results in reduced power consumption per unit area as illustrated in Figure 4.25.
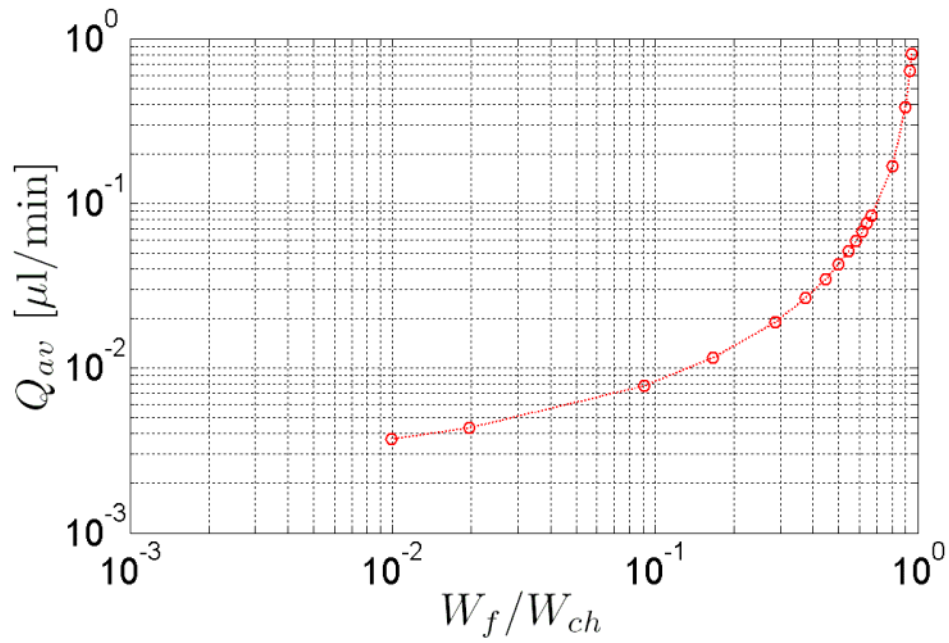
Figure 4.22: 3D Pump; W_f/W_{ch} vs. average flow rate for $B_o = 5$ μm and $f = 112$ Hz.

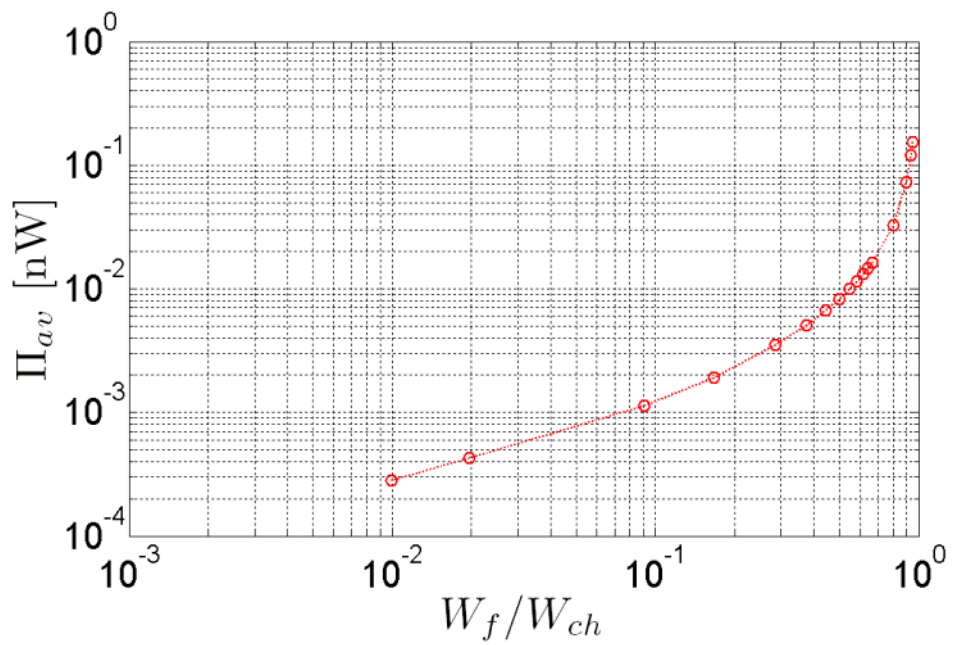Figure 4.23: 3D Pump; W_f/W_{ch} vs. average power consumption for $B_o = 5$ μm and $f = 112$ Hz.
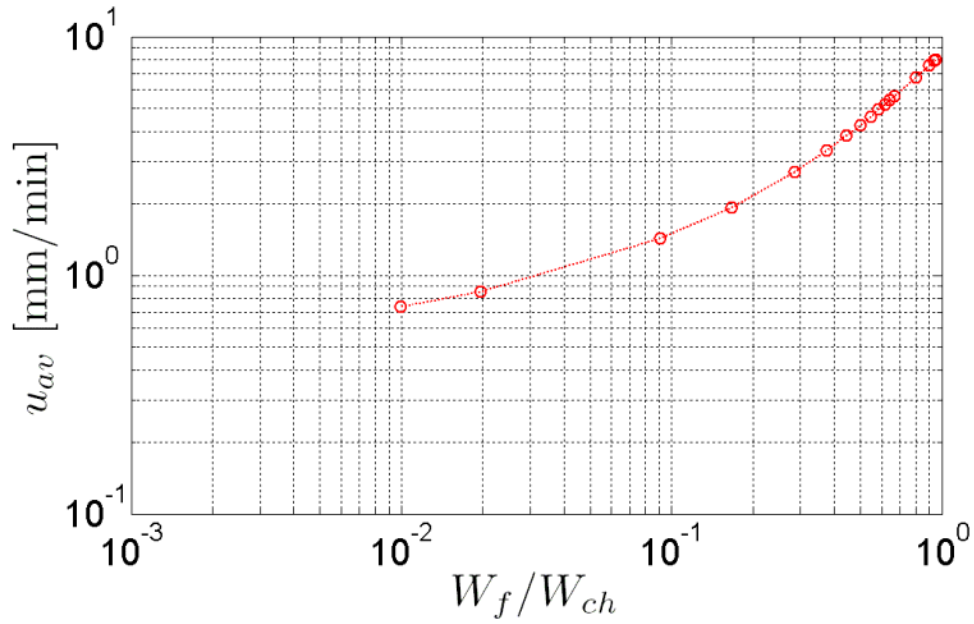
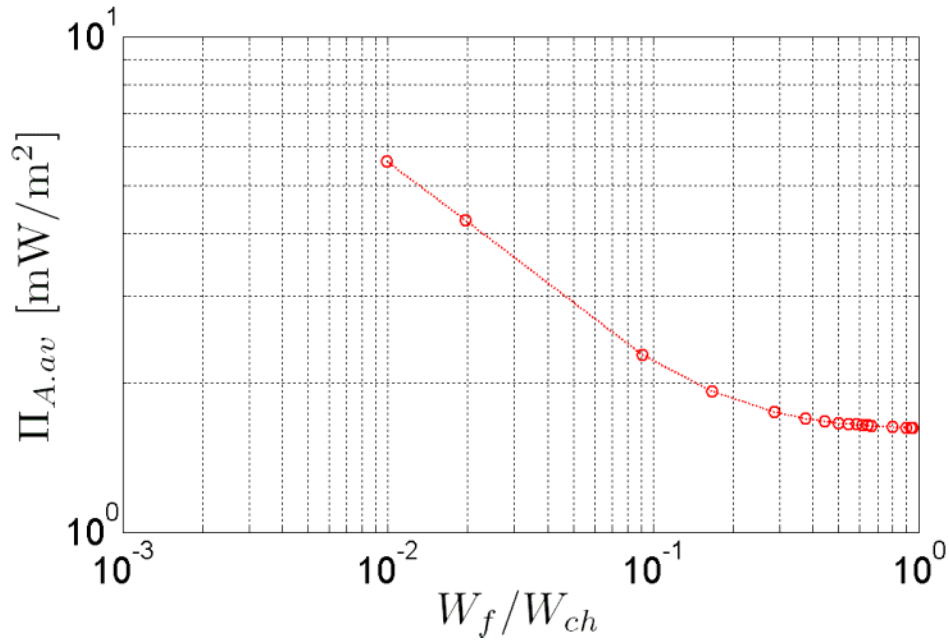Figure 4.24: 3D Pump; W_f/W_{ch} vs. average velocity for $B_o = 5$ μm and $f = 112$ Hz.

Figure 4.25: 3D Pump; W_f/W_{ch} vs. power consumption per unit area for $B_o = 5$ μm and $f = 112$ Hz.

4.1.2.4 Characteristic Pump Curve

Pressure head and efficiency dependency on the flow rate are shown in Figure 4.26 for the micropump that operates at the base case, for which $B_o = 5$ μm, $W_f/W_{ch} = 0.5$ with and $f = 112$ Hz. For simulations corresponding to the date points in the figure,

outlet pressure is kept at zero and the inlet pressure is varied. Calculated flow rates for the prescribed pressure difference between the exit and the inlet, $\Delta P = P_{out} - P_{in}$, are shown in Figure 4.26. Furthermore, the efficiency of the micropump is calculated and plotted as a function of the average-flow rate on the right-axis of the plot in Figure 4.26. Similarly to an ideal pump, the pressure head vs. the flow rate is linear, and the efficiency is parabolic. The maximum flow rate for zero pressure head and the maximum pressure head for zero flow-rate are about 0.04 µl/min and 40 mPa respectively. Moreover, the maximum efficiency takes place at the half of the maximum flow rate, i.e. $Q_{av} = 0.02$ µl/min, and is 0.085%. Note that, in general, micro fluidic devices have small efficiencies because of the dominance of the viscous effects [10].
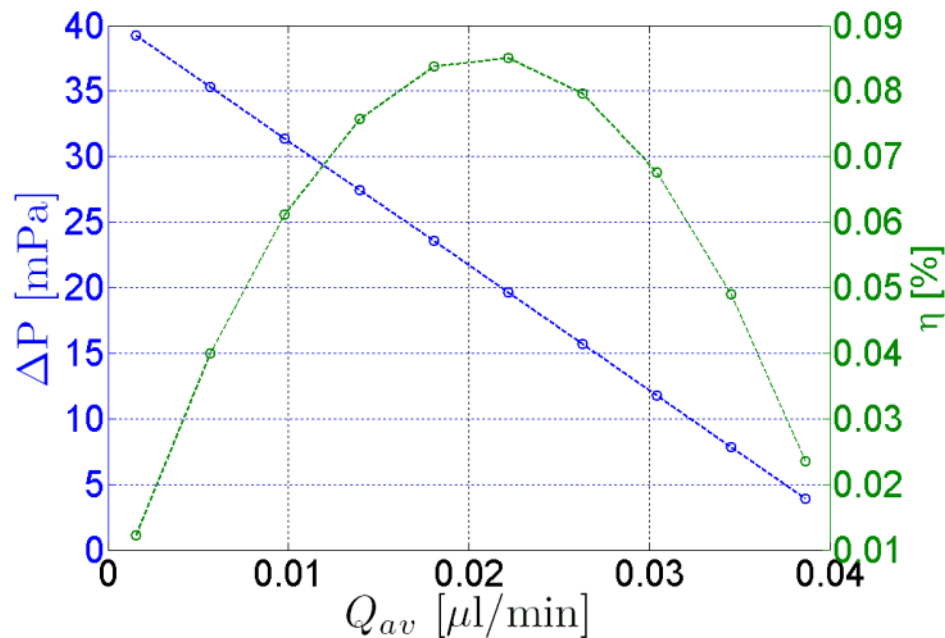

Figure 4.26: 3D Pump; pressure head (blue circles, left axis) and efficiency (green circles, right axis) of the micropump as a function of the flow rate. Each data point corresponds to a numerical simulation for which pressure boundary conditions are specified according to the corresponding pressure head.

4.1.3 Final Remarks for Pump Analysis

A biologically inspired micropump actuation mechanism is reported in this section. The effects of some of the performance variables such as the channel height, wavelength, wave amplitude, excitation frequency and width ratio between membrane and channel are demonstrated by means of two-dimensional and three-dimensional time-

dependent simulations of the flow. Flow induced by traveling-plane-wave deformations on the thin-membrane that has finite dimensions and is placed inside a channel is modeled by incompressible isothermal Stokes and Navier-Stokes equations on a deforming mesh due to moving boundaries. In the former Stokes case, deformation of the mesh is given as boundary condition and for the later Navier-Stokes case mesh is given as prescribed condition and an arbitrary Lagrangian Eulerian method is used to ensure the physical solution via Winslow smoothing method in each case.

Based on our numerical results, the flow rate increases linearly with the excitation frequency and quadratically with the amplitude. Similarly, the dependence of the rate-of-work done on the fluid is quadratic with both the frequency and the amplitude. The average velocity of the flow increases almost linearly with the increasing width of the membrane. However, the area-averaged power tends to converge to a limit as the width ratio increases. Therefore, from the geometric design point-of-view, it is recommended to limit the space between the membrane and the channel's side walls for better efficiency and higher flow rates. Although 3D and 2D interpretations are different, i.e. one is an arbitrary slice of an infinite medium, other is a finite medium respectively; numerical results clearly show that the flow induced by the waving motion on a membrane surface has the properties suggested by the asymptotical results to the analytical studies carried out long before [64], [70] and [66].

Finally, the performance of a typical micropump that uses traveling-plane-wave deformations on a thin membrane inside a channel for flow and pressure head is obtained and reported. The micropump has similar characteristics compared to its counterparts using other mechanisms.

4.2 3D Swimmer Results

In contrast with pump simulations, 3D swimmer simulations were carried out for dimensional quantities with relatively larger dimensions. Head piece is bullet shaped geometry and tail is a conical structure, different from the 2D case as shown in Figures 4.22-4.25 which is supposedly the more realistic case. It is decided to choose the geometry to the head piece with relatively larger cross-sectional area since head is supposed to home the controller electronics and power supply system when swimmer is built although exact size is uncertain for now. It is noted that no control algorithm is

utilized in this study. Once more, the main equations solved for this simulation batch are as follows:

$$\left(\frac{\partial \mathbf{U}}{\partial t} + \mathbf{u}_\mathrm{r} \cdot \nabla \mathbf{U}\right) = -\nabla P + \frac{1}{\mathrm{Re}} \nabla^2 \mathbf{U} \tag{4.17}$$

$$\nabla \cdot \mathbf{U} = 0 \tag{4.18}$$

$$\frac{\partial^2}{\partial x^2} \mathbf{X} + \frac{\partial^2}{\partial y^2} \mathbf{X} = 0 \tag{4.19}$$

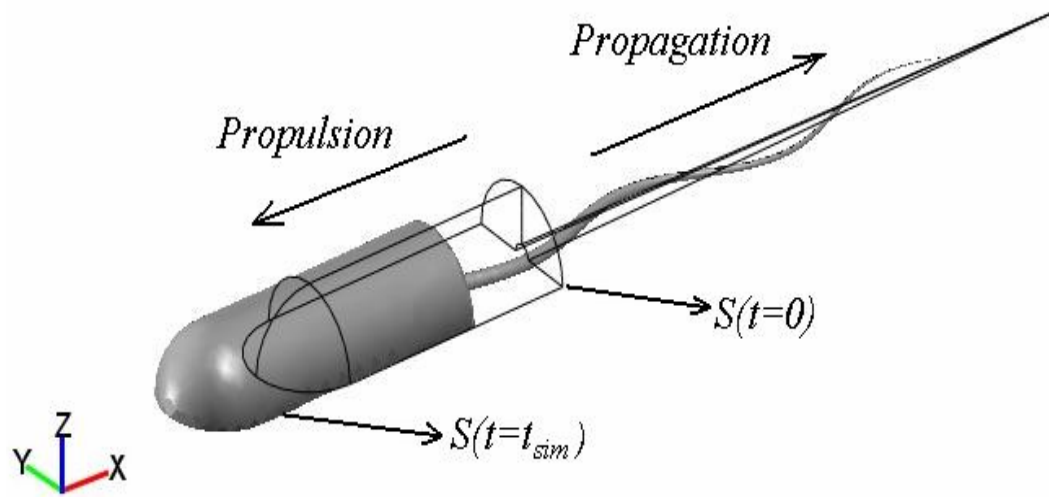### 4.2.1 Analysis of Operating Principles

Figure 4.27: 3D swimmer; wave propagation and swimmer propulsion takes place on the same axis but opposite directions (Simulation time t=20).

In Figure 4.27 net motion of swimmer surface is illustrated. Notice that propagation and net propulsion action takes place on opposite directions but on the same axis. Base case run is made for $\lambda = 625$ μm, $B_\mathrm{o} = 45.625$ μm, $f = 1$ Hz and $C_{sh} = 6$. Time averaged quantities are obtained from integration over the last two cycles long after initial ramp is completed. All propagation basics are a kin to the pump models except for propulsion phenomenon. Vortex formations occur behind the swimmer as can be observed in Figure 4.28. Vortex formations in microrealm are energy draining phenomenon while in macrorealm it is possible to extract power from vortices causing tremendous swimming efficiencies [100].

Optimum flow efficiency occurs for combined values of 0.4>St>0.25 and 106>Re>104 [63] which obviously is the reason why it is not included within the microflow context in detail. While forward motion takes place head piece pushes the fluid on the propulsion direction due to no-slip conditions as illustrated in Figure 4.29.
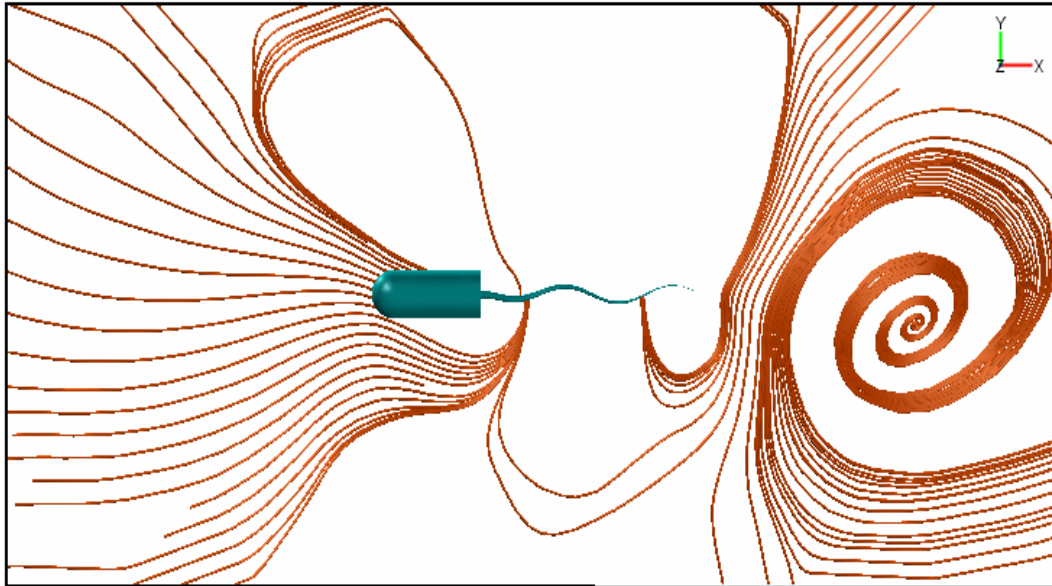

Figure 4.28: 3D Swimmer; normalized streamlines around the swimmer, view from *XY* plane. Notice that vortex formations do not take place in front of the swimmer (Simulation time *t*=2 sec).

Flow fields illustrated in Figures 4.28 and 4.29-(a)-(b) demonstrates the counter flows coexisting. As can be observed in Figure 4.28, the flow field in front of the swimmer body is not disturbed since the *X*-velocity is bigger than the *Y*-velocity as will be demonstrated in Figures 4.30 and 4.31. On the other hand the flow field in the vicinity of the tail contains vortex structures due to the existence of larger counter flow fields due to waving action as can be inspected in Figure 4.29-(b) since the *Y*-velocity on the tail is comparable with the propulsion velocity. Larger alternating *Y*-velocities introduce considerable perturbations to the flow. This phenomenon takes place especially when tail velocity changes sign and immediately confronts the flow field created by the previous reverse motion. The vortex structure located behind the swimmer forms due to the free tail end which causes the same effect. Also wider domain allows bigger vortex structures to form. Due to high surface forces all these vortex structures drain the mechanical energy by means of shear losses.
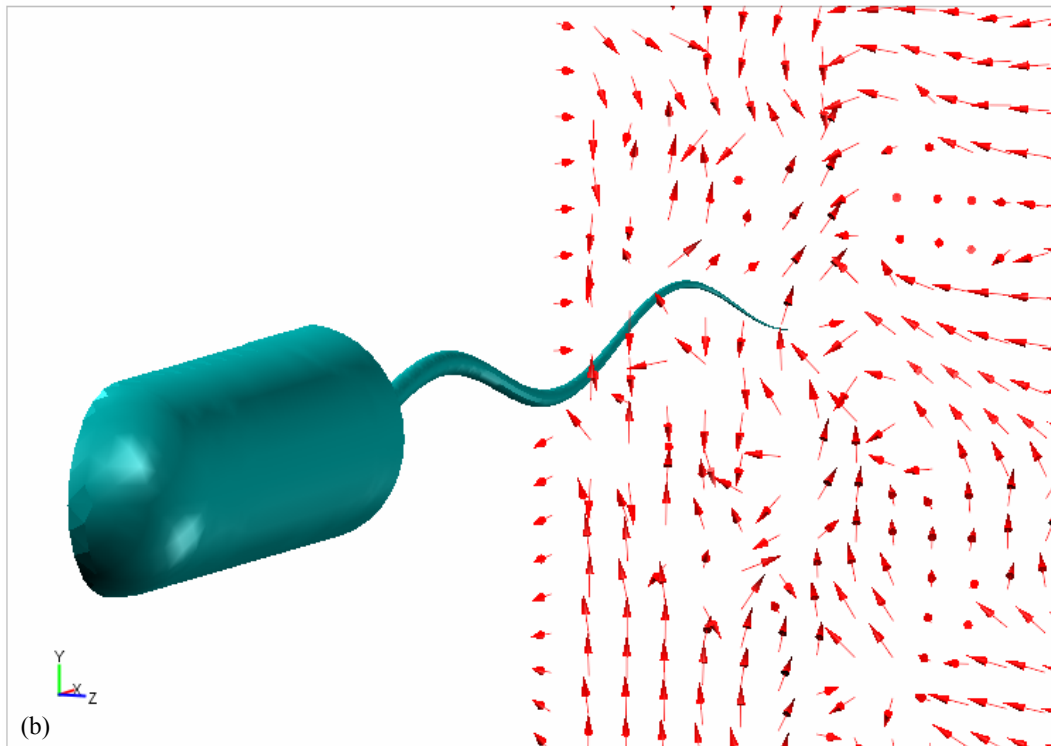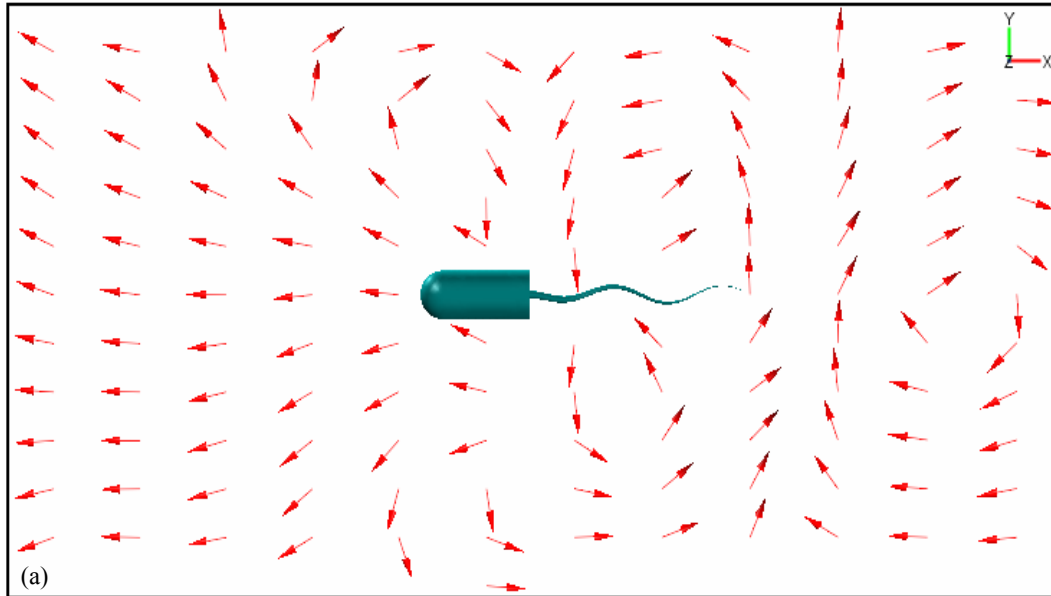
Figure 4.29: 3D Swimmer; (a) velocity field depicted via normalized 3D arrows on *XY* symmetry plane. Notice that head pushes the flow towards the propulsion direction forming homogeneous flow field and rotational flow field exists on both sides of the tail (*t*=3); (b) velocity profile on *YZ* plane where $X_f = \ell_f / 2$ at simulation time *t*=2.75.

Notice that fluid velocity is almost homogeneous below and above the tail on the symmetry plane; two opposite fields meet head-on on the very neighbor causing random vortex formations.
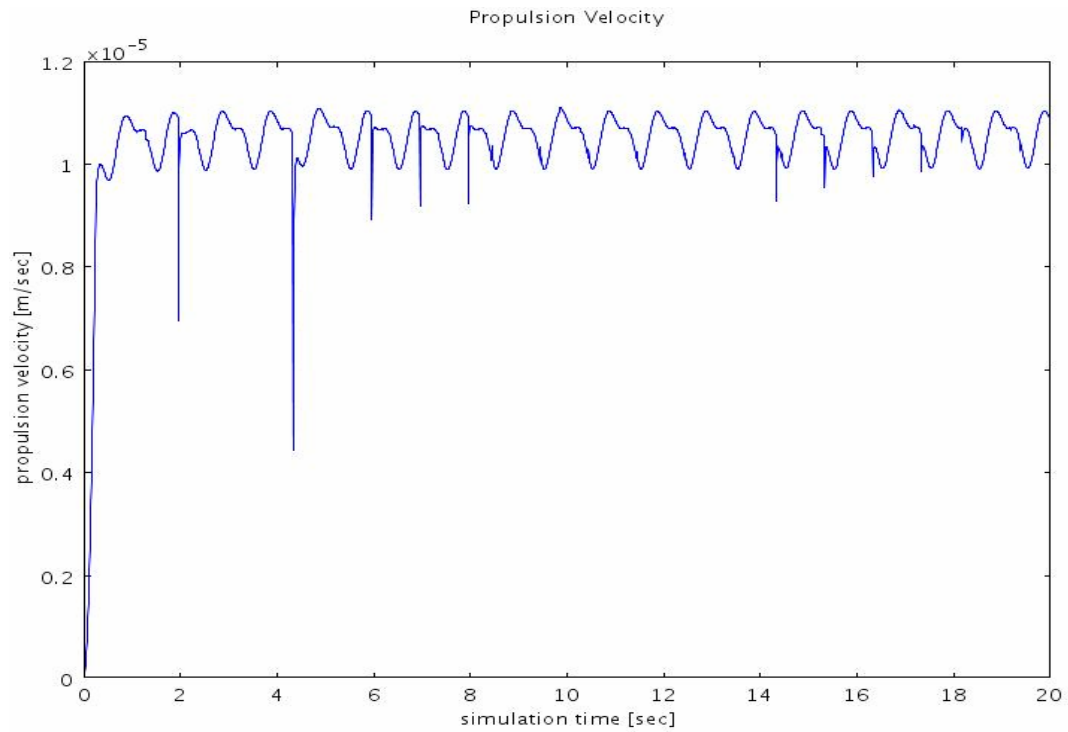
Figure 4.30: 3D Swimmer; propulsion velocity (*X*-velocity) versus simulation time for base case run. Apart from sudden spikes, *X*-velocity becomes steady periodic soon after initial ramp is ended (Base case run.).

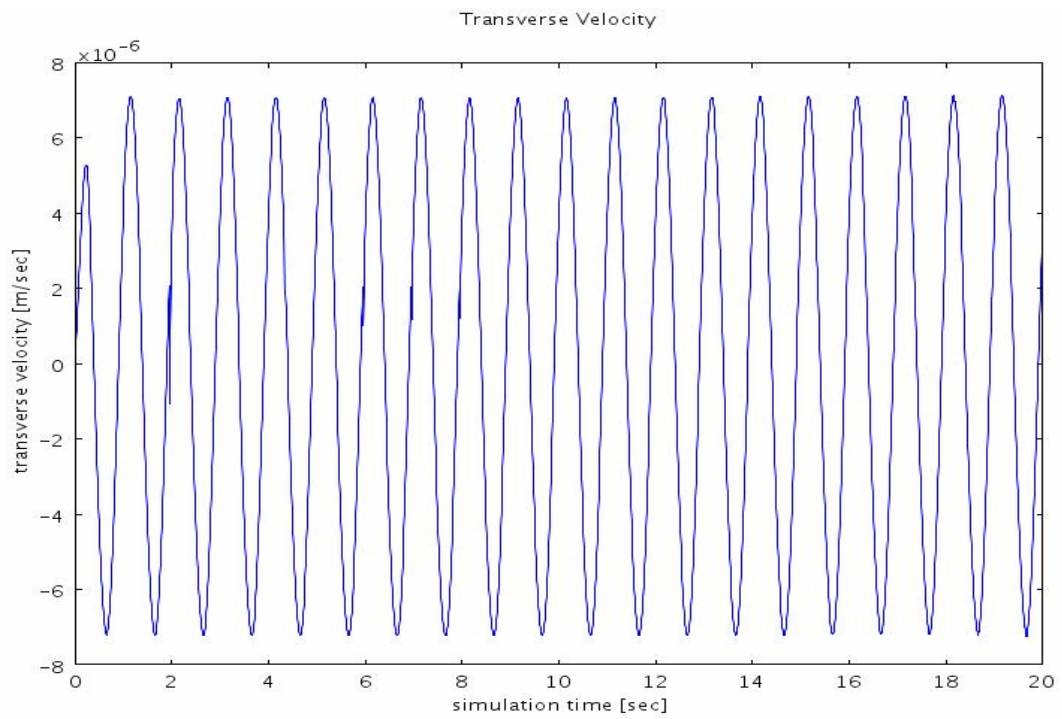Figure 4.31: 3D Swimmer; transverse velocity (*Y*-velocity) versus simulation time for base case run. *Y*-velocity becomes steady periodic after initial ramp is ended.
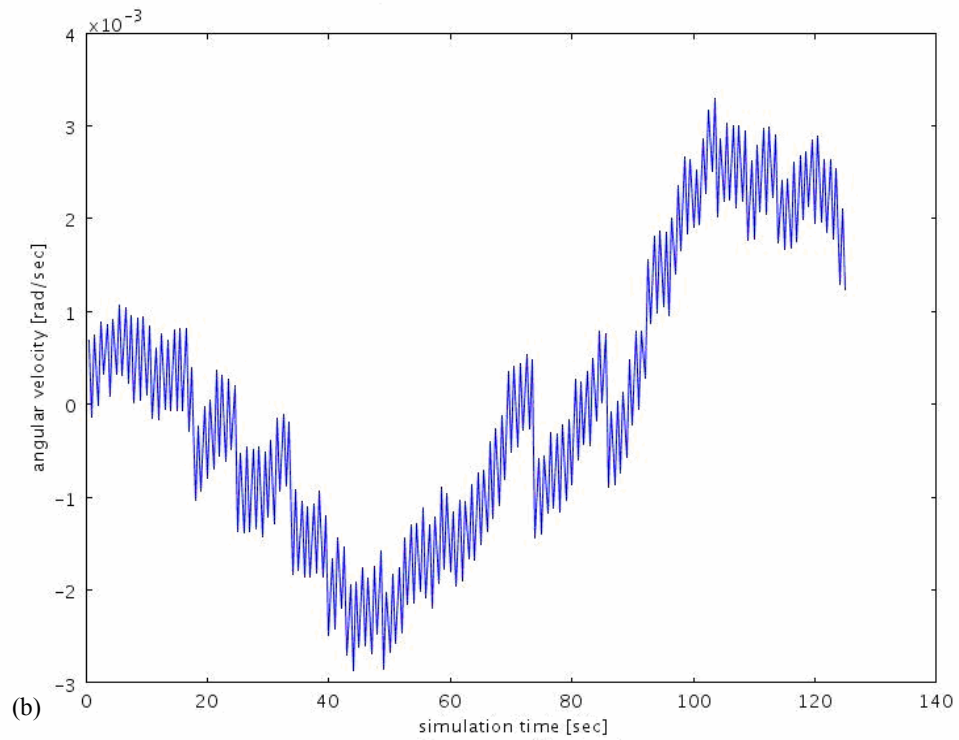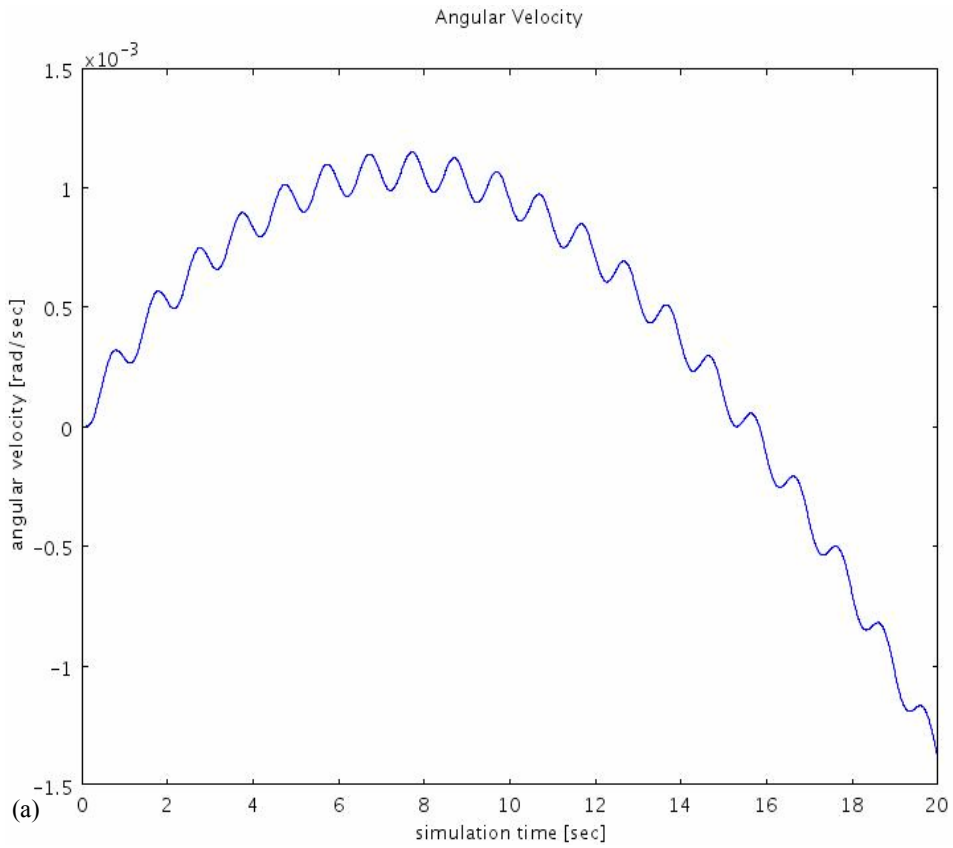
Figure 4.32: 3D Swimmer; (a) angular velocity with respect to center of mass versus simulation time for base case run. (High resolution plot), (b) Angular velocity has secondary frequency effects with longer period (Base case run).

91

While propulsion is commencing, swimmer's center of mass has three degrees of freedom, translation in both *X* and *Y*-directions and rotation around *Z*-axis. Net motion takes place in *X*-direction as shown in Figure 4.30 since *Y*-translation and *Z*-rotation happen in a sinusoidal behavior around zero as portrayed in Figures 4.31 and 4.32-(b) except *X*-velocity (propulsion velocity). Angular velocity has secondary frequency effects embedded within itself as can be seen in Figure 4.32.

4.2.2 Parametric Study: Time averaged results

In this part, numerical results for the parametric study carried out will be represented respectively for parameterized design variables, namely $\{B_o, \lambda, f, C_{sh}\}$, via time averaged results. The disadvantage of dimensional analysis is that although general behavior is the same for proposed geometry and wave actuation, numeric results are unique for predefined design specifications.

4.2.2.1 Amplitude Effect

Following results are obtained for base case values of $\lambda = 625$ μm, $f = 1$ Hz and $C_{sh} = 6$ and varying amplitudes with the constants represented in Table 3.5. Figure 4.33 shows the relationship between wave amplitude and propulsion velocity. Presented curve exhibits almost a quadratic relationship similar to the asymptotic results given by Taylor (1981) and Katz (1974), except for the geometrical constants or higher order effects. As amplitude increases propulsion velocity increases with the square of the rate of change in amplitude. This behavior is limited by the deflection capacity of the structure to form the tail which will be partially discussed in following sections.

Figure 4.34 demonstrates the effect of wave amplitude on power requirement to support the desired waving affect. Again the dimensional numerical results of swimmer behavior for power consumption agree with the asymptotic results presented by Sir Taylor (1981); i.e. power need to gain desired waving action is proportional to the square of the change in wave amplitude.
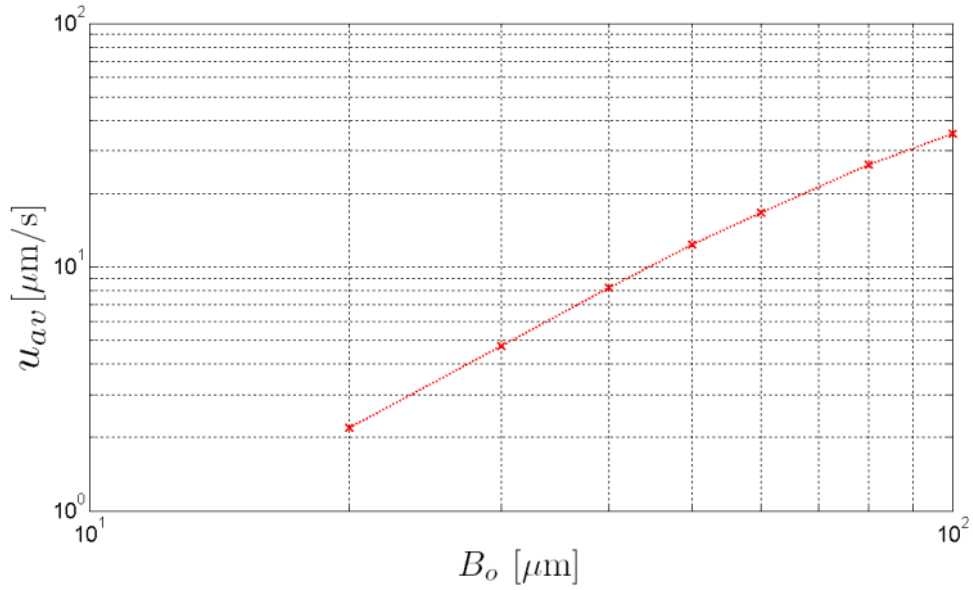
Figure 4.33: 3D Swimmer; wave amplitude vs. Propulsion velocity for $\lambda = 625$ μm, $f = 1$ Hz and $C_{sh} = 6$.
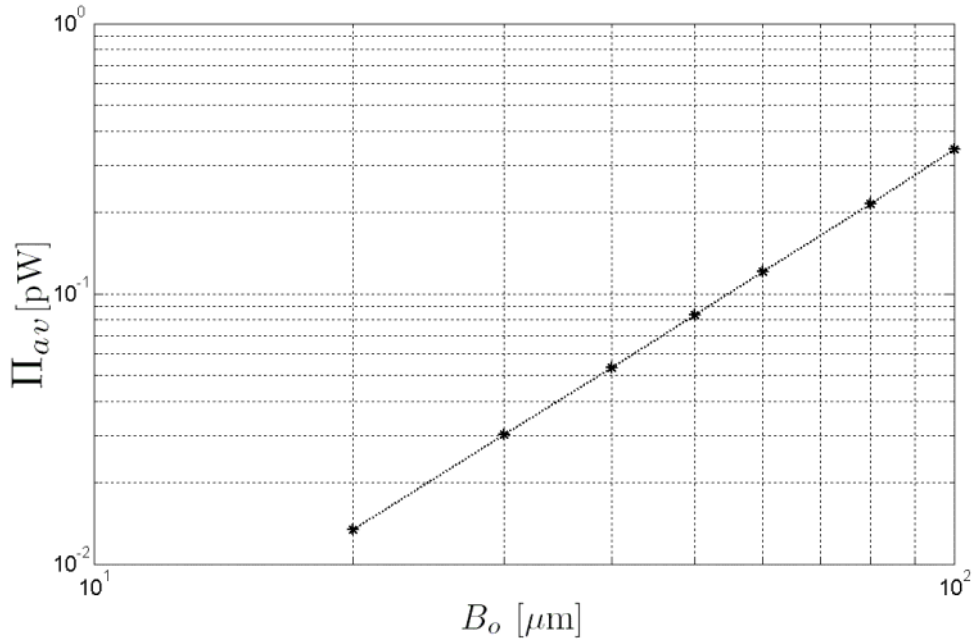
Figure 4.34: 3D Swimmer; wave amplitude vs. power consumption for $\lambda = 625$ μm, $f = 1$ Hz and $C_{sh} = 6$.

Figure 4.35 shows the effect of wave amplitude on swimming efficiency of the proposed system, which is calculated as the percentage ratio of power to overcome the shear forces on X-axis to the power to sustain desired waving action on the tail neglecting structural or electrical conversions. Swimming efficiency also changes proportional almost with square of the change in wave amplitude as depicted in Figure

4.35. It can be seen that for $B_o = 100$ μm efficiency gets close to %0.5 for the particular case.

Figure 4.35: 3D Swimmer, wave amplitude vs. swimmer efficiency for $\lambda = 625$ μm, $f = 1$ Hz and $C_{sh} = 6$.

4.2.2.2 Wavelength Effect
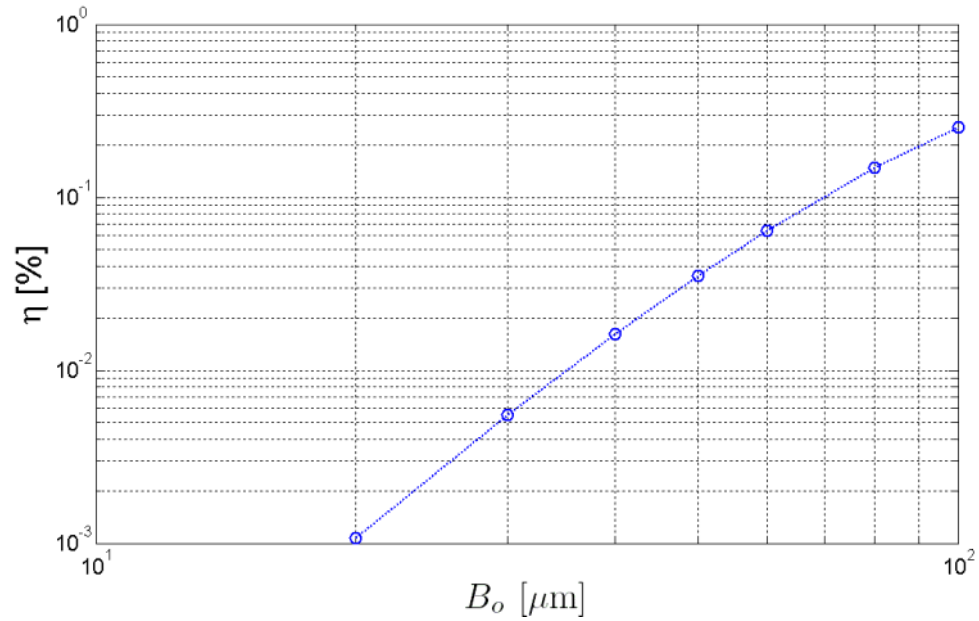
Following results are obtained for base case values of $B_o = 45.625$ μm, $f = 1$ Hz and $C_{sh} = 6$ with varying wavelengths. Figure 4.36 represents the impact of wavelength on propulsion velocity. Propulsion velocity changes linearly proportional to the change in the wavelength just as Katz (1974) suggested but numerical results show that the swimmer behavior does not include an inversely proportional behavior for small wavelengths as Sir Taylor (1951) predicted.

Figure 4.37 illustrates the impact of wavelength on power required to sustain desired waving action on the tail. Numerical results show that power consumption changes almost proportional to the 1.5[th] power of the wavelength change but definitely not liner which is clearly not in agreement with results published by either Sir Taylor (1951) or Katz (1974) and Childress (1981). Possible grounds for this nonlinear effect will be discussed in following sections.

Figure 4.36: 3D Swimmer; ratio of wavelength to tail length vs. swimmer velocity for $B_o = 45.625$ μm, $f = 1$ Hz and $C_{sh} = 6$.
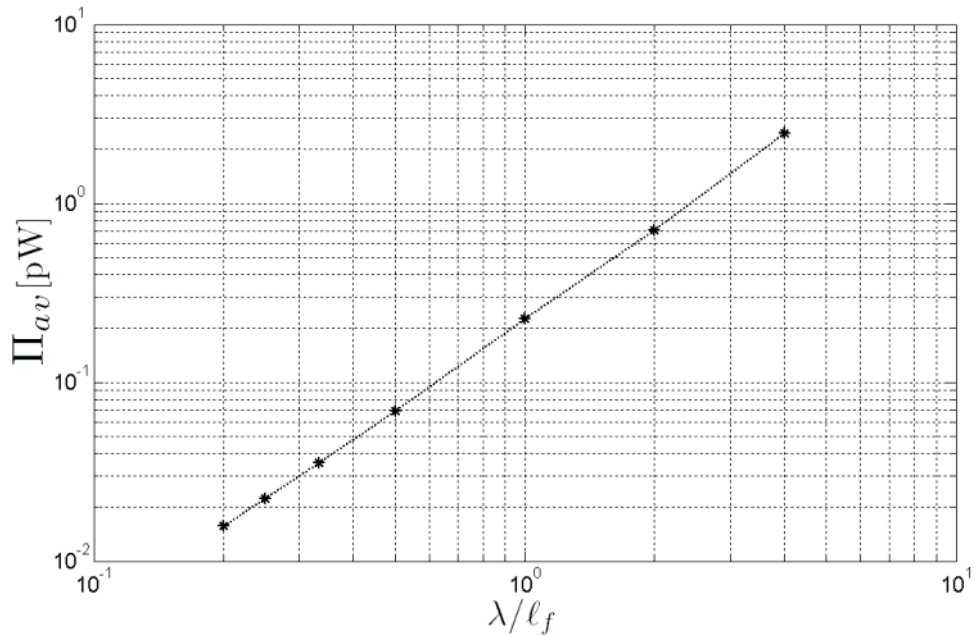
Figure 4.37: 3D Swimmer; ratio of wavelength to tail length vs. power consumption for $B_o = 45.625$ μm, $f = 1$ Hz and $C_{sh} = 6$.

Figure 4.38 shows that there is a minimum possible efficiency which occurs when wavelength is equal to the half tail length. As wavelength goes to zero efficiency seems to increase as it does while the ratio gets larger but each direction change happens in small amounts hence the curve is like a very shallow valley shape. These results show

that there is a trade-off between optimum efficiency and high velocities. As can be monitored from Figures 4.36-4.38, it is possible to conclude that for high efficiency and low power consumption, wavelength choice should be within $0 \ll \lambda/\ell_f < 0.5$ for considerable velocities.
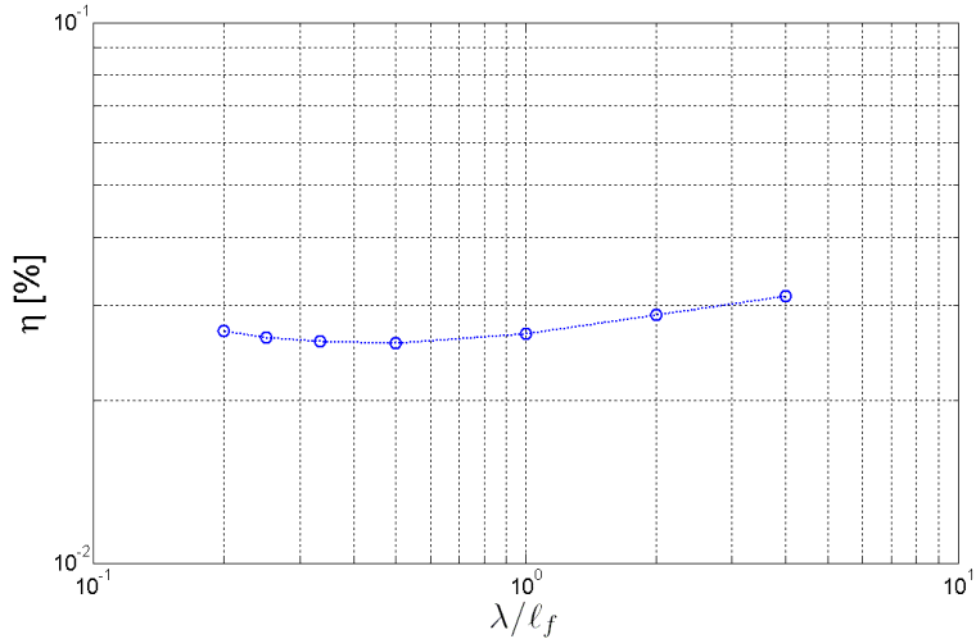
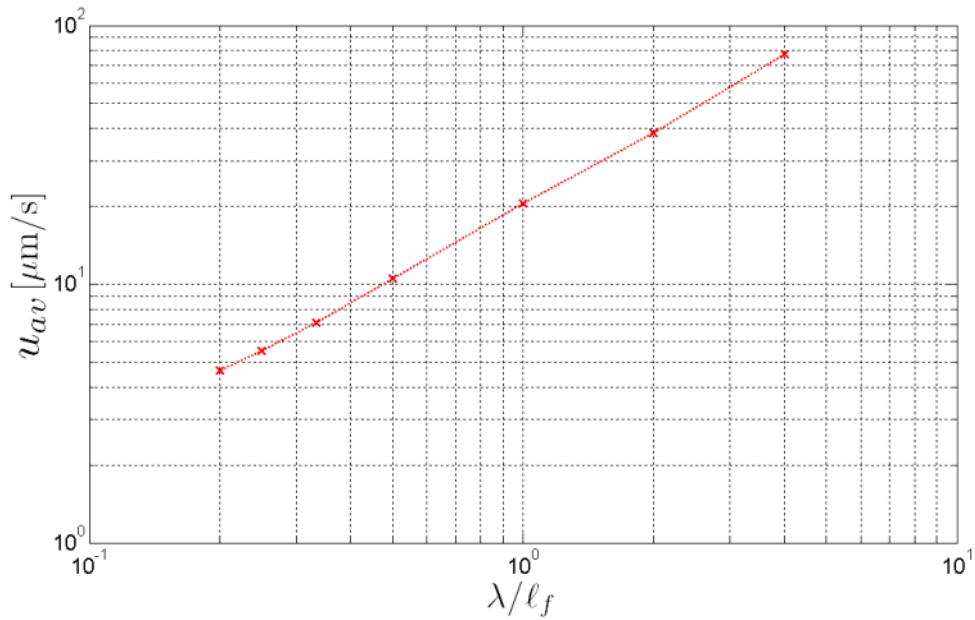

Figure 4.38: 3D Swimmer; ratio of wavelength to tail length vs. swimmer efficiency for $B_o = 45.625$ μm, $f = 1$ Hz and $C_{sh} = 6$. Notice that the minimum efficiency takes place where wavelength is equal to half tail length.

4.2.2.3 Driving Frequency Effect

Following results are obtained for base case values of $\lambda = 625$ μm, $B_o = 45.625$ μm, $C_{sh} = 6$ with variable driving frequencies. Figure 4.39 represents the impact of driving frequency on propulsion velocity. The change in propulsion velocity is linearly proportional to the rate of change in the driving frequency as Katz (1974) suggested.

Figure 4.40 demonstrates the effect of frequency on power consumption. As it can be observed power consumption increases with a ratio proportional to square of the change of frequency which is completely concur with the results given by Taylor (1951) and Katz (1974).
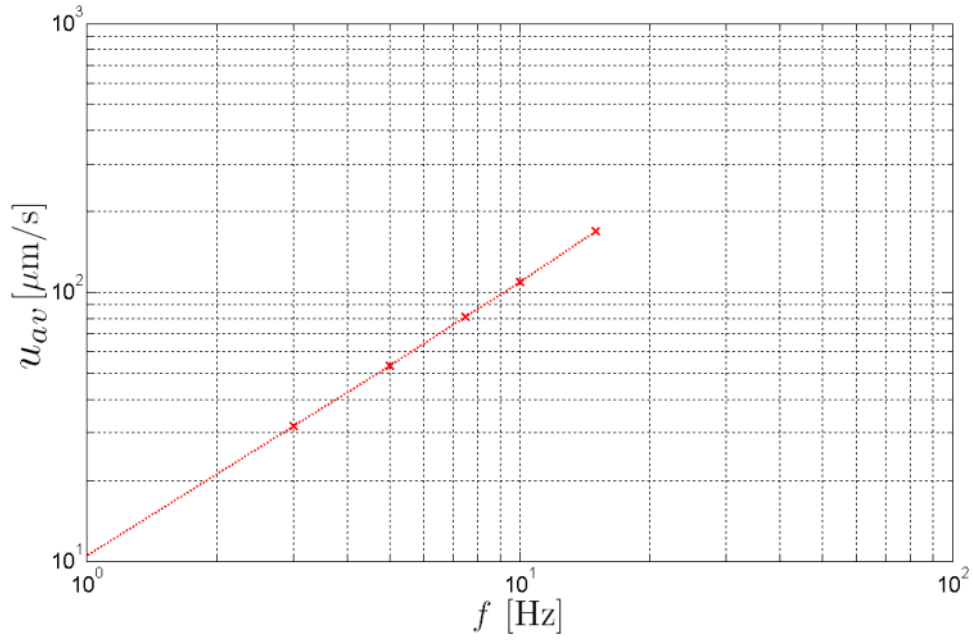
Figure 4.39: 3D Swimmer; driving frequency vs. propulsion velocity for $\lambda = 625$ μm, $B_o = 45.625$ μm and $C_{sh} = 6$.

Figure 4.40: 3D Swimmer, driving frequency vs. power consumption for $\lambda = 625$ μm, $B_o = 45.625$ μm and $C_{sh} = 6$.

Figure 4.41 demonstrates the characteristic behavior of efficiency with respect to driving frequency. As observed before, frequency almost does not change efficiency of the swimmer (or the waving membrane).

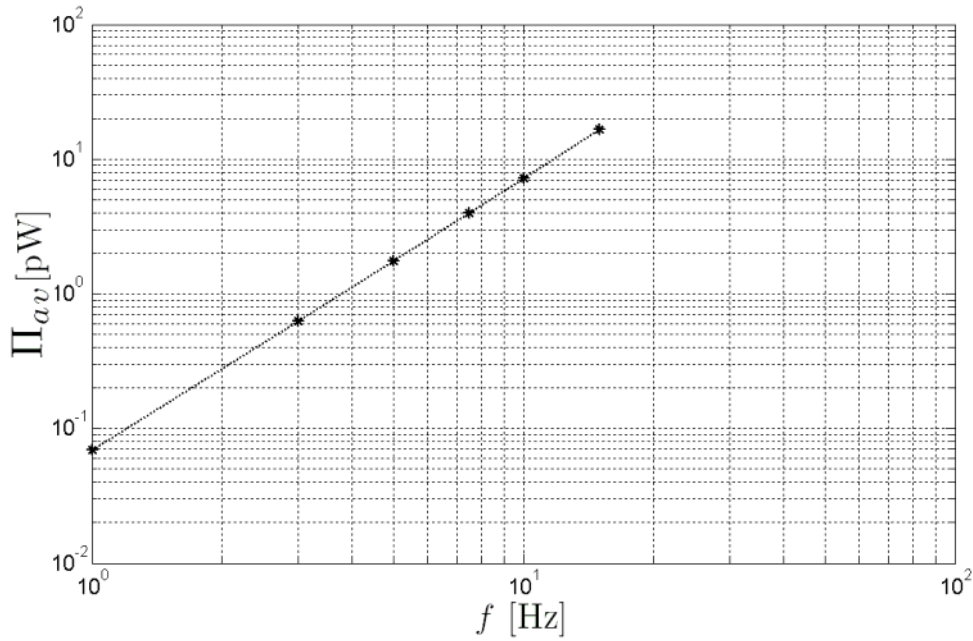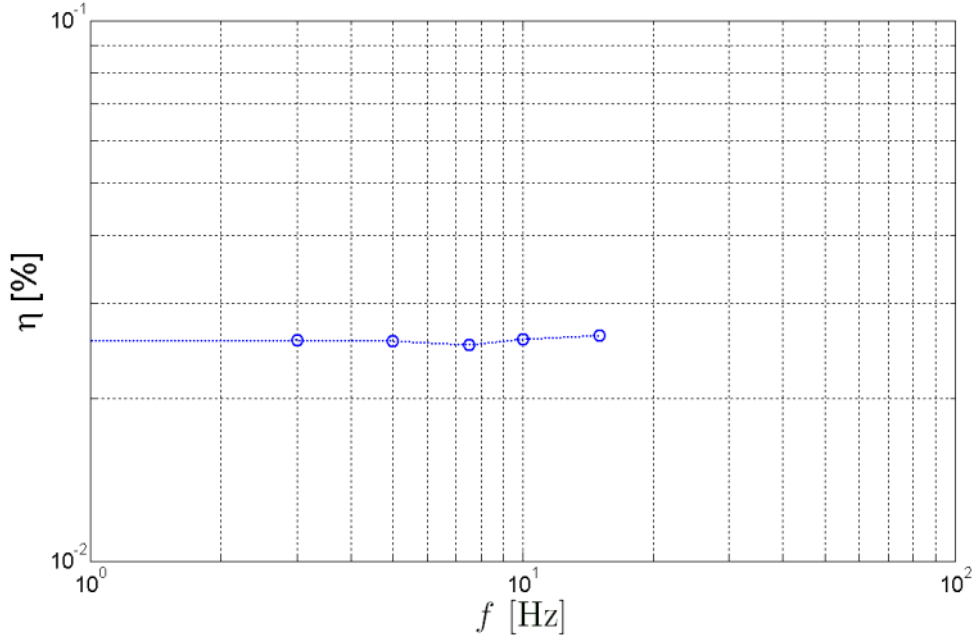Figure 4.41: 3D Swimmer; driving frequency vs. swimmer efficiency for $\lambda = 625$ μm, $B_o = 45.625$ μm and $C_{sh} = 6$.

4.2.2.4 Shape Constant Effect

Following results are obtained for base case values of $\lambda = 625$ μm, $B_o = 45.625$ μm, $f = 1$ Hz with variable shape constants. Shape constant, C_{sh}, is the constant to determine what portion of the tail will achieve maximum amplitude during waving action by modifying the behavior of envelope function (3.48). Figure 4.42 represents the role of shape constant on propulsion velocity. Like one may predict, as shape constant gets larger, propulsion velocity reaches to an asymptotical value for after a certain value it has no effect since whole tail achieves the maximum amplitude value.

Figure 4.43 expresses the behavior for the relationship between shape constant and hydraulic power consumption. When $C_{sh} = 4$, maximum amplitude occurs on the tip with approximately more than %95 of the real maximum. The maximum power consumption takes place where $C_{sh} = 10$ as observed in Figure 4.43. Velocity profile changes its slope after $C_{sh} = 4$ such that relatively fast incline turns into a slow approach to the asymptotical value, i.e. for $C_{sh} > 4$ sinusoidal wave propagation tends to get more homogeneous throughout the waving tail. Thus same homogeneous effort causes relatively less power consumption per wave against the fluid resistance since whole boundary starts to force the surrounding fluid with the same stroke without letting fluid loose its energy by means of shear losses and stand down.

Figure 4.44 shows the effect of shape constant on swimmer efficiency. As shape constant approaches to C_{sh} = 10, efficiency increases approaching a limit value eventually. As expected, after tail assumes the maximum amplitude value from start to end and as expected efficiency is does not change anymore. Nevertheless, this is indeed the ideal case, the waving action is never supposed to be totally homogeneous throughout the tail since one end is always fixed.
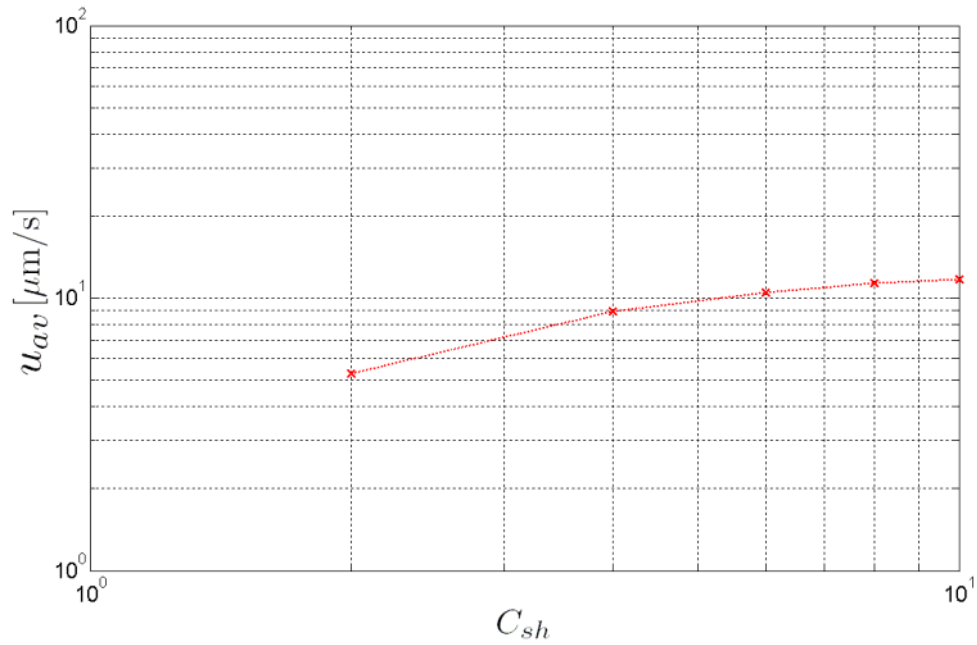
Figure 4.42: 3D Swimmer; shape constant vs. swimmer velocity for λ = 625 μm, B_o = 45.625 μm and f = 1 Hz.
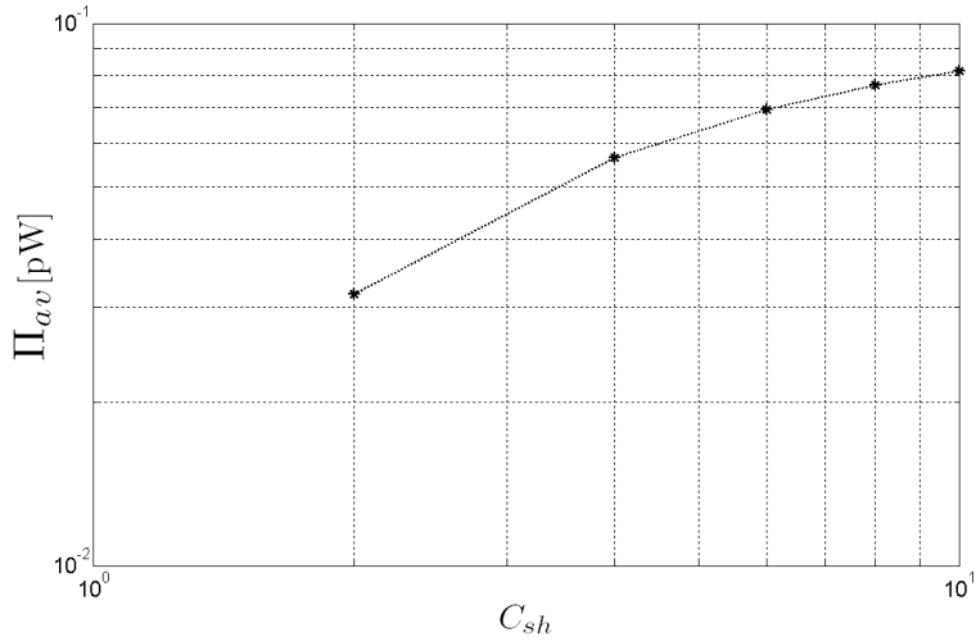
Figure 4.43: 3D Swimmer; shape constant vs. power consumption for $\lambda = 625$ μm, $B_{\mathrm{o}} = 45.625$ μm and $f = 1$ Hz.
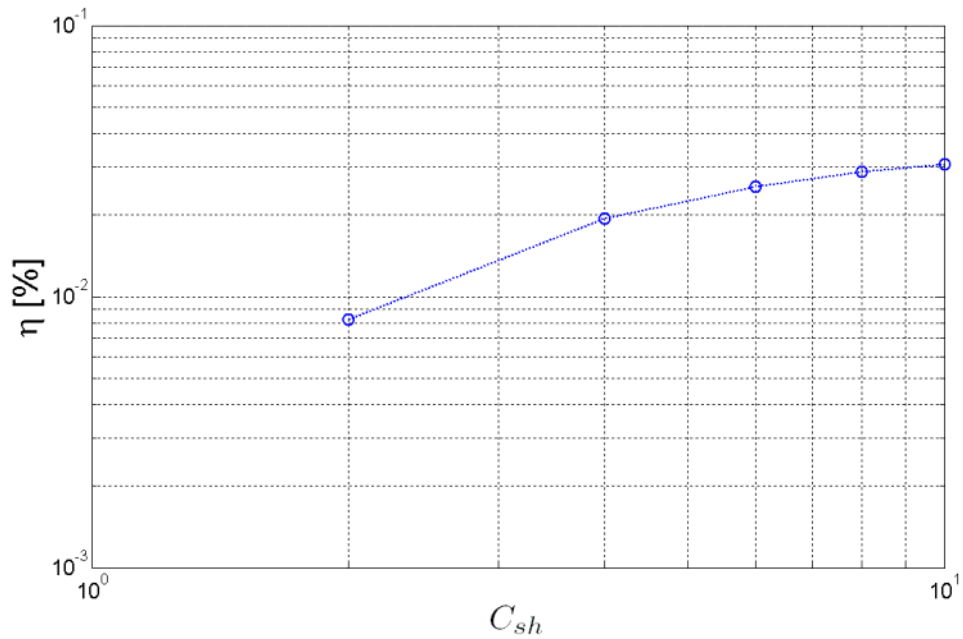
Figure 4.44: 3D Swimmer; shape constant vs. swimmer efficiency for $\lambda = 625$ μm, $B_{\mathrm{o}} = 45.625$ μm and $f = 1$ Hz.

4.2.3 Revisiting the Extensibility Approach

It is obvious that inextensibility approach does not hold for large amplitudes. In reality inextensibility is only possible if surface acoustic waves are invoked in shear

mode [28]. Childress (1981) has discussed a set of prerequisites for inextensibility approach and concluded that combination of *X* and *Y*-motions of the waving membrane results in even more than 40% higher propulsion velocities without disturbing system behavior under design parameters [66]. Combining these two facts results in the issue on the maximum *X*-velocity of any arbitrary point located on the tail. That is to say, if any arbitrary point has a larger *X*-velocity with respect to center of mass of the swimmer than the velocity of the center of mass with respect to a stationary eye in *XYZ* frame then the dominant inextensibility approach does not hold anymore because of the inevitable effect of no-slip conditions. In this case, simulation results become questionable because in real life, no-slip conditions would make sure that the contribution occurs as Childress (1981) states. To find out the limits on this issue, maximum velocities were tested under extensibility assumption.

The proper approach to calculate the maximum *X*-velocity on the tail for any set of design parameters is to integrate the local contributions of each point in a cumulative approach. Derivation of $Y_f(X_f,t,)$ with respect to *X*-axis would yield slope of the tangent line at that point, i.e. $dY/dX=\tan(\Theta)$. But for small deflections it is safe to say that dX is also equal to $d\ell_f$, the infinitesimal portion of the tail, and this results in equating $\tan(\Theta)$ expression to $\sin(\Theta)$. This results in $dX = d\ell_f - \cos(\arcsin(dY/dX))\ d\ell_f$ thus leading to (4.20):

$$\frac{dX}{dt} = \frac{d\ell_f - \cos\left(\arcsin\left(\frac{dY}{dX}\right)\right)d\ell_f}{dt} \tag{4.20}$$

The expression above (4.20) needs to be integrated over the tail, i.e. from 0 to ℓ_f with the transformation of $d\ell_f = dX_f$ on the right hand side, in order to find the velocity data of each point on the tail. Since MATLAB[®] has the ability to integrate both symbolic and numeric expressions so it was preferred to integrate (4.20) invoking the trapezoidal rule [101] function, i.e. "trapz" [102], to obtain the numerical results depicted in Figures 4.45, 4.46, 4.47 and 4.48. By sweeping a full simulation period for base case parameters changing in turn, all maximum values are obtained for this simulation batch.

Figure 4.45 shows the maximum *X*-velocity on tail inspected for validation to amplitude runs, which is almost 20 times smaller than the velocity of center of mass with respect to the stationary frame.

Figure 4.46 shows the maximum *X*-velocity on tail inspected for frequency run check, which is again almost 20 times smaller than the velocity of center of mass.

Figure 4.47 illustrates a different behavior, i.e. as wavelength increases, the maximum velocity decreases and *vice versa*. For small wavelength values the center of mass velocity and the maximum tail velocity is comparable and very close to each other. For large wavelength values velocity of center of mass is more than 150 times larger in magnitude. There is an inflection point where $\ell_f / \lambda = 1$.

Finally, Figure 4.48 demonstrates the C_{sh} effect on maximum *X*-velocity which is ten times smaller for its highest value on tail surface. Hence all simulations except for smallest wavelength value are conveniently checked out for inextensibility condition.
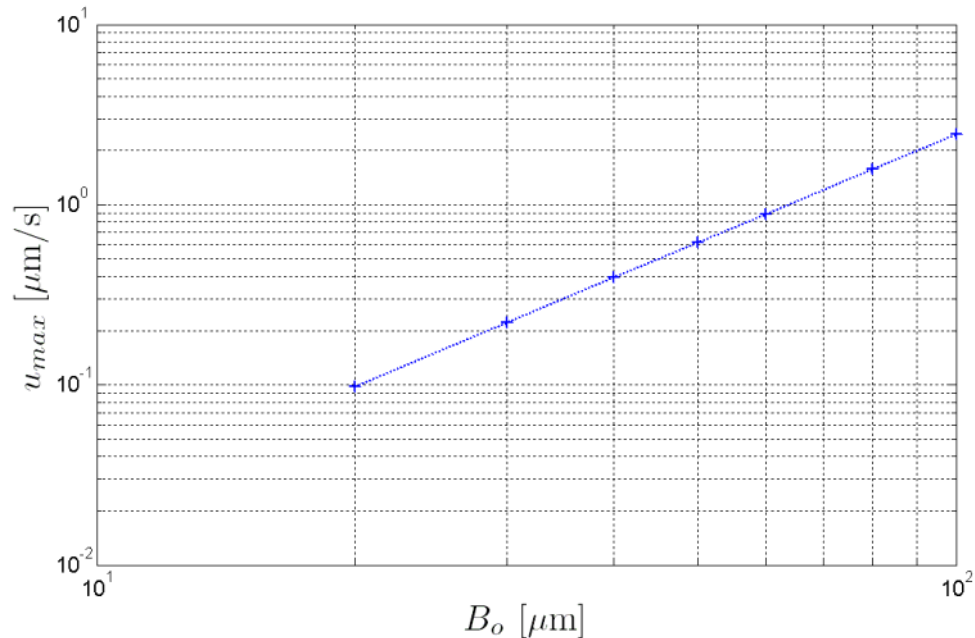
Figure 4.45: Extensibility; maximum *X*-velocity on tail with respect to center of mass for $\lambda = 625$ μm, $f = 1$ Hz and $C_{sh} = 6$ with one complete simulation period with varying B_o.
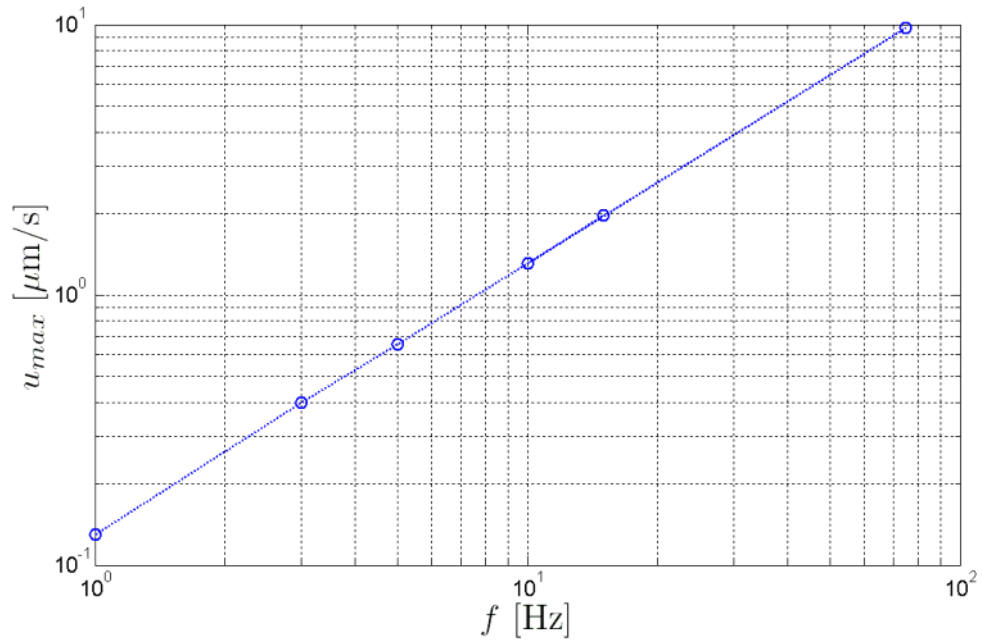
Figure 4.46: Extensibility; maximum *X*-velocity on tail with respect to center of mass for $\lambda = 625$ μm, $B_o = 45.625$ μm and $C_{sh} = 6$ with one complete simulation period and varying f.
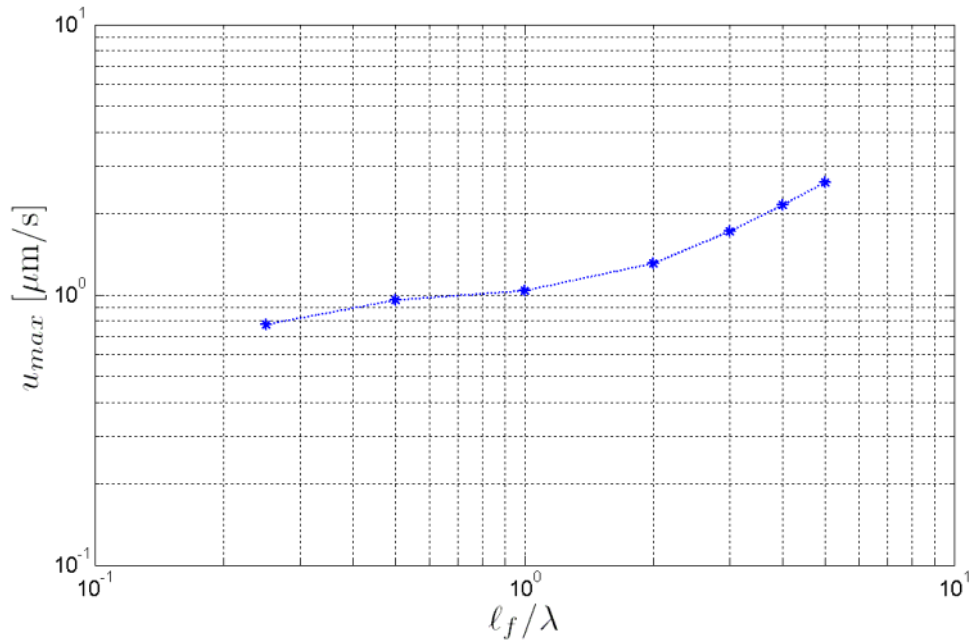
Figure 4.47: Extensibility; maximum *X*-velocity on tail with respect to center of mass for $B_o = 45.625$ μm, $f = 1$ Hz and $C_{sh} = 6$ with one complete simulation period and varying λ.
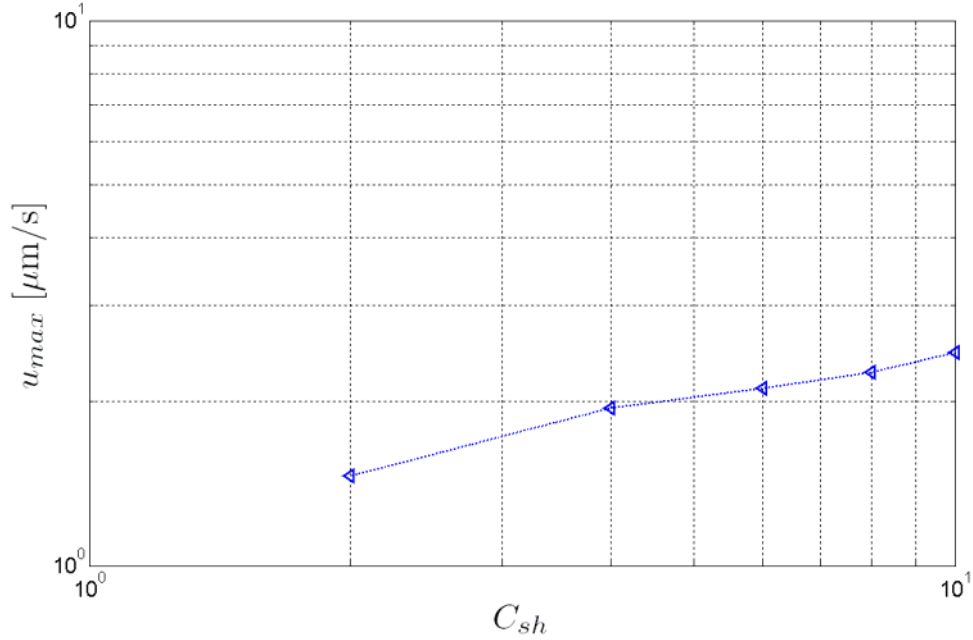
Figure 4.48: Extensibility; maximum *X*-velocity on tail with respect to center of mass for $\lambda = 625$ μm, $B_o = 45.625$ μm and $f = 1$ Hz with one complete simulation period and varying C_{sh}.

4.2.4 Conclusion and Final Remarks on 3D Microswimmer

Both amplitude and driving frequency simulations in 2D and 3D show that contribution to the flow behavior of both pump and swimmer model is the same as Taylor (1951), Katz (1974) and Childress (1981) suggested. Wavelength tends to show a dual behavior encompassing both approaches expressed by Taylor (1951), Katz (1974) for pump simulations.

On the other hand results for swimmer runs show that wavelength effect deserves extra attention. Although 2D and 3D pump simulation results for changing wavelength are in agreement with the asymptotical results found in analytical studies, swimmer results with a rod like tail exhibits an entirely different behavior and deserves a detailed analysis.

One possible explanation may be the aspect ratio between channel and tail geometry which is not an entirely unexpected outcome, since neither Taylor (1951) nor Katz (1974) or Childress (1981) have included W_f/W_{ch} effect in their analysis that proved to be an important parameter in 3D pump results, even if only for geometric reasons. The explanation for this deviation may partially be that each full wave is actually interacting with lateral flows and is responsible for supplying the essential

momentum to mobilize the fluid in the vicinity against this drain effect by sustaining the pre-assumed waving action. Since $W_f/W_{ch} \to 0$, it becomes as if a finite width tail is operating in between relatively infinite stationary plates. Such a configuration drains considerable momentum both in axial and lateral directions as explained in 3D pump case, i.e. as $W_f/W_{ch} \to 0$, not only the power requirement per unit area increases but also behavior, namely slope, changes as seen in Figure 4.25. Hence one may conclude that additional stresses result in behavioral change. That may be the reason why different wavelengths have the same effect on propulsion velocity while power requirement to create propulsion differs, which will be evident towards the end of this discussion.
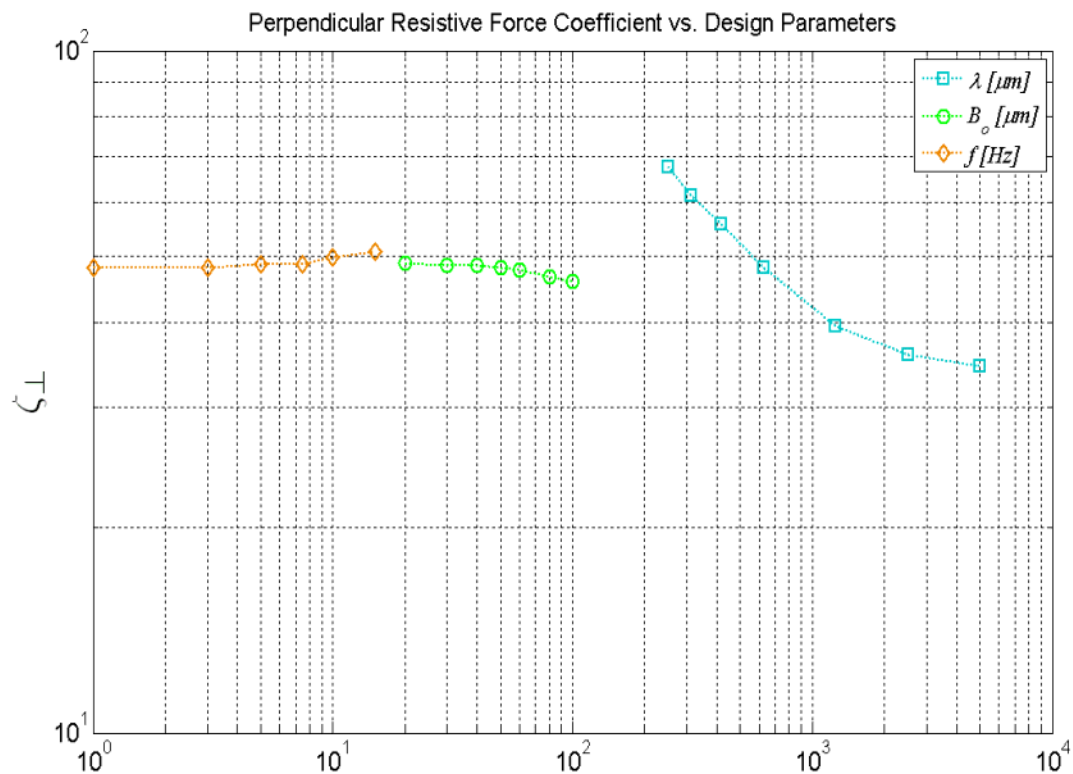
Figure 4.49: Perpendicular resistive force coefficient with respect to λ, B_o, and f. Notice that wavelength is a factor to resistive force coefficient.

Another approach to confirm this peculiar behavior on λ dependence is through the resistive force theory since propulsion velocity is found to be concurrent with asymptotical results found for analytical studies. Resistive force theory states that force on an infinitesimal portion of the structure can be calculated as the product of fluid velocity components and special constants, namely normal or tangential resistive force coefficients in (2.18) and (2.19). As one can observe in Figure 4.49, while wavelength,

λ, is changing, the normal (perpendicular) resistive force coefficient is also changing which suggest that $\zeta_{\perp} \equiv \zeta_{\perp}(\lambda)$, rather than being constant. Amplitude and driving frequency do not seem to have a similar effect on resistive force coefficients but they reveal an almost global constant for proposed design geometry.

Reader should keep in mind that numerical integration procedure is carried out over entire tail surface including both ends. On the other hand, the infinitesimal part depicted in Figure 4.49 and discussed later on is taken from the middle section of the tail where end effects are minimal. This discussion is elaborated on the wavelength, λ, since it has a different consequence on power consumption with higher order effects than the suggested results in previous studies. A sound method to find out the mechanism which led wavelength to have such a consequence on resistive force coefficient is to examine the derivative terms inside the *Y*-component of the full stress tensor shown as (3.79) and (3.96). Figures 4.50-4.54 show the role of each derivative term.
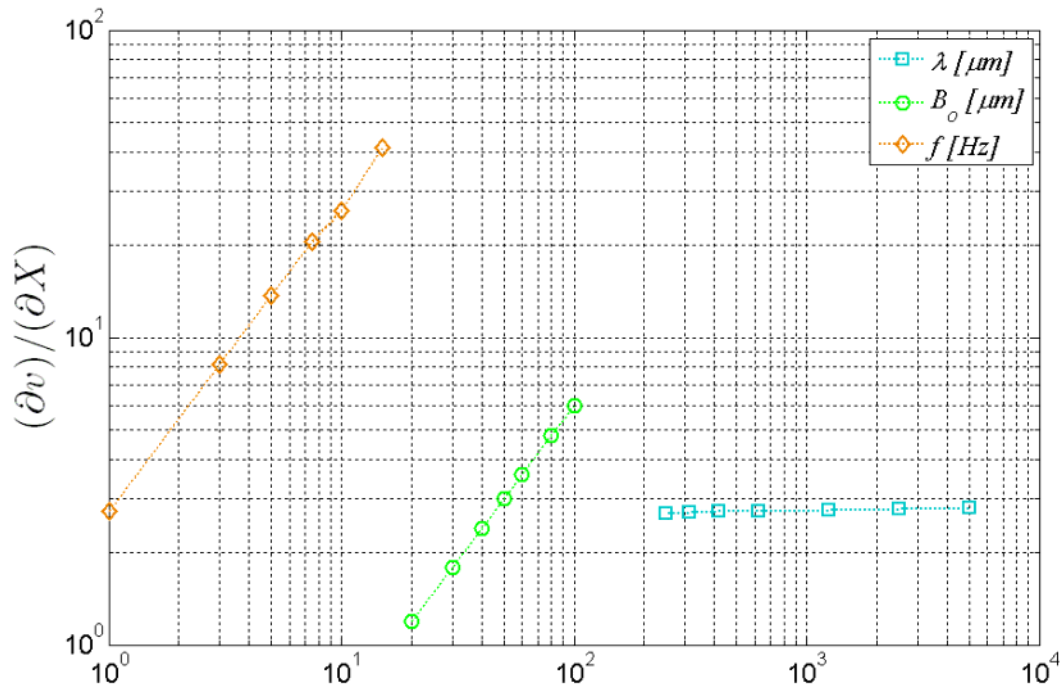
Figure 4.50: Effect of λ, B_o, and f on $\partial v / \partial X$ expression. Notice that λ change does not have any contribution.
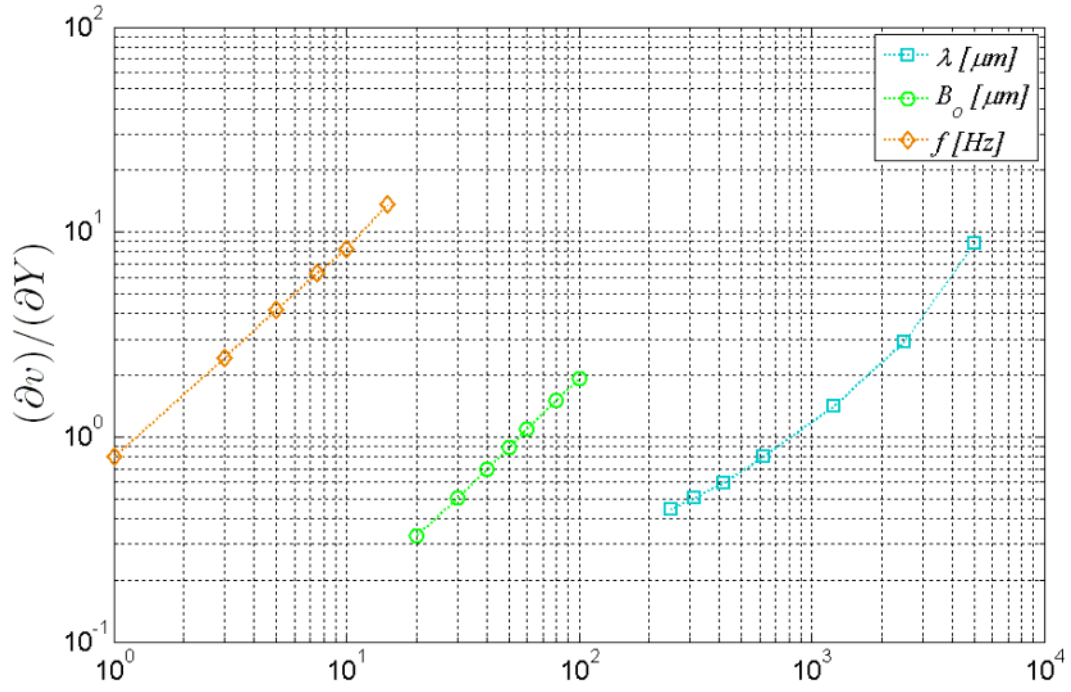
Figure 4.51: Effect of λ, B_o, and f on $\partial v/\partial Y$ expression. Notice that λ and $\partial v/\partial Y$ are almost linearly proportional, with higher order effects.
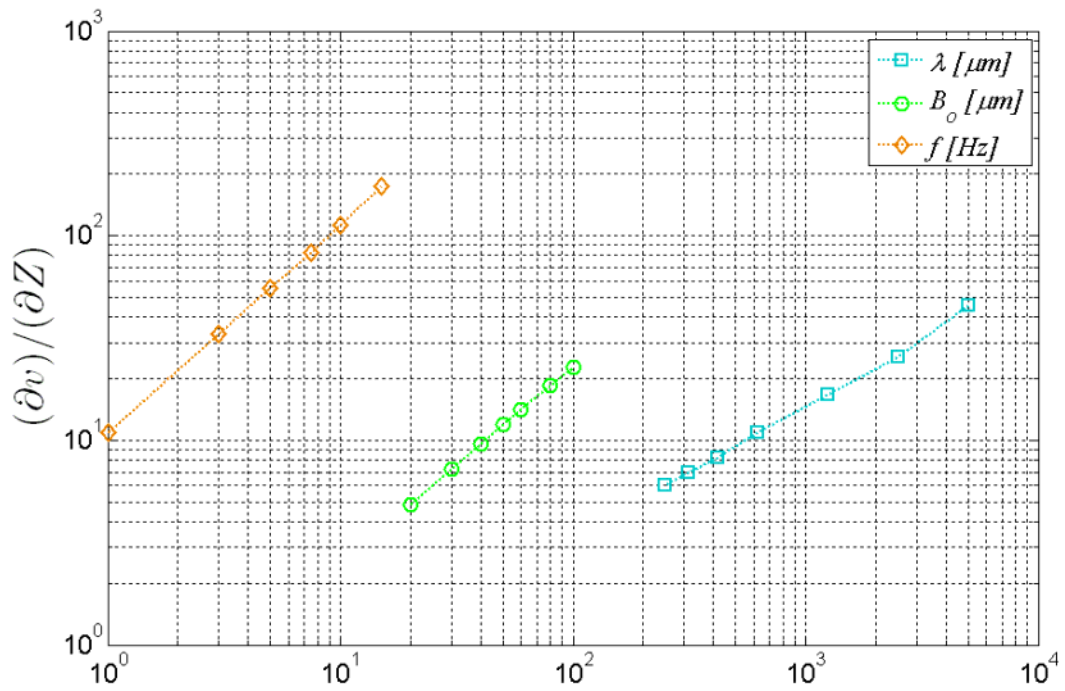
Figure 4.52: Effect of λ, B_o, and f on $\partial v/\partial Z$ expression. Notice that the change in $\partial v/\partial Z$ is 2/3 of the change in λ.
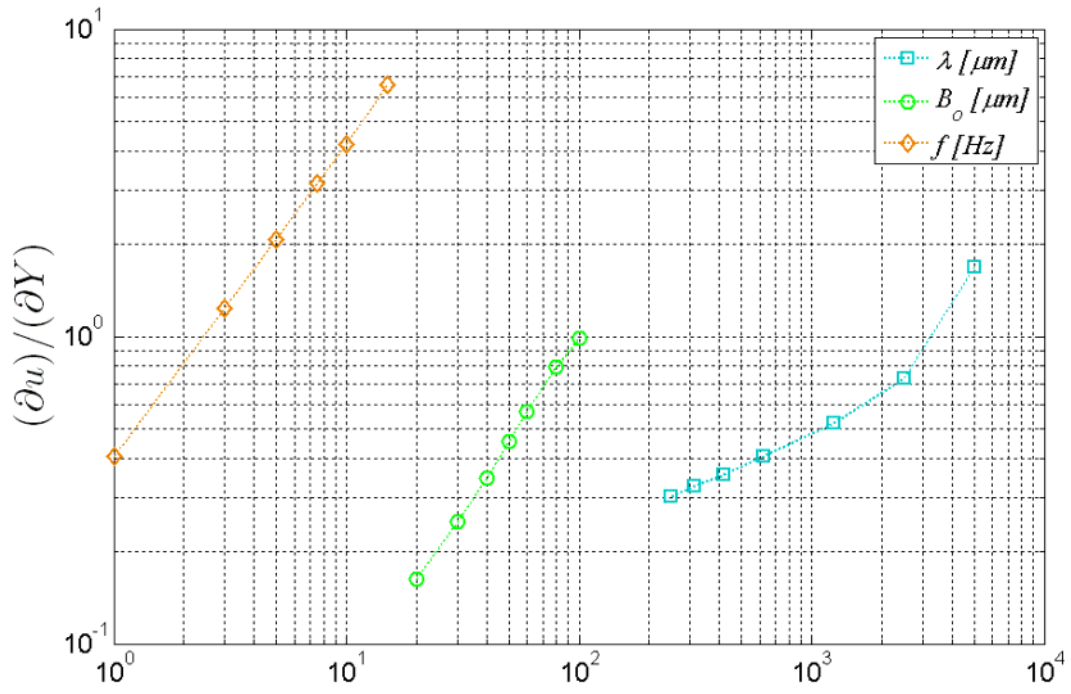
Figure 4.53: Effect of λ, B_o, and f on $\partial u/\partial Y$ expression. Notice that the change in $\partial u/\partial Y$ is 3/4 of the change in λ.
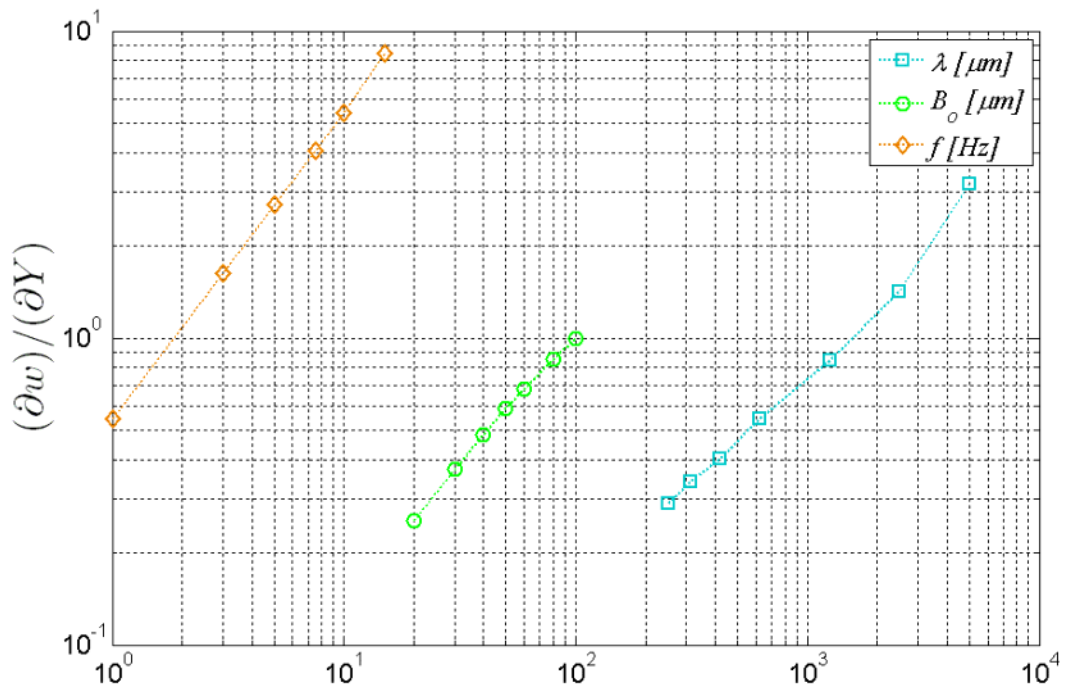
Figure 4.54: Effect of λ, B_o, and f on $\partial w/\partial Y$ expression. Notice that λ and $\partial w/\partial Y$ are almost linearly proportional to each other.

It is evident that the deviation in wavelength behavior relies on the expressions which behave differently, i.e. showing a profile other than linear proportionality with design parameters shown in Figure 4.50, 4.52 and 4.53. Especially X and Z-components of flow variation cause this divergence due to vortex formations. In addition, all these results concur with the conclusion based on Figure 4.55. Y-velocity dependent Y and Z-shear forces exist because of the positive and negative velocity field collusions in the vicinity of the waving tail surfaces as can be examined in a slice plot at the center point of the tail.
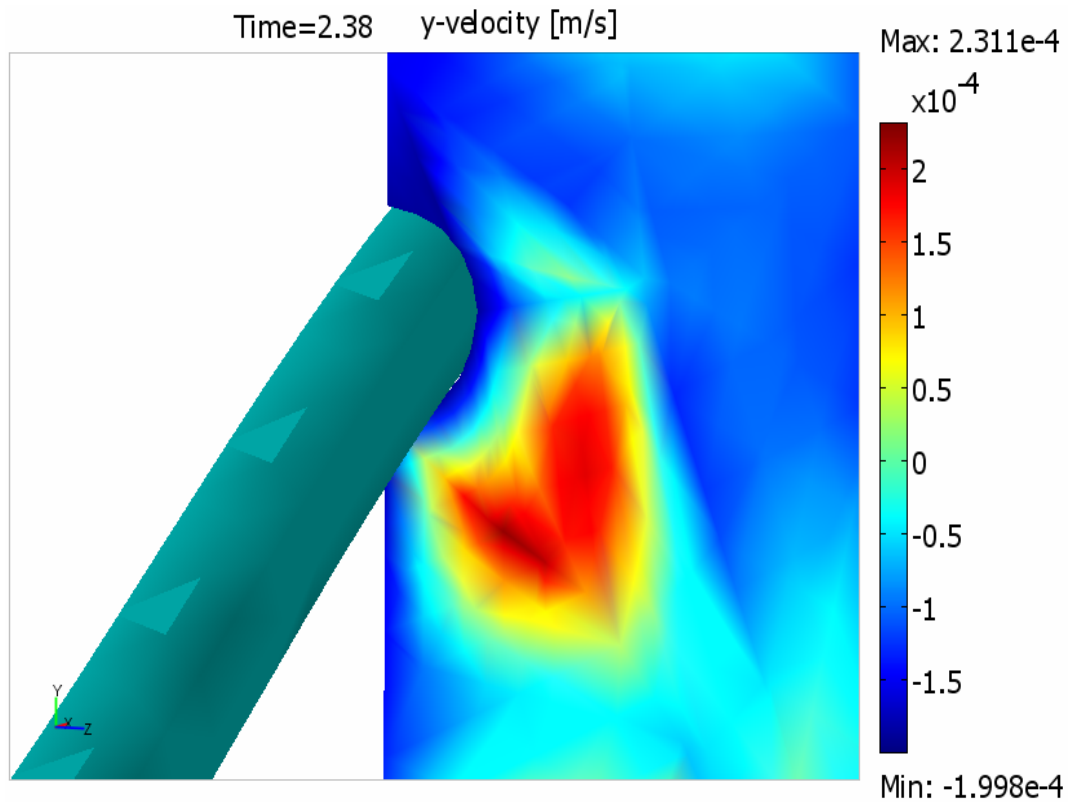
Figure 4.55: Zoomed view on collusion of negative and positive velocity fields in the vicinity of waving tail, at $X = 2.875 \times 10^{-3}$ m and $t = 2.38$ sec. Tail section moves downwards and confronts the positive velocity field on Y and Z-directions created by the previous traveled wave.

Final possible approach is related to the effect of attack angle of the tail surface, i.e. $\tan(\Theta) = 4B\left(X_f, t\right)/\lambda$, on the resistive force, which was discussed as the effect of attack angle on the propulsion velocity [103]. Figure 4.56 illustrates the nonlinear relationship between surface angle and the perpendicular resistive force coefficient versus design parameters, which is obtained purely numerically.
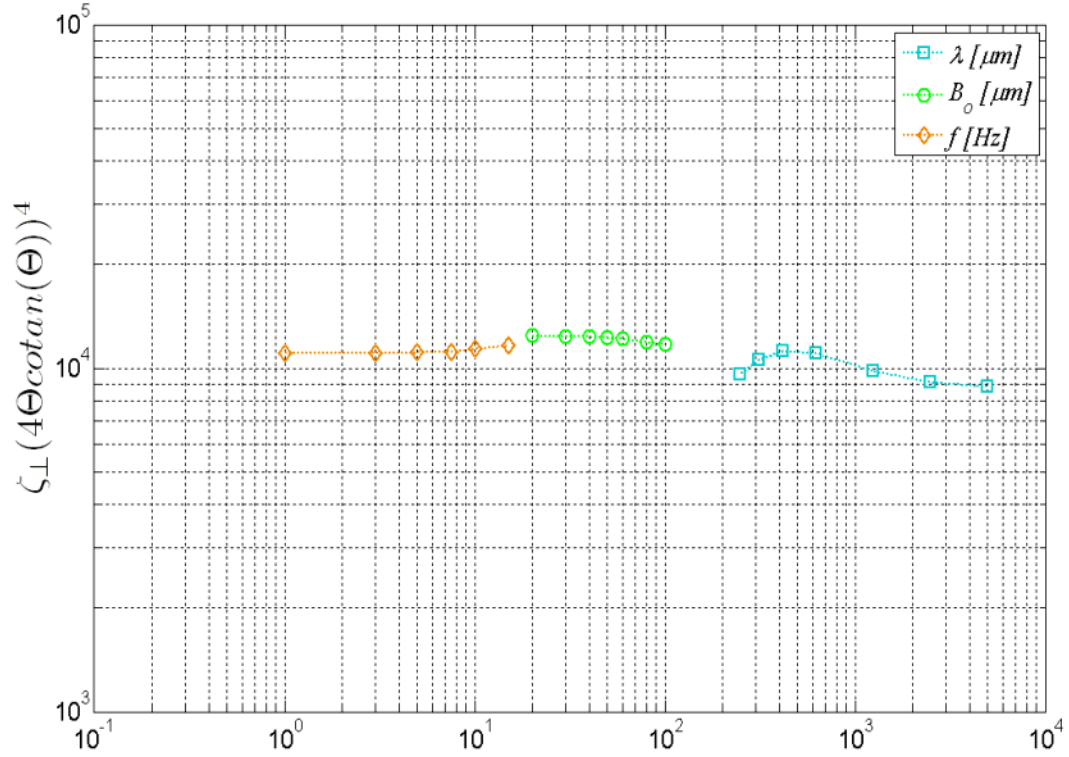
Figure 4.56: Effect of attack angle on resistive force coefficient against design parameters, λ, B_o, and f. Notice that for λ, $\zeta_\perp \left(4\Theta / \tan(\Theta)\right)^4$ has a peak value and still in need of a 'higher order' correction.

Swimmer efficiency values are found to be very small as Lighthill (1975) pointed out, with very high Strouhal number, the dimensionless frequency of the flow, i.e. bigger than 1000, and very low Re numbers, i.e. smaller than 0.01 for most of the cases. These dimensionless number groups shows that either proposed pump design or swimmer design loose excessive energy unlike fish like macroscale natural swimmers [100]; i.e. under these physical conditions vortex structures drains the power exerted into the fluid before it can be converted to net propulsion of the swimmer.

Inextensibility approach does not change the behavior but affects the numerical results as Childress (1981) depicted. The inquiry was to confirm that relative motion on the tail for proposed swimmer does not become a dominant effect on propulsion in real case. It is shown that for most of the cases relative motion is smaller than the swimmer itself including the base case, except for $\lambda = 0.2\ell_f$ (Figures 4.36 and 4.47) where swimmer is still faster but velocities are very close to each other. After all, extensible sheet assumption may affect the efficiency results in either way since it has an influence on both propulsion velocity and power consumption [66].

CHAPTER 5

MICROPROPULSION SYSTEM DESIGN: AN INTRODUCTION

All waving models discussed so far are assumed to be prearranged. In this chapter, it is the intention to carry out a very brief introductory discussion for future work on micropropulsion system design by means of an overview on actuation mechanisms and energy harvesting methods can be employed in MEMS based applications.

5.1 Creating Wave Deformations

Waving geometry and properties were given as design parameters in analytical and numeric studies presented earlier in this text. This section is dedicated to review possible alternative ways to create propagating waving action on structures. Waving action without any rotating or mechanically independent moving parts is possible via deformable structures which act as electrical to mechanical transducers, and *vice versa*. In this section, two material types, namely piezoelectric materials and ionic polymer-metal composites (IPMC) will be reviewed for wave traveling purposes.

5.1.1 Piezo Materials

Piezo is a word descended from Greek connotation "to squeeze" [104]. Piezo materials can be ceramic, polymer or in composite form [105], [106]. Piezo materials have a considerable value since their electrical-mechanical-electrical transformation feature represents practical solutions in several micro applications, especially for micro sensors [21] and micropump systems as portrayed in previous chapters. This advantage is known to be due to the "inversion-asymmetry" which is a consequence of asymmetric crystalline structure [75]. Nevertheless, this feature is not always inherited; generally

ferroelectric materials are manufactured via a procedure known as "poling" to include this quality [12]. Whenever unevenly charged molecules are displaced inside the structure with an external load an electric field is created and whenever an external electric field is applied on the piezo material it results in net displacement of charged particles [75]. All these interactions can be modeled with two very compact matrix equations, one for transversely polarized piezomaterials (5.1) and other for axially polarized piezomaterials (5.2) [18] as:

$$
\begin{bmatrix} \sigma_{xx} \\ \sigma_{yy} \\ \sigma_{zz} \\ 2\tau_{yz} \\ 2\tau_{xz} \\ 2\tau_{xy} \\ D_{xx} \\ D_{yy} \\ D_{zz} \end{bmatrix} = \begin{bmatrix} s_{11} & s_{12} & s_{13} & 0 & 0 & 0 & 0 & 0 & -d_{31} \\ s_{12} & s_{22} & s_{23} & 0 & 0 & 0 & 0 & 0 & -d_{32} \\ s_{13} & s_{23} & s_{33} & 0 & 0 & 0 & 0 & 0 & -d_{33} \\ 0 & 0 & 0 & s_{44} & 0 & 0 & 0 & -d_{24} & 0 \\ 0 & 0 & 0 & 0 & s_{55} & 0 & -d_{15} & 0 & 0 \\ 0 & 0 & 0 & 0 & 0 & s_{66} & 0 & 0 & 0 \\ 0 & 0 & 0 & 0 & d_{15} & 0 & \in_{xx} & 0 & 0 \\ 0 & 0 & 0 & d_{24} & 0 & 0 & 0 & \in_{yy} & 0 \\ d_{31} & d_{32} & d_{33} & 0 & 0 & 0 & 0 & 0 & \in_{zz} \end{bmatrix} \cdot \begin{bmatrix} \varepsilon_{xx} \\ \varepsilon_{yy} \\ \varepsilon_{zz} \\ \gamma_{yz} \\ \gamma_{xz} \\ \gamma_{xy} \\ E_{xx} \\ E_{yy} \\ E_{zz} \end{bmatrix} \qquad (5.1)
$$

$$
\begin{bmatrix} \sigma_{xx} \\ \sigma_{yy} \\ \sigma_{zz} \\ 2\tau_{yz} \\ 2\tau_{xz} \\ 2\tau_{xy} \\ D_{xx} \\ D_{yy} \\ D_{zz} \end{bmatrix} = \begin{bmatrix} s_{33} & s_{23} & s_{13} & 0 & 0 & 0 & -d_{33} & 0 & 0 \\ s_{23} & s_{22} & s_{12} & 0 & 0 & 0 & -d_{32} & 0 & 0 \\ s_{13} & s_{12} & s_{11} & 0 & 0 & 0 & -d_{31} & 0 & 0 \\ 0 & 0 & 0 & s_{66} & 0 & 0 & 0 & 0 & 0 \\ 0 & 0 & 0 & 0 & s_{55} & 0 & 0 & 0 & -d_{15} \\ 0 & 0 & 0 & 0 & 0 & s_{44} & 0 & -d_{24} & 0 \\ d_{33} & d_{32} & d_{31} & 0 & 0 & 0 & \in_{zz} & 0 & 0 \\ 0 & 0 & 0 & 0 & 0 & d_{24} & 0 & \in_{yy} & 0 \\ 0 & 0 & 0 & 0 & d_{15} & 0 & 0 & 0 & \in_{xx} \end{bmatrix} \cdot \begin{bmatrix} \varepsilon_{xx} \\ \varepsilon_{yy} \\ \varepsilon_{zz} \\ \gamma_{yz} \\ \gamma_{xz} \\ \gamma_{xy} \\ E_{xx} \\ E_{yy} \\ E_{zz} \end{bmatrix} \qquad (5.2)
$$

where d represents piezoelectric coupling constant, E is the electric field on the piezomaterial, ε is axial deformation, γ is shear deformation, σ is axial stress, τ is shear stress, $\in$ is the permittivity constant, D is electric displacement and s is the compliance matrix element. Compliance matrix is the inverse of stiffness matrix and stiffness matrix elements can be found from Lamé constants [18] for each particular element. As it can be observed from equations (5.1) and (5.2), stress or electric field applications with correct configuration can result in deflections with different

112

orientations. Piezomaterials can be used in two different ways to implement waving action while satisfying the inextensibility approach up to some degree, namely shear actuation and acoustic actuation.

Although piezo materials can reach high frequencies, i.e. $f > 1$ kHz, [107] there are two important setbacks. One difficulty with piezomaterials is the hysteresis behavior. Hysteresis behavior is the term for going from one state by a particular course and coming back with a different course which eventually leads to a slightly different state than the initial one [12]. Hysteresis behavior similar to Figure 5.1 is also can be explained by hysteretic damping phenomenon which is the energy loss within the material due to friction by any means. Hysteretic friction for polycrystalline materials has a very complex model which depends on temperature, grain size, driving frequency, density, heat conductivity, heat capacity, thermal expansion and wavelength [108]. Hysteretic energy dissipation inside the materials can be calculated with viscous damping analogy [109] which will eventually reduce the overall efficiency of the system. The other problem is the brittle nature of ceramic materials which evidently does not allow high deformations on the crystalline structure [110].
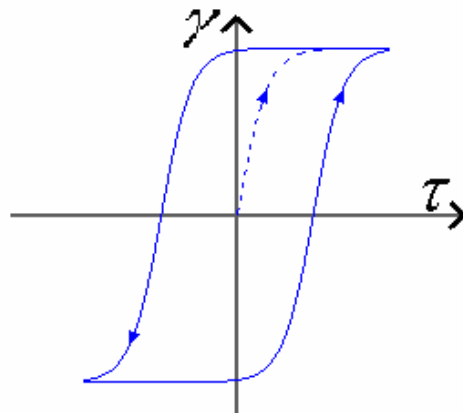
Figure 5.1: Hysteretic behavior for shear stress and shear deformation

5.1.1.1 Shear Actuation

Shear deflection is a promising candidate for wave propagation. Benjeddou *et al.* (1997, 1999), Piefort (2000, 2001), and Hofer and Lerch (2002) made insightful analyses on shear actuation mode. Piezoelectric coupling coefficients are categorized as

"inplane" (i.e. d_{31} and d_{32}), "thickness" (i.e. d_{33}) and "shear" (i.e. d_{15} and d_{24}) modes [114]. Application of external electric fields in appropriate orientations can cause shear mode actuation of piezomaterials which are predicted by (5.1) and (5.2). A single shear actuated piezo material can lead to pure shear deflection as expressed in (5.3) and illustrated in Figure 5.2:

$$\Delta B_o = \Delta L d_{24} E_{yy} \tag{5.3}$$
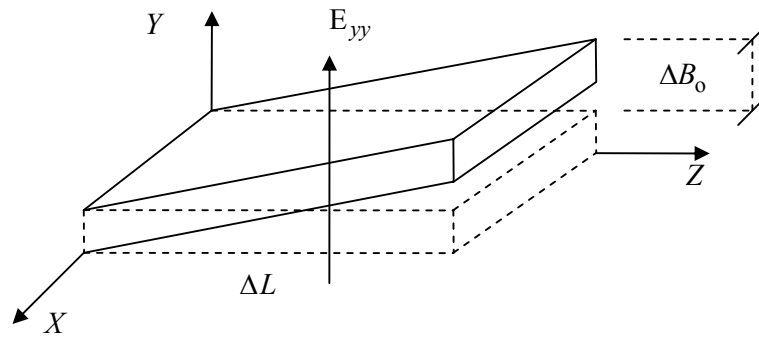
Figure 5.2: Shear actuation

A series of piezoelectric materials, i.e. driven out-of-phase, stacked between other materials with higher deflection capabilities can support traveling waves [115] with larger amplitudes. Hence it would be possible to create the desired wave propagation along a tail-like structure.

5.1.1.2 Acoustic Actuation

Surface acoustic waves (SAW) travel causing elastic wave shaped deformations on the material surface by sliding the molecules in opposite directions [28], [75]. Nguyen and White (1999) proposed a pump mechanism utilizing interdigital transducer structures [28], [116] a kin to the conceptual drawing of Figure 5.3, to create and harvest SAW on piezoelectric films while propagating deformation on film surface causing net fluid velocity in the vicinity via no-slip conditions. Considering the fluid-structure interaction, acoustic pumping method is identical to the proposed traveling

wave micropumps in this text [27], [89], [94], [95] but acoustic actuation employs high frequencies and small amplitudes. In acoustic actuation case, wave speed is expressed in terms of physical properties of the material [108] rather than a choice as discussed in earlier chapters; hence wavelength is inversely proportional to the frequency on the contrary to the shear actuation method where wavelength and amplitude are determined by the number of out-of-phase piezo materials.
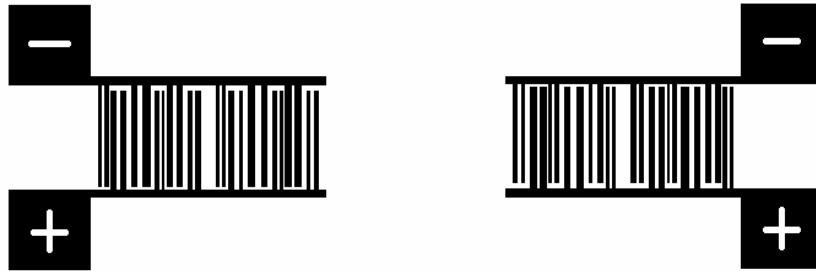
Figure 5.3: A conceptual interdigital transducer design (zoomed view). Proper electrical potential application with driving frequency equal to the natural frequency of interdigital transducer (left hand side) structure causes wave propagation and this wave can be harvested as electric signals by the counter part (right hand side).

5.1.2 Ionic Polymer-Metal Composite (IPMC) Materials

Ionic polymer-metal composites (IPMC) are in use of biomimetic applications such as gripper mechanisms due to their electrical-mechanical-electrical transformation capability [117]. They are capable of high deformations due to their low stiffness but they are not preferred to be operated at high frequencies, i.e. $f \ll 1$ kHz; as driving frequency increase their deformation capability decreases with corresponding power requirement [118], [119]. Their mechanical behavior can also demonstrated by circuitry analogy as a series of resistances, capacitors and diodes based on electrical properties of the actuation [120] which is beyond the scope of this project. The particular IPMC structure discussed briefly here is Nafion. Actuation principle of Nafion is very different than the actuation principle of piezomaterials. The electrical potential causes deformations on inner structure not due to displacement of charged molecules of the structural matrix but by mobilizing foreign ions inside, i.e. moving ions between electrodes coated on the sides stretching the molecules to cause local deformation via counter expansions and contractions as illustrated in Figure 5.4. However surrounding

115

fluid must contain water for ion mobility and as a consequence of liquid transport within, deformation time is limited with back flow incidence inside the structure [121].
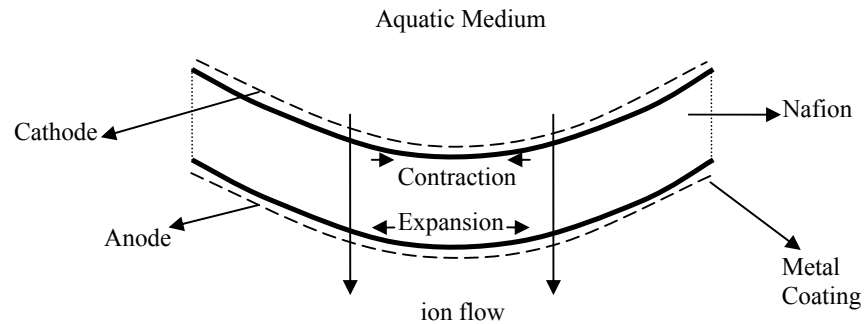
Figure 5.4: Actuation principle of metal coated Nafion.

Traveling waves can be produced by isolated Nafion stacks bonded one another and driven out-of-phase a kin to shear driven piezo stacks [121]. Kim *et al.* (2005) studied an experimental centimeter scale tadpole, i.e. larval amphibian [122], imitating swimming micro robot. Traveling waves generated on 95 mm length Nafion tail driven with 4 Hz ±2.5 V potential; resulting in 1 mm wave amplitude and 23.6 mm/s velocity in water which leads to Re > 1. This experiment violates both low Re number and inextensibility approach expressed in this text but with smaller stack size and smaller amplitude would satisfy these assumptions on microscale.

5.2 Possible Energy Harvesting Methods

A microscale propulsion system is meaningful only if the driving circuitry and energy supply are in microscale and provide the necessary power during operation. It is obvious that an autonomous microrobot should contain its own power supply but conventional batteries are manufactured at least in millimeter sizes [123]. Although energy supply problem is beyond the scope of this text it is imperative that there exist alternative methods to harvest desired power in microscale and thus to realize the micropropulsion system if built.

Different possible energy harvesting methods exist for MEMS applications. Jeon *et al.* (2005) studied a system to transform the acoustic energy to electrical energy by means of transverse piezoelectric sensing [124]. Soliman *et al.* (2005) studied

electromagnetic and electrostatic power generator structures based on electrical-mechanical interactions in microrealm [125]. Nielsen *et al.* (2003) and Bermejo *et al.* (2005) have published a study on "photovoltaic" cell based MEMS power harvesting method to collect the necessary energy from considerable light sources [126], [127]. A micro fuel cell design was discussed for medical MEMS devices by von Stetten *et al.* (2006). There exist other types of electrochemically actuated power systems as discussed by Koeneman *et al.* (1997) and Cardenas-Valencia *et al.* (2003). Another method is harvesting energy directly from human body, (i.e. by means of heat, motion etc.) [131]. There are some other power-supply methods for MEMS applications [129].

Most of the methods presented above require periodic external power or material treatment to operate. Another promising alternative which can answer the power demand in non-stop long term operations is nuclear power. Ni-63 [132] and Tritium [133] are reported to be promising nuclear materials which do not scatter particles in dangerous dozes and could be sealed in microstructures to produce relatively higher amount of power, more than a thousand times of a Li-ion cells, with higher efficiencies, i.e. 40 percent efficiency instead of 5 percent, than conventional batteries for longer duration intervals, such as a few months for some cases [134]. Implementation of nuclear power would increase the possible life time of micro scale autonomous robotic devices.

Since proposed system is supposed to operate in a highly viscous medium with large loss factors, energy supply must be as efficient and durable as possible. Thus nuclear power generation seems to be a viable candidate for possible microswimmer applications.

CHAPTER 6

CONCLUSIONS AND FUTURE WORK

A biologically inspired propulsion method is presented based on numerical data obtained via computational fluid dynamic methods employing deformable mesh formulation to implement moving boundaries. Extensive numerical studies are carried out in order to confirm the asymptotical results to the earlier analytical work discussed so far and the possible actuation methods are partially addressed at the end. Proposed pump systems are in total agreement with those results exposing dynamic pump characteristic. In absence of dominant inertial effects, dynamic behavior originates from the acceleration attribute of the moving boundaries which introduces partial time derivative term into Stokes equations. It is demonstrated that as a stationary boundary in contact with a highly viscous fluid propagates a sinusoidal wave, considerable upstream flow is obtained. As deformations takes place on the boundary, shear force zones appears due to changing velocities. These zones are balanced with counter pressure zones. All these counteracting zone couples shift their positions consequently with the deformations. Simply, there must be flow between high and low pressure zones in the vicinity of the waving membrane. Dragging these zone couples results in dynamically shifting of local flow fields; this time dependent incident eventually leads to a net flow field over the waving boundary. Time permitting; most of the important design variables have been studied in a parametric manner to investigate the general behavior of the proposed pump and swimmer actuation method in the most possible comprehensive manner.

In earlier analytical studies upstream velocity behavior was found to be similar to swimmer velocity behavior which is also validated throughout the swimmer analysis except for the effect of wavelength parameter. It is shown that 3D simulations in particular have extra factors to be considered which could not be covered solely by 2D

assumptions. Detailed analysis on the effect of third dimension revealed that the case of an infinite sheet placed in between two infinite plates can not represent the higher order variations fully. Proposed microswimmer assumed to be neutrally buoyant in the surrounding fluid and was modeled such that only wave propagation is in need of energy supply. All other motions are direct result of the force interaction between swimmer surfaces and surrounding fluid. It is demonstrated that in absence of anchoring force, necessary thrust to move a free body in a highly viscous environment can be obtained by adjusting the design variables of waving action. It is also observed that although instantaneous motion of the swimmers center of mass is a combination of translations and rotations in all three axes, net propulsion takes place on the same axis with wave propagation but in opposite direction. All other motions vanish when averaged over time. Even though steering capabilities of the proposed system are not referred to at any level, it is obvious that combinations of waving tails, i.e. double, triple etc., would grant adequate maneuverability under appropriate control techniques.

Swimmer efficiency is found to be very low due to viscous dissipations as pointed out in previous studies. Especially shear effect inherited from the third dimension results in excessive loss of momentum flux by means of dissipation. Although considerable losses occur, swimmer is supposed to operate in a thermal reservoir, such as human body, which is pre-assumed by isothermal Navier-Stokes equations explained within the introduction. Constant temperature and density assumptions are usually satisfied in real life situations, if not strictly.

In all simulations, waving action on membrane or tail is assumed to be given. In the last chapter some possible ways to create this sinusoidal wave propagation and some power supply methods are discussed in general. This last brief discussion constitutes some of the theoretical background for future work. It is intended to simulate and partially experiment the proposed systems with structural emphasis, with the help of the results presented here in spite of the fact that real life results for fluid studies may differ since there is always an error margin between real life phenomenon and their mathematical representations in numerical procedures.

In the future, the resistive force theory issue addressed at the end of the 3D microswimmer results section will be studied in detail to resolve the wavelength and attack angle issue. Additional structural simulations and experiments will be carried out to demonstrate the feasibility of possible actuation methods for plane-wave-propagation. Large scale experimental pump systems will be manufactured to check the results of

analytical and numerical studies carried out on the subject so far. Hopefully, time permitting; miniaturization of these systems will follow, including the study of proper manufacturing techniques of proposed systems. Construction and power management of the proposed micropump systems are relatively easier since they are supposed to be anchored.

REFERENCES

[1] Feynman, R.P., "There's Plenty of Room at the Bottom", *Journal of Microelectromechanical Systems*, 1(1), pp. 60-66, **1992.**

[2] Feynman, R.P., "Infinitesimal Machinery", *Journal of Microelectromechanical Systems*, 2(1), pp. 4-14, **1993.**

[3] Landau, L.D., Lifshitz, E.M., "Mechanics 3rd Ed.", Course of Theoretical Physics Vol. 1, Elsevier Butterworth-Heinemann, India, **2003.**

[4] Sadler, C., Wilson, J., "Kinematics and Dynamics of Machinery 3rd Ed. In SI Units", Pearson Higher Education, Prentice Hall, **2003.**

[5] Munson, B.R., Donald, F.Y., Okiishi, T.H., "Fundamentals of Fluid Mechanics 4th Ed.", John Wiley & Sons, Inc., USA, **2002.**

[6] Kundu, P., Cohen, I.M., "Fluid Mechanics 3rd Ed.", Elsevier Academic Press, USA, **2004.**

[7] Incropera, F.P., DeWitt, D.P., "Fundamentals of Heat and Mass Transfer", John Wiley & Sons, Inc., USA, **2002.**

[8] White, F.M., "Viscous Fluid Flow 3rd Ed.", McGraw-Hill Series in Mechanical Engineering, McGraw-Hill, N.Y., **2006.**

[9] Purcell, E.M., "Life at Low Reynolds Number", *American Journal of Physics*, 45(1), pp. 3-11, **1976.**

[10] Laser, D.J., Santiago, J.G., "A Review of Micropumps", *J. Micromech. Microeng.,* 4, pp. R35-R64, **2004.**

[11] van Lintel, H.T.G., "Micropump Having a Constant Output", US Patent No. 5.085,562, **1992.**

[12] Damjanovic, D., "Ferroelectric, Dielectric and Piezoelectric Properties of Ferroelectric Thin Films and Ceramics", *Rep. Prog. Phys.*, 61, pp. 1267-1324, **1998.**

[13] Hsu, T.R., "MEMS & Microsystems: Design and Manufacture", McGraw Hill Higher Education, New York, **2002.**

[14] Feng, G.H., Kim, E.S., "Piezoelectrically Actuated Dome-Shaped Diaphragm Micropump", *Journal of Microelectromechanical Systems*, 14(2), pp. 192-199, **2005.**

[15] Carrozza, M.C., Croce, N., Magnani, B., Dario, P., "A Piezoelectric-Driven Stereolithography-Fabricated Micropump", *J. Micromech. Microeng.*, 5, pp. 177 179, **1995.**

[16] Schomburg, W.K., Vollmer, J., Bustgens, B., Fahrenberg, J., Hein, H., Menz, W., "Microfluidic Components in LIGA Technique", *J. Micromech. Microeng.*, 4, pp. 186-191, **1994.**

[17] Benard, W.L., Kahn, H., Heuer, A.H., Huff, M.A., "Thin-Film Shape Memory Alloy Actuated Micropumps", *J. Microelectromech. Syst.*, 7, pp. 245-51, **1998.**

[18] Senturia, S.D., "Microsystem Design", Kluwer Academic Publishers, USA, **2003.**

[19] Rapp, R., Schomburg, W.K., Maas, D., Schulz J., Stark, W., "LIGA Micropump for Gases and Liquids", *Sensors Actuators*, 40(A), pp. 57-61, **1994.**

[20] De Los Santos, H.J., "Introduction to Microelectromechanical Microwave Systems 2nd Ed.", Microelectromechanical Systems Series, Artech House, Inc., USA, **2004.**

[21] Elwenspoek, M., Wiegerink, R., "Mechanical Microsensors, Microtechnology and MEMS", Springer, Germany, **2001.**

[22] Kilani, M.I., Galambos, P.C., Haik, Y.S., Chen, C-J, "Electrostatically Actuated Surface Micromachined Offset Planetary Gear Pump Design", *Proc. ASME Int. Mechanical Engineering Congress and Exposition*, New York, **2001.**

[23] Döpper, J., Clemens, M., Ehrfeld, W., Jung, S., Kämper K-P., Lehr, H., "Micro Gear Pumps for Dosing of Viscous Fluids", *J. Micromech. Microeng.*, 7, pp. 230-232, **1997.**

[24] Sen, M., Wajerski, D., Gad-el-Hak, M., "A Novel Pump for MEMS Applications", *J. Fluids Eng.*, 118, pp. 624-627, **1996.**

[25] Lei, K.F., Li, W.J., "Vortex Micropump for Integrated Optically Transparent Microfluidic Chips", *IEEE International Conference on Mechatronics and Machine Vision in Practice*, Macau, **2004.**

[26] Bourouina, T., Bossebof, A., Grandchamp, J-P., "Design and Simulation of an Electrostatic Micropump for Drug-Delivery Applications", *J. Micromech. Microeng.*, 7, pp. 186-188, **1997.**

[27] Tabak, A.F., Yeşilyurt, S., "Numerical Analysis of the 3D Flow Induced by Propagation of Plane-Wave Deformations on Thin Membranes inside Microchannels", *Proceedings of the Fifth International Conference on Nanochannels, Microchannels and Minichannels*, Puebla, Mexico, **2007.**

[28] Kino, G.S., "Acoustic Waves: Devices, Imaging, and Analog Signal Processing Corrected Edition", Simon & Schuster, New Jersey, **2000.**

[29] Nguyen, N.T., White R.M., "Design and Optimization of an Ultrasonic Flexural Plate Wave Micropump Using Numerical Simulations", *Sensors and Actuators*, 77, pp. 229-236, **1999.**

[30] Kanno, I., Kawano, S., Yakushiji, S., Kotera, H., "Characterization of Piezoelectric Micropump Driven by Traveling Waves", *Seventh International Conference on Miniaturized Chemical and Biochemical Analysis Systems*, California, USA, **2003.**

[31] Shapiro, A.H., Jaffrin, M.Y., Weinberg, S.L., "Peristaltic Pumping with Long Wavelengths at Low Reynolds Number", *J. Fluid Mech.*, 37(4), pp. 799-825, **1969.**

[32] Fuhr, G., Schnelle, T., Wagner, B., "Traveling Wave-Driven Microfabricated Electrohydrodynamic Pumps for Liquid", *J. Micromech. Microeng.*, 4, pp. 217-226, **1994.**

[33] Jeong, S., Seyed-Yagoobi, J., "Electrohydrodynamically Induced Dielectric Liquid Flow Through Pure Conduction in Point/Plane Geometry", *IEEE Trans. Dielectr. Electr. Insul.*, 10, pp. 27-36., **2003.**

[34] Richter, A., Plettner, A., Hofmann, K.A., Sandmaier, H., "A Micromachined Electrohydrodynamic (EHD) Pump", *Sensors and Actuators*, 29(A), pp. 159-168, **1991.**

[35] Probstein, R.F., "Physical Hydrodynamics an Introduction 2nd Ed.", John Wiley & Sons, Inc., New Jersey, **2003.**

[36] Yao, S.H., Santiago, J.G., "Porous Glass Electroosmotic Pumps: Theory", *J. Colloid Interface Sci.*, 268, pp. 133-142, **2003.**

[37] Cheng, D.K., "Field and Wave Electromagnetics 2nd Ed.", Addison-Wesley Series in Electrical Engineering, USA, **1992.**

[38] Lemoff, A.V., Lee, A.P., Miles, R.R., McConaghy, C.F., "An AC Magnetohydrodynamic Micropump: Toward a True Integrated Microfluidic System", *10th International Conference on Solid-State Sensors and Actuators*, Sendai, Japan, **1999.**

[39] Cao, L., Mantell, S., Polla, D., "Implantable Medical Drug Delivery Systems Using Microelectromechanical Systems Technology", *First Annual International IEEE EMBS Special Topic Conference on Microtechnologies in Medicine & Biology*, Lyon, France, **2000.**

[40] Polla, D.L., Erdman, A.G., Robbins, W.P., Markus, D.T., Diaz-Diaz, J., Rizq, R., Nam, Y., Bricker, H.T., Wang, A., Krulevitch, P., "Microdevices in Medicine", *Annu. Rev. Biomed. Eng.*, 2, pp. 551-76, **2000.**

[41] Meyns, B., Sergeant, P., Nishida, T., Perek, B., Zietkiewicz, M., Flameng, W., "Micropumps to Support the Heart during CABG", *European Journal of Cardiothoracic Surgery*, 17, pp. 169-174, **2000.**

[42] Mack, M.J., "Beating Heart Surgery: Does It Make a Difference?", *The American Heart Hospital Journal*, 1(2), pp. 149-157, **2003.**

[43] Hammel, D., Mollhoff, T,. Soepawata, R., van Aken, H., Scheld, H.H., "Mechanical Myocardial Support Systems 1997: An Overview of Intra-Aortic Balloon Counterpulsation to Implantable Left Ventricular Support Systems", *Anaesthesist*, 46(5), pp. 408-418, **1997.**

[44] Gardeniers, J.G.E., van den Berg, A., "Lab-on-a-chip Systems for Biomedical and Environmental Monitoring", *Anal. Bioanal. Chem.*, 378, pp. 1700-1703, **2004.**

[45] Garcia, M., Krimoama, S., Marlborough, D., Leafasia, J., Rieckmann, K.H., "Immunochromatographic Test for Malaria Diagnosis (letter)", *Lancet*, 347, pp.1549, **1996.**

[46] Zhang, T., "Valveless Piezoelectric Micropump for Fuel Delivery in Direct Methanol Fuel Cell (DMFC) Devices", PhD Thesis Submitted to Graduate Faculty of the School of Engineering, University of Pittsburgh, **2005.**

[47] Tuckerman, D. B., Pease, R.F.W., "High-Performance Heat Sinking for VLSI", *IEEE Electron. Device Lett.*, 2, pp. 16-129, **1981.**

[48] Micci, M.M., Ketsdever, A.D., Ed., "Micropropulsion for Small Space Craft", *AIAA American Institute of Aeronautics & Ast.*, USA, **2000.**

[49] http://www.imdb.com/title/tt0099810/, **1990.**

[50] Brennen, C., Winnet, H., "Fluid Mechanics of Propulsion by Cilia and Flagella", *Ann. Rev. Fluid Mech.*, 9, pp. 339-398, **1977.**

[51] Campbell, N.A., Reece, J.B., Simon, E.J., "Essential Biology 2nd International Ed.", Benjamin Cummings, USA, **2006.**

[52] DePamphilis, M.L., Adler, J., "Fine Structure and Isolation of the Hook-Basal Body Complex of Flagella from *Escherichia Coli* and *Bacillus Subtilis*", *J. Bacteriol.*, 105, pp. 384-395, **1971.**

[53] Norton, R.L., "Machine Design: An Integrated Approach 2nd Ed.", Pearson Prentice-Hall Engineering/Science/Mathematics, USA, **2000.**

[54] Larsen, S.H., Adler, J., Gargus, J.J., Hogg, R.W., "Chemomechanical Coupling without ATP: The Source of Energy for Motility and Chemotaxis in Bacteria", *Proc. Natl. Acad. Sci. USA*, 71, pp. 1239-1243, **1974.**

[55] Jahn, T.L., Landman, M.D., "Locomotion of Spirochetes", *Trans. Am. Microsc. Soc.*, 84, pp. 395-406, **1965.**

[56] Edwin, Jr., E.P., Public Health Image Library, PHIL #836, http://phil.cdc.gov/phil/home.asp, **1986.**

[57] Votta, J.J., Jahn, T.L., Griffith, D.L., Fonseca, J.R., "Nature of the Flagellar Beat in *Trachelomonas volvocina, Rhabdomonas Spiralis, Menoidium cultellus and Chilomonas paramecium*", *Trans. Am. Microsc. Soc.,* 90, pp. 404-412, **1971.**

[58] Higdon, J.J.L., "The hydrodynamics of Flagellar Propulsion: Helical Waves", *J. Fluid Mech.*, 94(2), pp. 331-351, **1978.**

[59] Brokaw, C.J., Gibbons, I.R., "Mechanism of Movement in Flagella and Cilia", *Swimming and Flying in Nature*, 2, pp. 89-132, **1975.**

[60] Jahn, T.L., Votta, J.J., "Locomotion of Protozoa", *Ann. Rev. Fluid Mech.*, 4, pp. 93-116, **1972.**

[61] Jahn, T.L., Landman, M.D., Fonseca, J.R., "The mechanism of Locomotion in Flagellates. II. Function of the Mastigonemes of Ochromonas", *J. Protozool.*, 11, pp. 221-296, **1964.**

[62] Gibbons, B.H., Gibbons, I.R., "Flagellar Movement and Adenosine Triphosphate Activity in Sea Urchin Sperm Extracted with Triton X-100", *J. Cell Biol.*, 54, pp. 75-97, **1972.**

[63] Sfakiotakis, M., Lane, D.M., Davies, J.B.C., "Review of Fish Swimming Modes for Aquatic Locomotion", *IEEE Journal of Oceanic Engineering*, 24(2), pp. 237-252, **1999.**

[64] Taylor, Sir, G.I., "Analysis of the Swimming of Microscopic Organisms", *Proc. R. Soc. Lond.*, 209(A), pp. 447-461, **1951.**

[65] Avron, J.E., Gat, O., Kenneth, O., "Optimal Swimming at Low Reynolds Numbers", *American Physical Society Physical Review Letters*, 93(18), 186001, **2004.**

[66] Childress, S., "Mechanics of Swimming and Flying", Cannings, C., ed., Hoppensteadt, F., ed., Cambridge Studies in Mathematical Biology:2, Cambridge University Press, New York, **1981.**

[67] Batchelor, G.K., "An Introduction to Fluid Dynamics", Cambridge Mathematical Library, Cambridge University Press, USA, **2005.**

[68] Landau, L.D., Lifshitz, E.M., "Fluid Mechanics 2nd Ed.", Course of Theoretical Physics Vol. 6, Elsevier Butterworth-Heinemann, Oxford, **2005.**

[69] Gray, J. and Hancock, G., "The Propulsion of Sea-Urchin Spermatozoa", *Journal of Experimental Biology*, 32, pp. 802-814, **1955.**

[70] Katz, D.F., "On the Propulsion of Micro-Organisms near Solid Boundaries", *J. Fluid Mech.*, 64, pp. 33-49, **1974.**

[71] Lighthill, Sir, J., "Mathematical Biofluiddynamics", *Society for Industrial and Applied Mathematics*, USA, **1975.**

[72] Stone, H.A., Samuel, A.D.T., "Propulsion of Microorganisms by Surface Distortions", *Physical Review Letters*, 77, pp. 4102-4104, **1996.**

[73] Wiggins, C.H., Goldstein, R.E., "Flexive and Propulsive Dynamics of Elastica at Low Reynolds Number", *Physical Review Letters*, 80(17), pp. 3879-3882, **1998.**

[74] Wiggins, C.H., Riveline, D., Ott, A., Goldstein, R.E., "Trapping and Wiggling: Elastohydrodynamics of Driven Microfilaments", *Biophysical Journal*, 74, pp. 1043-1060, **1998.**

[75] Cleland, A.N., "Foundations of Nanomechanics From Solid-State Theory to Device Applications", Advanced Texts in Physics, Springer, Germany, **2003.**

[76] Cox, R.G., "The Motion of Long Slender Bodies in a Viscous Fluid Part 1. General Theory", *J. Fluid Mech.*, 44, pp. 791-810, **1969.**

[77] Lagomarsino, M.C., Capuani, F., Lowe, C.P., "A Simulation Study of the Dynamics of a Driven Filament in an Aristotelian Fluid", *Journal of Theoretical Biology*, 224, pp. 215-224, **2003.**

[78] Dreyfus, R., Baudry, J., Roper, M.L., Fermigier, M., Stone, H.,A., Bibette, J., "Microscopic Artificial Swimmers", *Nature*, 437(6), pp. 862-864, **2005.**

[79] Behkam, B., Sitti, M., "Design Methodology for Biomimetic Propulsion of Miniature Swimming Robots", *Journal of Dynamic Systems*, Measurement, and Control, 128, pp. 36-43, **2006.**

[80] Edd, J., Payen, S., Rubinsky, B., Stoller, M.L., Sitti, M., "Biomimetc Propulsion for a Swimming Surgical Micro-Robot", *Proc. of the Int. Conf. on Intelligent Robots and Systems*, Las Vegas, USA, **2003.**

[81] Bathe, K.J., "Finite Element Procedures", Prentice Hall, New Jersey, **1996.**

[82] Boyce, W.E., DiPrima, R.C., "Elementary Differential Equations 7th Ed.", John Wiley & Sons, Inc., USA, **2001.**

[83] Udaykumar, H.S., Tran, L., Belk, D.M., Vanden, K.J., "An Eulerian Method for Computation of Multimaterial Impact with ENO Shock-Capturing and Sharp Interfaces" *Journal of Computational Physics*, 186(1), pp. 136-177, **2003.**

[84] Antaki, J.F., Blelloch, G.E., Ghattas, O., Malčević, I., Miller, G.L., Walkington, N.J., "A Parallel Dynamic-Mesh Lagrangian Method for Simulation of Flow with Dynamic Interfaces", *Proceedings of the IEEE/ACM SC2000 Conference*, **2000.**

[85] COMSOL, A.B., COMSOL Multiphysics User Guide, **2005.**

[86] Williams, Jr., J.H., "Fundamentals of Applied Dynamics", John Wiley & Sons, Inc., Canada, **1996.**

[87] Donea, J., Huearta, A., Ponthot, J.-P., Ferran, A.R., "Arbitrary Lagrangian-Eulerian Methods", Encyclopedia of Computational Mechanics Vol. 1: Fundamentals, Stein, E., de Borst, R., Hughes, T.J.R., Ed., John Wiley & Sons, Ltd., **2004.**

[88] Duarte, F., Gormaz, R., Natesan, S., "Arbitrary Lagrangian-Eulerian Method for Navier-Stokes Equations with Moving Boundaries", *Comput. Methods Appl. Mech. Engrg.*, 193, pp. 4819-4836, **2004.**

[89] Tabak, A.F., Yeşilyurt, S., "Simulation-Based Analysis of Flow Due to Traveling Plane-Wave Deformations on Elastic Thin-Film Actuators in Micropumps", *Microfluidics and Nanofluidics*, accepted, **2007.**

[90] Winslow, A., "Numerical Solution of the Quisilinear Poisson Equations in a Nonuniform Triangle Mesh", *J. Comp. Phys.*, 2, pp. 149-172, **1967.**

[91] Knupp, P.M., "Winslow Smoothing on Two-Dimensional Unstructured Meshes", *Engineering with Computers*, 15, pp. 263-268, **1999.**

[92] http://www.comsol.com/, **2007.**

[93] http://www.mathworks.com/, **2006.**

[94] Tabak, A.F., Yeşilyurt, S., "Numerical Simulations of a Traveling Plane-Wave Actuator for Microfluidic Applications", Hiller, J.A., Ed., *Proceedings of the COMSOL Users Conference*, Boston, **2006.**

[95] Tabak, A.F., Yeşilyurt, S., "Numerical Simulations and Analysis of a Micropump Actuated by Traveling Plane Waves", *SPIE-Photonics West, MOEMS-MEMS*, San Jose, **2007.**

[96] Tabak, A.F., Yeşilyurt, S., "Numerical Analysis of a Planar Wave Propagation Based Micro Propulsion System", *ASME International Mechanical Engineering Congress and Exposition*, Seattle, Washington, extended abstract submitted, **2007.**

[97] Davis, T.A., "Algorithm 832: UMFPACK V4.3 – An Unsymmetric-Pattern Multifrontal Method", *ACM Transactions on Mathematical Software*, 90(2), pp. 196-199, **2004.**

[98] Schenk, O., Gärtner, K., "Solving Unsymmetric Sparse Systems of Linear Equations with PARDISO", *Future Generation Computer Systems*, 20(3), pp. 475-487, **2004.**

[99] http://www.intel.com/cd/software/products/asmo-na/eng/perflib/219780.htm, **2007.**

[100] Techet, A.H., Hover, F.S., Triantafyllou, M.S., "Seperation and Turbulence Control in Biomimetic Flows", *Flow, Turbulence and Combustion*, 71, pp. 105-118, **2003.**

[101] Schilling, R.J., Harris, S.L., "Applied Numerical Methods for Engineers Using MATLAB® and C", Books/Cole Thomson Learning, USA, **2000.**

[102] The MathWorks, Inc., MATLAB® Function Reference, **2006.**

[103] Becker, L.E., Koehler, S.A., Stone, H.A., "On Self-Propulsion of Micro-Machines at Low Reynolds Number: Purcell's Three Link Swimmer", *J. Fluid Mech.*, 490, pp. 15-35, **2003.**

[104] http://en.wikipedia.org/wiki/Piezo, **2007.**

[105] Gururaja, T.R., Schulze, W.A., Cross E.L., Newnham, R.E., Auld, A.B., Wang, Y.J., "Piezoelctric Composite Materials for Ultrasonic Transducer Applications. Part I: Resonant Modes of Vibration of PZT Rod – Polymer Composites", *IEEE Transduction on Sonics and Ultrasonics*, SU-32(4), pp. 481-498, **1985.**

[106] Harrison, J.S., Ounaies, Z., "Piezoelectric Polymers", ICASE NASA Langley Research Center, ICASE Report No: 2001-43, **2001.**

[107] Li, H.,Q, Roberts, D.,C., Steyn, J.L., Turner, K.T., Carreteo, J.A., Yaglioglu, O., Su, Y.-H., Saggere, L., Hagood, N.W., Spearing, S.M., Schmidt, M.A., "A High Frequency High Flow Rate Piezoelectrically Driven MEMS Micropump", *Proceedings IEEE Solid State Sensors and Actuators Workshop*, Hilton Head, **2000.**

[108] Landau, L.D., Lifshitz, E.M., "Theory of Elasticity 3rd Ed.", Course of Theoretical Physics Vol. 7, Elsevier Butterworth-Heinemann, China, **2005.**

[109] Rao, S.S., "Mechanical Vibrations 4th Ed.", Pearson Prentice Hall, USA, **2004.**

[110] Shackelford, J.F., "Introduction to Materials Science for Engineers 5th Ed.", Prentice Hall, N.J., **2000.**

[111] Benjeddou, A., Trindade, M.A., Ohayon, R., "A Unified Beam Finite Element Model for Extension and Shear Piezoelectric Actuation Mechanisms", *J. Intell. Mater. Syst. Struct.*, 8(12), pp. 1012-1025, **1997.**

[112] Benjeddou, A., Trindade, M.A., Ohayon, R., "New Shear Actuated Smart Structure Beam Finite Element", *AIAA Journal*, 37(3), pp. 378-383, **1999.**

[113] Piefort, V., Henrioulle, K., "Modelling of Smart Structures with Colocated Piezoelectric Actuator/sensor Pairs: Influence of the In-plane Components", *Identification, Control and Optimization of Engineering Structures*, Civil-Comp Press, Edinburgh UK, **2000.**

[114] Piefort, V., "Finite Element Modelling of Piezoelectric Active Structures", PhD Thesis submitted to Faculty of Applied Sciences, PhD Thesis, Université Libre De Bruxelles, **2001.**

[115] Hofer, M., Lerch, R., "Finite Element Calculation of Wave Propagation and Excitation in Periodic Piezoelectric Systems", Mang, H.A., Rammerstorfer, F.G., Eds., *Fifth World Congress on Computational Mechanics*, Vienna, Austria, **2002.**

[116] Mamishev, A.V., Sundara-Rajan, K., Yang, F., Du, Y., Zahn, M., "Interdigital Sensors and Transducers", *Proceedings of IEEE*, 92(5), pp. 808-845, **2004.**

[117] Shahinpoor, M., Bar-Cohen, Y., Xue, T., Simpson, J.O., Smith, J., "Ionic Polymer-Metal Composites (IPMC) as Biomimetic Sensors and Actuators", *Proceedings of Fifth Annual International Symposium on Smart Structures and Materials*, San Diego, **1998.**

[118] Bonomo, C., Fortuna, L., Giannone, P., Graziani, S., Strazzeri, S., "A Model for Ionic Polymer Metal Composites as Sensors", *Smart Mater. Struct.*, 15, pp. 749-758, **2006.**

[119] Kim, B., Kim, D.-H., Jung, J., Park, J.-O., "A Biomimetic Undulatory Tadpole Robot Using Ionic Polymer-Metal Composite Actuators", *Smart Mater. Struct.*, 14, pp. 1579-1585, **2005.**

[120] Bonomo, C., Fortuna, L., Giannone, P., Graziani, S., Strazzeri, S., "A Nonlinear Model for Ionic Polymer Metal Composites as Actuators", *Smart Mater. Struct.*, 16, pp. 1-12, **2007.**

[121] Arena, P., Bonomo, C., Fortuna, L., Frasca, M., Graziani, S., "Design and Control of an IPMC Wormlike Robot", *IEEE Transactions on Systems, Man, and Cybernetics Part B: Cybernetics*, 36(5), pp. 1044-1052, **2006.**

[122] http://en.wikipedia.org/wiki/Tadpole, **2007.**

[123] SII Micro Parts Ltd., Micro Batteries Product Catalogue, http://www.siimp.co.jp/, **2007.**

[124] Jeon, Y.B., Sood, R., Jeong, J.-H., Kim, S.-G., "MEMS Power Generator with Transverse Mode Thin Film PZT", *Sens. and Actuators, A Phys.*, 122(1), pp. 16-22, **2005.**

[125] Soliman, M.S.M., El-Saaday, E.F., Mansour, R.R., "Electromagnetic and Electrostatic Micro-Power Generators; an Overview", *Proceedings of the IEEE International Conference on Mechatronics & Automation*, Niagara Falls, Canada, **2005.**

[126] Nielsen, O.M., Arana, L.R., Baertsch, C.D., Jensen, K.F., Schmidt, M.A., "A Thermophotovoltaic Micro-Generator for Portable Power Applications", *The 12th International Conference on Solid State Sensors, Actuators and Microsystems*, Boston, **2003.**

[127] Bermejo, S., Ortega, P., Jimenez, J.J., Castañer, "Response of c-Si PV Arrays under Monochromatic Light for MEMS Power Supply", *J. Micromech. Microeng.*, 15, pp. 1446-1453, **2005.**

[128] von Stetten, F., Kerzenmacher, S., Lorenz, A., Chokkalingam, V., Miyakawa, N., Zengerle, R., Ducrée, "A One-Compartment, Direct Glucose Fuel Cell for Powering Long-Term Medical Implants", *IEEE MEMS 2006*, Istanbul, Turkey, **2006.**

[129] Koeneman, P.B., Busch-Vishniac, I.J., Wood, K.L., "Feasibility of Micro Power Supplies for MEMS", *Journal of Microelectromechanical Systems*, 6(4), pp. 355-362, **1997.**

[130] Cardenas-Valencia, A., Fries, D., Broadbent, H., Langebrake, L., Benson, R., "Micro-Actuated Aluminum Galvanic and Semi-Fuel Cells for Powering Remote Lab-On-A-Chip Applications", *7th International Conference on Miniaturized Chemical and Biochemical Analysis Systems*, Squaw Valley, California, **2003.**

[131] Sato, N., Ishii, H., Urano, M., Sakata, T., Terada, J., Morimura, H., Shigematsu S., Kudou K., Kamei, T., Machida, K., "Novel MEMS Power Generator with Integrated Thermoelectric and Vibrational Devices", *The 13th International Conference on Solid-State Sensors, Actuators and Microsystems*, Seoul, Korea, **2005.**

[132] Wilson, H.W., "Radioactivity of Ni^{59} and Ni^{63}", *Phys. Rev.*, 79(6), pp. 1032-1033, **1950.**

[133] Andreev, V.M., Kavetsky, A.G., Kalinovsky, V.S., Khvostikov, V.P., Larionov, V.R., Rumyantsev, V.D., Shvarts, M.Z., Yakimova, E.V., Ustinov, V.A., "Tritium Powered Betacells Based on $AI_x Ga_{1-x} As$," *Photovoltaic Specialists Conference, Conference Record of the Twenty-Eighth IEEE*, pp. 1253-1256, **2000.**

[134] Lal, A., Blanchard, J., "The Daintiest Dynamos", *IEEE Spectrum*, September, pp. 36-41, **2004.**